Detection of Magnetic Nanoparticles for Bio-sensing Applications

A DISSERTATION
SUBMITTED TO THE FACULTY OF THE GRADUATE SCHOOL
OF THE UNIVERSITY OF MINNESOTA
BY

LIANG TU

IN PARTIAL FULFILLMENT OF THE REQUIREMENTS
FOR THE DEGREE OF
DOCTOR OF PHILOSOPHY

JIAN-PING WANG, ADVISOR

JUNE, 2013

Acknowledgements

I am very much delighted to have this chance to thank those people who supported and helped me. First of all, I would like to thank my advisor, Professor Jian-Ping Wang, for his sharing of scientific mind, introducing me to the research field of magnetic materials and supervising me to do this exciting project. The discussion with him was invaluable and guided me to passionately explore amazing science in this topic.

I would also like to acknowledge the input and advice from Professor Randall Victora, Beth Stadler and Jack Judy during my work and stay in the center for Micromagnetic and Information Technollogies (MINT), which builds a solid foundation for me in the field of magnetism and magnetic materials.

I am thankful to my dissertation committee members Professor Sang-Hyun Oh, Jizhen Lin, Anand Gobinath, Beth Stadler, Rhonda Franklin, and Walter Low for their time, help and effort of serving in my committee.

This work was also supported by an OTC Innovation grant from the University of Minnesota and National Science Foundation BME 0730825 and Institute of Engineering in Medicine at University of Minnesota. Parts of this work were carried out using the Characterization Facility which receives partial support from NSF through the NSF Minnesota MRSEC Program under Award Number DMR-0819885 and NNIN program.

It has been an enjoyable experience with the past and current members of Professor Wang's group. I would like to thank all the group members for their valuable discussion and friendly feedback.

Finally, I would like to express my love and thanks to my parents and my friends. Without their love, support and advice, I would have never gone so far.

Dedication

With gratitude to my parents.

Abstract

Superparamagnetic Nanoparticles (MNPs) are used as probes to detect biomarkers (protein, DNA, etc.) by using a search coil based scheme for volume detection and by using a Giant Magneto-Resistance (GMR) sensor for surface detection.

In search coil detection scheme, a low frequency field is applied to saturate the MNPs and a high frequency field is applied to modulate the nonlinearity of the magnetization into the high frequency region where the noise floor is lower. Under an ac magnetic field, MNPs above certain hydrodynamic size (for Iron Oxide is around 20nm) will experience physical rotation called Brownian relaxation. [1]By studying the phase information of the mixing frequencies, the Brownian relaxation time can be monitored in real time thus dynamic bio-molecular interaction can be recovered. The Néel and Brownian relaxation of MNPs with different magnetic and hydrodynamic properties has been investigated by using a different DC bias field and AC field frequency. The specific response from each MNP can be used as magnetic identification in nano-scale application.

A Giant Magneto-Resistance (GMR) sensor array is also used for MNPs detection. Compared with the search coil, GMR sensor is more sensitive but requires surface modification for bio- molecular detection. A low-noise Printed Circuit Board is designed and assembled to implement Wheatstone bridge, multiplexing function, and signal amplification. An AC field is applied to the entire sensor array while an AC current is flowing through a specific sensor. The sensor response will generate mixing frequency terms as the multiplication of field frequency and current frequency. All the active sensors printed with specific capture antibodies are scanned sequentially, recorded in real time, and compared with the reference sensor which is covered by a thick protection layer. Signal to noise ratio for the integrated system is studied by considering the noise contribution from all components.

Table of Contents

List of Figures

List of Tables

Chapter 1 Introduction

1.1 Ferromagnetism in a material

Spin and orbital movement of charged particles (electrons, protons) creates magnetic field. In this study, all the magnetism comes from motion of electrons. Magnetic field is generated by passing electron current through solenoid conducting coil (Ampère's law), and magnetic material's net moment is from the spin-orbital coupling of the unpaired 3d electrons.

When a magnetic field H is applied, according to classical physics, there is an increase of mechanical orbital moment L. With a negative gyromagnetic ratio γ, the changed magnetic moment $\mu m = L^* \gamma$ will have an opposite direction to the applied field. This negatively magnetized phenomenon is called diamagnetism. Diamagnetism is present in all materials; however it is too weak to be considered in most experiments and often ignored especially when other strong magnetism is exhibited. A special property of diamagnetism is its temperature independence. Some examples of diamagnetic material are copper and water.

On the other hand, the magnetic field also tends to align the local magnetic dipole to the field's direction. This phenomenon is called paramagnetism. Quantum physics limits the orientation of spins to up and down relative to the applied field. The distribution of the number of up and down spins is regulated by Boltzmann factors. The total net magnetic moment can be calculated by summarizing the up and down spins, and turns out to have a negative dependence on the temperature. The calculated susceptibility is $\chi = \mu m/H = C/T$. C is the Curie constant. Material (such as sodium) with isolated, distinguishable magnetic ions also shows paramagnetic. This is called Pauli paramagnetism, and is not dependent on temperature.

Another very important magnetism is the ferromagnetism. In ferromagnetic material, the spins have positive coupling through Heisenberg interaction, which

means under Curie temperature T_c spontaneous magnetization will happen. The saturation magnetization M_s also has a negative dependence on the temperature due to the uncorrelated thermal spin fluctuations. Above T_c, thermal disorder reigns over the spin-spin coupling, the material shows the paramagnetic property: $\chi = \mu m/H = C/(T - T_c)$. This positively coupling mainly exists in 3d electron (transition metal such as Fe, Co, and Ni) and 4f electron (rare earth material such as Gd and Dy).

Some oxides have the magnetism of superexchange. In these oxides, a 3d electron of transition metal atom is shared with a 2p orbit of oxygen. Each oxygen atom has two 2p covalent bonding, and the doubly occupied orbital has two electrons of opposite spin. Thus the two metal atoms have different spins through the oxide bonding. The superexchange interaction separate some of the transition metal atoms from others in term of spin directions, and the two group of atoms with same spin direction are called site A and site B. If the total magnetic moments of site A and site B are equal, the material is Antiferromagnetic, and no net moment is exhibited without applied field; if the two sites have different moment, the material is Ferrimagnetic. One common superexchange group is iron oxide, including Antiferromagnetic hematite (α-Fe_2O_3) and FeO, and Ferromagnetic maghemite (γ-Fe_2O_3) and Fe_3O_4 (magnetite). Susceptibility (χ) of Antiferromagnetic material is similar to that of Ferromagnet, while Ferrimagnetic $1/\chi$ has a nonlinear dependence on temperature[1].

1.2 Superparamagnetism

Magnetic domains exist in bulk ferromagnetic materials to minimize magnetostatic energy. For very small Magnetic Nano Particles (MNP) compared to magnetic domain wall in term of size, it costs more energy to create a domain wall than to support the magnetostatic energy of the single-domain state. When the size of this single-domain MNP is small enough, even the thermal fluctuation energy

(K_BT) can overcome the anisotropy energy (K_UV), and the magnetization can flip between the two easy axes very fast compared to the measurement time. In this case, the anisotropy energy can be ignored and zero coercivity is observed. This phenomenon is like paramagnetic material with giant magnetic moment, thus called superparamagnetism.

At temperature T, the mean time between two spin flips of a MNP is called the Néel relaxation time:$\tau_N = \tau_0 e^{(\frac{K_U V}{k_B T})}$,where τ_0(attempting time) is a length of time depending on the characteristic of the material. During one measurement time τ_m, the magnetization spin will flip several times if $\tau_m \gg \tau_N$, thus the overall measured magnetization will average to zero. A net magnetization will be measured only if $\tau_m \ll \tau_N$. The state of the nanoparticle (superparamagnetic or blocked) depends on the measurement time τ_m and Néel relaxation time τ_N. When the measurement time τ_m is fixed, temperature can affect Néel relaxation time τ_N, and thus affect the observation of superparamagnetic state or blocked state.The transition ($\tau_m = \tau_N$) between these two states can be determined by the blocking temperature $T_B = \frac{K_U V}{k_B \ln(\frac{\tau m}{\tau_0})}$.When temperature and measurement time are fixed, MNP is considered as superparamagnetic when $\frac{K_U V}{k_B T} < 25$. [2] Compared with paramagnetism, superparamagnetism has much higher magnetization. Compared with ferromagnetism, superparamagnetism has no remanence, thus superparamagneticMNPs can disperse very well by Van der Waals force in a carrier fluid and the solution is called ferrofluid.

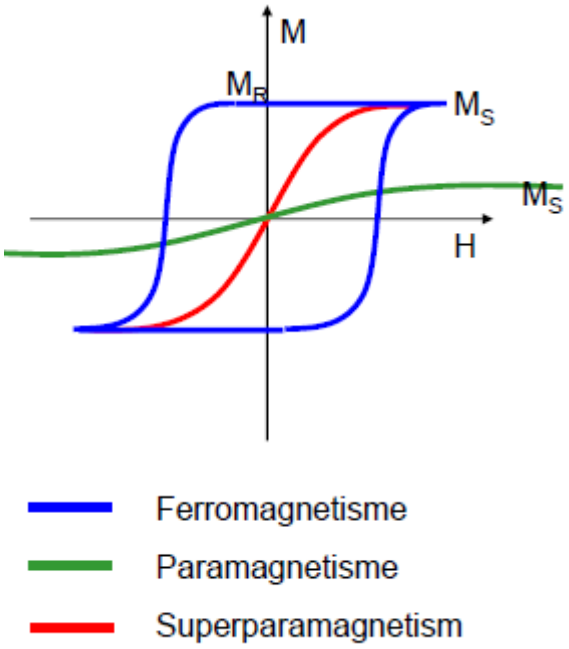

Figure 1-1 Comparison of magnetization curves of Ferro, Para and Superpara-magnetism

SuperparamagneticMNPs have been used for biomedicine such as Magnetic Resonance Imaging (MRI), cell-, DNA-, protein- separation, RNA fishing, drug delivery, hyperthermia, and biomarker detection.3 MNPs are usually ferri or ferromagnetic. Superparamagnetic iron oxide nanoparticles (SPIO),maghemite (γFe_2O_3) and magnetite (Fe_3O_4) are widely useddue to their relatively easy synthesis process and establishedbiocompatibility[4]. However the low saturation magnetization of SPIO limits their applications. Bulk Fe-Co alloy has the highest saturation magnetization 240 emu/g at Fe:Co composition ratio of around 60:40, while iron also has a high saturation magnetization of 220 emu/g. Prof. Wang's group from University of Minnesota first proposed the application of bio-compatible FeCo-Au(Ag). At 20 Oe external field, the moment of an isotropic $Fe_{0.6}Co_{0.4}$nanoparticle is $2.4*10^{-15}$emu, which is 17 times larger thanthat of a Fe_3O_4 nanoparticle and 28 times than that of a γFe_2O_3nanoparticle. Oxidation usually takes place for unprotected Fe-Co nanoparticles. Natural oxidation layer (approximately

1.5nm thick), Au, or SiOx shell through a diffusion control based gas condensation method can function as a protection layer, at the expense of magnetic moment.

The critical size for superparamagnetic particles depends on the anisotropy and magnetic moment of the material shown in Figure 1-2**Error! Reference source not found.**. As the size of MNPs increases, multi-domains will be formed to decrease the magnetostatic energy. When the domain wall is at the center of the MNP, the magnetostatic energy is minimal. When the domain wall is pushed to the side (maximal magnetization) by an external field, the Zeeman energy is minimal. However, after the field is removed, the thermal agitation is not strong enough to create multi-domains by overcoming the exchange energy barrier. Thus net magnetic moment, also called remanence, is present even without external field. This net magnetic moment will cause MNPs to form clusters and cannot well disperse in the solution.

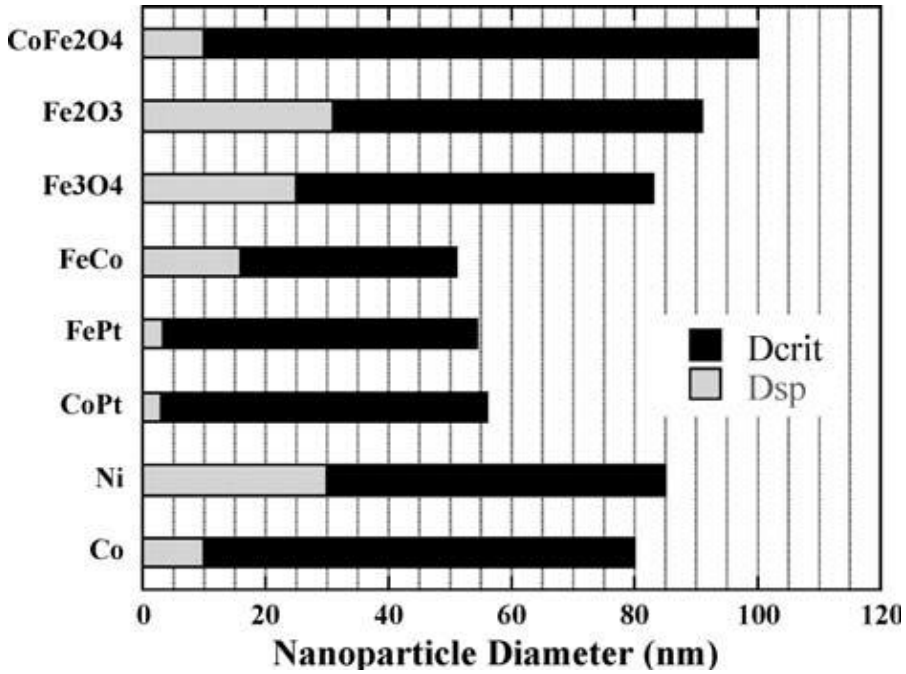

Figure 1-2 Single domain size, Dcrit and magnetic stability size or the superparamagnetic limit at room temperature, Dsp for some common ferromagnetic materials.[5]

1.3 Magnetic Spin Relaxation

1.3.1 Electron spin dynamics

The dynamics of electron spin include precession and damping, and can be described by Landau-Lifshitz (LL) equation:

$$\dot{M} = -\gamma' M \times H_{eff} + \lambda M \times (M \times H_{eff}) \ ,$$

where$\gamma' = \frac{\gamma}{1+\gamma^2\eta^2 M_s^2}$ and$\lambda = \frac{\gamma^2\eta}{1+\gamma^2\eta^2 M_s^2}$.

Gilbert later replaced the damping term in the Landau-Lifshitz equation by one that depends on the time dependence of the magnetic field[6]:

$$\dot{M} = \gamma M \times (H_{eff} - \eta\dot{M}) \ ,$$

whereγ is gyromagnetic ratio and η is damping constant.

1.3.2 Static magnetization

For superparamagnetic MNPs, in the presence of a DC magnetic field H in z direction, the magnetic moment of each MNP will follow the Boltzmann distribution, and the parallel magnetization is:

$$\langle M_z \rangle = M_s \cdot \langle \cos\vartheta \rangle = M_s \cdot \langle x \rangle = M_s \cdot \frac{\int_{-1}^{1} x e^{\xi x} dx}{\int_{-1}^{1} e^{\xi x} dx}$$

$$= M_s \cdot \left(\frac{e^{\xi} + e^{-\xi}}{e^{\xi} - e^{-\xi}} - \frac{1}{\xi} \right) = M_s \cdot (\coth\xi - \frac{1}{\xi}) = M_s \cdot L(\xi),$$

whereL is Langevin function and $\xi = vHM_s/k_BT$.

1.3.3 Dynamic magnetization

By the thermal agitation, the MNP will experience Brownian motion and magnetic spin disorientation. To include the thermal energy, two treatments will be

introduced here[7].

Langevin's treatment of Brownian motion is listed below:

$$m\ddot{x}(t) + \zeta\dot{x}(t) = \lambda(t)$$

Where $\zeta\dot{x} = 6\pi\eta a\dot{x}$ is the friction term, η is the viscosity of the surrounding fluid, and 'a' is the radius of a spherical particle. (t) describes the thermal white noise, where $\langle\lambda(t_1)\lambda(t_2)\rangle = 2D\delta(t_1 - t_2)$. D is the diffusion coefficient $D = k_B T\zeta$.

Fokker-Plank treatment considers the magnetization dynamics in term of drift and diffusion:

$$\frac{\partial W}{\partial t} = -\nabla \cdot \boldsymbol{J} = -\nabla \cdot (W\dot{\boldsymbol{r}} - k'\nabla W)$$

Where W is the probability density of orientations of **M**. **J** is the current density. $\boldsymbol{r} = \boldsymbol{M}/M_s$ is the magnetization vector. K' is a constant which determines the extent of thermal disruption, and its value can be calculated by comparing the solution of Fokker-Plank equation in DC field to the static magnetization.

$$k' = \frac{k_B T}{v}\frac{\gamma}{M_s}\frac{\alpha}{1+\alpha^2} = \frac{1}{2\tau_N}$$

Where $\alpha = -\lambda/M_s = \eta\gamma M_s$, and τ_N is the Néel relaxation time.

1.3.4 Brown's equation

Suppose the magnetization **M** only has orientation dependence W(ϕ, ϑ), where ϕ is the azimuthal angle and ϑ is the polar angle. The Fokker-Plank equation can be written as Brown's equation:

$$\frac{1}{k'}\frac{\partial W}{\partial t} = \frac{1}{\sin\vartheta}\frac{\partial}{\partial\vartheta}\left\{\sin\vartheta\left[\frac{v}{k_B T}\left(\frac{\partial V}{\partial\vartheta} - \frac{1}{\sin\vartheta}\frac{1}{\alpha}\frac{\partial V}{\partial\phi}\right)W + \frac{\partial W}{\partial\vartheta}\right]\right\}$$

$$+\frac{1}{sin\vartheta}\frac{\partial}{\partial\phi}\left\{\frac{v}{k_BT}\left(\frac{1}{\alpha}\frac{\partial V}{\partial\vartheta}+\frac{1}{sin\vartheta}\frac{\partial V}{\partial\phi}\right)W+\frac{1}{sin\vartheta}\frac{\partial W}{\partial\phi}\right\}$$

To solve the Brown's equation, W is expanded into Legendre harmonics in spherical coordinates:

$$W(\vartheta,\phi,t)=\sum_{n=0}^{\infty}\sum_{m=-n}^{n}a_{nm}(t)P_n^{|m|}(cos\vartheta)e^{i\omega\phi}$$

$$|m|\leq n,\quad a_{n,-m}=a_{nm}^{*}$$

$P_n^{|m|}(cos\vartheta)$are the associated Legendre function.

$a_{nm}(t)$are the time-dependent functions describing the time evolution of each spherical harmonic.

$P_1(cos\vartheta)$describes the evolution of the alignment with the z axis.

$P_1^1(cos\vartheta)cos\phi$describes alignment perpendicular to the z axis.

W Legendre expansion is usually limited to certain number of harmonics in order to solve the Brown's equation more conveniently.

1.3.5 Solution to Brown's equation

To simply the problem, suppose the magnetization has no azimuthal ϕ dependence relative to applied field, and energy V only includes Zeeman energy where anisotropy energy is ignored:

$$W(\vartheta,t)=\sum_{n=0}^{\infty}a_n(t)P_n(cos\vartheta)$$

$$V(\vartheta)=-HM_s cos\vartheta$$

Brown's equation reduces to:

$$\frac{1}{k'}sin\vartheta\frac{\partial W}{\partial t}=\frac{\partial}{\partial\vartheta}[sin\vartheta(\frac{v}{k_BT}\frac{\partial V}{\partial\vartheta}W+\frac{\partial W}{\partial\vartheta})]$$

Replace W with the Legendre expansion, the Legendre coefficients a_n forms a

first order equation:

$$\frac{1}{k'n(n+1)}\dot{a}_n + a_n = \xi\left[\frac{a_{n-1}}{2n-1} - \frac{a_{n+1}}{2n+3}\right]$$

Or in matrix form:

$$2\tau_N \dot{\boldsymbol{a}}_m = \boldsymbol{\lambda}_m \boldsymbol{a}_m$$

The Laplace transforms of the above equation is an iterative equation:

$$\frac{2\tau_N s}{n(n+1)}A_n(s) + A_n(s) = \frac{2\tau_N}{n(n+1)}a_n(0) + \xi\left[\frac{A_{n-1}(s)}{2n-1} - \frac{A_{n+1}(s)}{2n+3}\right]$$

A_n can be solved numerically or analytically by truncating the higher order harmonics.

1.3.6 Néel relaxation time

For small $\xi = vHM_s/k_BT$, it is possible to limit the size of matrix$\boldsymbol{\lambda}_m$ to 2*2.

m = 0:

$$2\tau_N \dot{a}_{10} = -2a_{10} + 2\xi a_{00} - \frac{2}{5}\xi a_{20}$$

$$2\tau_N \dot{a}_{11} = -2a_{11} - \frac{3}{5}\xi a_{21}$$

m=1:

$$2\tau_N \dot{a}_{20} = -6a_{20} + 2\xi a_{10} - \frac{6}{7}\xi a_{30}$$

$$2\tau_N \dot{a}_{21} = -6a_{21} + \xi a_{11} - \frac{8}{7}\xi a_{31}$$

The above differential equations can be represented by linear nonhomogeneous equations with Laplace operator s.

$$\begin{pmatrix} 2\tau_N s + 2 & \frac{2}{5}\xi \\ -2\xi & 2\tau_N s + 6 \end{pmatrix}\begin{pmatrix} a_{10} \\ a_{20} \end{pmatrix} = \begin{pmatrix} 2\xi a_{00} \\ -\frac{6}{7}\xi a_{30} \end{pmatrix}$$

Equating the determinant to zero, we can get the parallel Néel relaxation time:

$$\tau_{||}(\xi) \approx \tau_N/(1-\xi^2/10)$$

$$\begin{pmatrix} 2\tau_N s+2 & \frac{3}{5}\xi \\ -\xi & 2\tau_N s+6 \end{pmatrix}\begin{pmatrix} a_{11} \\ a_{21} \end{pmatrix} = \begin{pmatrix} 0 \\ -\frac{8}{7}\xi a_{31} \end{pmatrix}$$

Equating the determinant to zero, we can get the perpendicular Néel relaxation time:

$$\tau_{\perp}(\xi) \approx \tau_N/(1-3\xi^2/40)$$

If the uniaxial anisotropy energy $V_a = Ksin^2\vartheta$ is considered, the relaxation time will have dependence on $\sigma = Kv/k_BT$.

For small σ, $\tau(\sigma) = \tau_N\left(1+\frac{2}{5}\sigma\right) + O(\sigma^2)$

For large σ>1.5, the orientation of magnetization can be treated discrete in the Wentzel-Kramers-Brillouin-Jeffreys (WKBJ) model, and the relaxation time is:

$$\tau_{||}(\sigma) \approx \frac{\tau_N}{2}\sqrt{\pi}\sigma^{-3/2}e^{\sigma}$$

1.4 AC susceptibility of MNPs

1.4.1 Brownian relaxation

In an AC magnetic field, not only can the magnetic spin follow the field direction, but also the MNPs can physically rotate by magnetic torque to align to the applied field. To describe how fast this physical alignment takes, the Brownian relaxation time τ_B is introduced:

$$\tau_B = \frac{3\eta V_H}{k_BT} = \frac{\eta\pi D_H^3}{2k_BT}$$

where η is the viscosity of the carrier or matrix fluid, and V_H is the effective

hydrodynamic volume of MNP, and D_H is the effective hydrodynamic diameter.

1.4.2 Total relaxation

Since Néel relaxation and Brownian relaxation occurs simultaneously, the total relaxation is a combination of these two schemes.

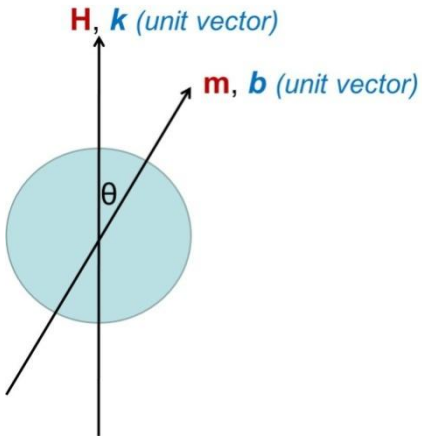

Figure 1-3 schematic of the magnetic moment of a MNP in relative to the applied field.

Néel relaxation shows that magnetic moment will flip on the two directions of the easy axis randomly under thermal fluctuation: m(t')=m × r(t') × b, where m is the magnetic moment of a MNP, and r is a stochastic function that has Poison distribution (±1), and b is the unit magnetization vector. Auto-correlation of r(t') is shown by Kenrick in 1929 as[8]:

$$\overline{r(t')r(t'+t)} = \exp(-|t|/\tau_N)$$

Brownian relaxation shows the whole MNP rotate along θ in the viscose surrounding fluid. Debye in 1929 has shown that auto correlation of cos(θ) is a function of τ_B:

$$\overline{\cos\theta(t')\cos\theta(t'+t)} = \exp(-|t|/\tau_B)/3$$

So the measured magnetization along the field direction:

$$m_z(t') = m \cdot r(t') \cdot \cos\theta(t')$$

Then the auto correlation of measured magnetization is:

$$c(t) = \overline{m_z(t') \cdot m_z(t'+t)}$$

$$= m^2 \overline{r(t')r(t'+t)\cos\theta(t')\cos\theta(t'+t)}$$

$$= \left(\frac{m^2}{3}\right)\exp\left\{-|t|\left[\frac{\tau_N + \tau_B}{\tau_N \tau_B}\right]\right\} = \left(\frac{m^2}{3}\right)\exp\{-|t|/\tau\}$$

From the above expression, the total relaxation time is the geometric mean of Néel and Brownian relaxation time:

$$\tau = \frac{\tau_N \tau_B}{\tau_N + \tau_B}$$

The total relaxation time τ will depend more on the smaller value of τ_N and τ_B. So Néel and Brownian relaxation, which ever will occur faster will dominate the total relaxation process.

1.4.3 Debye model

Under an AC field H(t) = H_0*exp(jωt), at any time instantt_0, the field will magnetize the MNPs, and the magnetization effects will then decay exponentially with the time constant τ. In other words, magnetization M(t) is not only from the current applied

field, but also from the previous remanence. So the magnetization can be calculated by convolving applied field with the decay function.

$$M(t) = \chi_0 \int_{-\infty}^{t} H_0 e^{i\omega x} c(x-t)\, dx = -\chi_0 H_0 e^{i\omega t} \int_0^{\infty} \phi(x) e^{-i\omega x}\, dx$$

Where χ_0 is the static susceptibility, $\chi_0 = Nm^2/3kTV\mu_0$, and $\phi(x) = c(x)/c(0)$ is the normalized autocorrelation of the magnetization defined in the previous sector.

Then the AC susceptibility can be expressed in time domain:

$$\chi(t) = -\chi_0 \int_0^{\infty} \phi(x) e^{-i\omega x}\, dx$$

The complex susceptibility can be converted in frequency domain using Fourier Transform, and this is the Debye model used to describe various relaxation phenomenon including the dielectric dispersion.

$$\chi(\omega) = \frac{\chi_0}{1 + j\omega\tau} = \frac{\chi_0}{\sqrt{1+(\omega\tau)^2}} + j\frac{-\chi_0\omega\tau}{\sqrt{1+(\omega\tau)^2}}$$

$$= \frac{\chi_0}{\sqrt{1+(\omega\tau)^2}} \cdot e^{-j\tan^{-1}(\omega\tau)} = |\chi| \cdot e^{j\varphi}$$

As shown above, the AC complex susceptibility can be expressed as the real part $\frac{\chi_0}{\sqrt{1+(\omega\tau)^2}}$ and the imaginary part $\frac{-\chi_0\omega\tau}{\sqrt{1+(\omega\tau)^2}}$, or as the amplitude $\frac{\chi_0}{\sqrt{1+(\omega\tau)^2}}$ and phase $\varphi = -\tan^{-1}(\omega\tau)$.

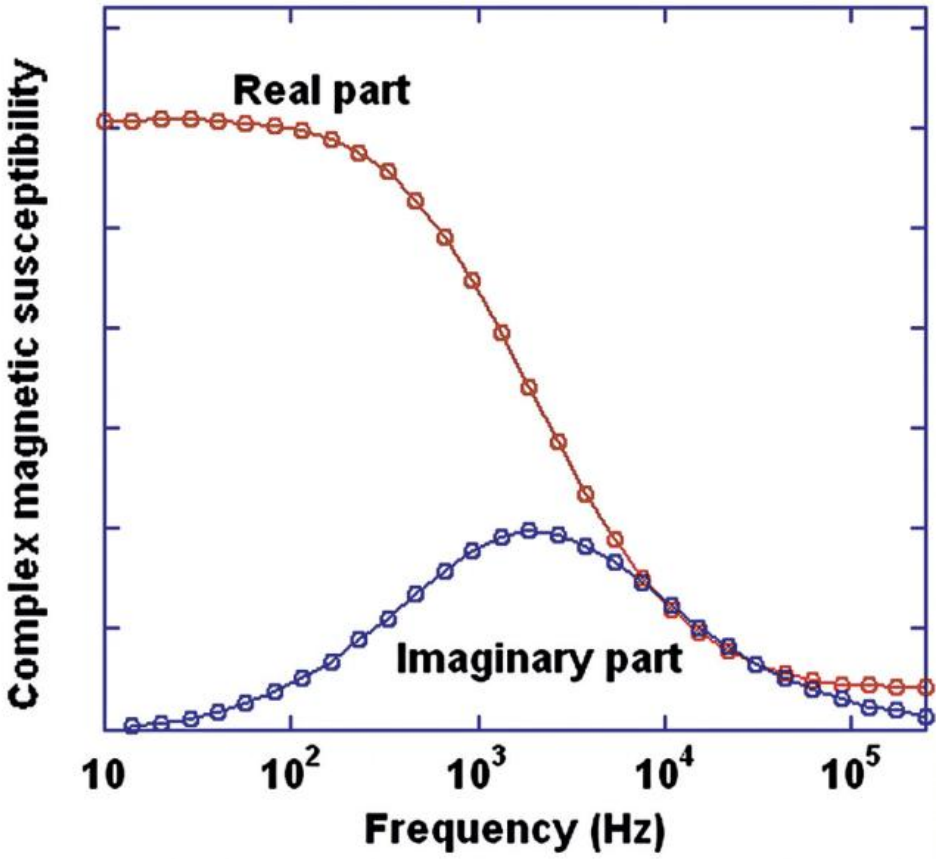

Figure 1-4 An example of measurement of real and imaginary part of ac susceptibility along frequency.

1.5 MNPs characterization

1.5.1 VSM

A Vibrating Sample Magnetometer (VSM) is an instrument that measures the static magnetization of a sample under a range of magnetic field[9].

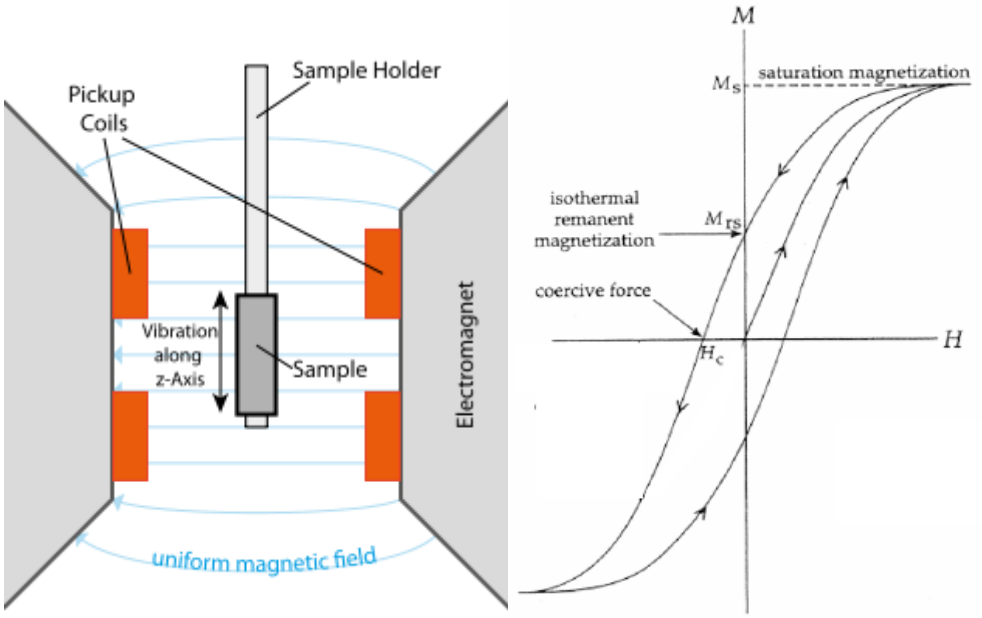

Figure 1-5 schematic of a VSM and an example of measured hysteresis curve.

A static magnetic field is applied by a Helmholtz coil with soft magnetic core, and the magnetized sample is vibrated through a vibrating rod. The vibrating frequency is usually in MHz range and the magnetization of the vibrating sample is picked up by a pair of pickup coils. The induced voltage in the pickup coil is proportional to the sample's magnetic moment, and can be measured by a lock-in amplifier using the vibration-generating signal as its reference signal. By measuring the magnetization while sweeping the magnetic field, the hysteresis curve of a material can be obtained.

1.5.2 SEM and TEM

A scanning electron microscope (SEM) is a type of electron microscope that produces images of a sample by scanning it with a focused beam of electrons[10]. This instrument has been used to study the surface structure such as the GMR sensor. An electron beam is formed and focused on a small spot on the sample surface, producing various signals (the most commonly used is secondary electrons) that can be detected and that contain information about the sample' surface topography and

composition. The electron beam is scanned to generate a whole surface image. SEM can achieve resolution better than 1 nanometer.

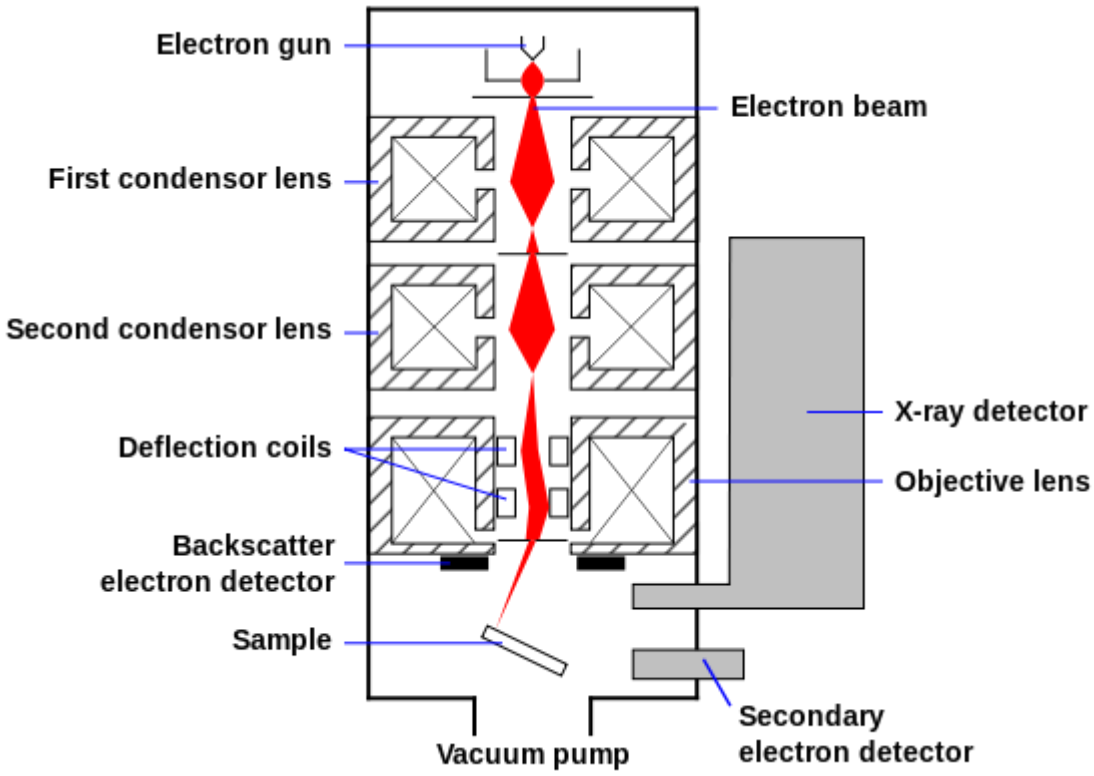

Figure 1-6 schematic of a TEM.

A transmission electron microscopy (TEM) is a microscopy technique whereby a bean of electron is transmitted through an ultra-thin specimen, interacting with the specimen as it passes through[11]. An image is formed from the interaction of the electrons transmitted through the specimen. Most recent technology pushes the detection resolution to below 0.5 Å. TEM has been used to measure the size and the crystal structure of MNPs.

1.5.3 DLS

Dynamic light scattering (DLS) is a technique that can be used to determine the size distribution profile of small particles in solution[12]. When light hits small particles, the light scatters as long as particles are small compared to the wavelength. Since particles are undergoing Brownian motion in solutions, the scattering intensity will fluctuate. Brownian motion speed is related to the particles' hydrodynamic size, so is the scattering intensity fluctuation. So by observing the time autocorrelation of the scattering intensity, particles' overall hydrodynamic size distribution can be calculated. Compared to TEM, DLS can measure the particles' organic surface layer while TEM cannot due to the poor contrast. DLS can estimate the overall particle size distribution by fitting to the Log-normal function. However, for more complex distribution like poly-dispersed, Nanosight instrument can track individual particles' movement and thus can estimate in small scales.

[1]Robert C. O'Handley, Modern Magnetic Materials: Principles and Applications.
Publication Date: Nov. 26, 1999| ISBN-10: 0471155667| ISBN-13:978-0471155669| Edition: 1

[2] Superparamagnetism, (Oct. 22nd, 2012), from *http://en.wikipedia.org/wiki/Superparamagnetism*

[3] Superparamagnetism, (Oct. 22nd, 2012), from *http://lmis1.epfl.ch/webdav/site/lmis1/shared/Files/Lectures/Nanotechnology%20for%20engineers/Archives/2004_05/Superparamagnetism.pdf*

[4]Y. Jing, S. He, T. Kline, Y. Xu and J.P. Wang, 'High-Magnetic-Moment Nanoparticles for Biomedicine', 31st Annual International Conference of the IEEE EMBS, Minneapolis, Minnesota, USA, September 2-6, 2009.

[5] K. M. Krishnan, A. B. Pakhomov, Y. Bao, et al.,'Nanomagnetism and spin electronics: materials, microstructure and novel properties.' J Mater Sci 41 (2006) 793-815.

[6] Landau-Lifshitz-Gilbert equation, (Oct. 23rd, 2012), from *http://en.wikipedia.org/wiki/Landau%E2%80%93Lifshitz%E2%80%93Gilbert_equation*

[7]W. T. Coffey, P. J. Gregg, and Y. P. Kalmykov, 'On the Theory of Debye and Néel Relaxation of Single Domain Ferromagnetic Particles', in Advances in Chemical Physics, edited by I. Prigogine and S. A. Rice (Wiley, New York, 1993), Vol. 83, p. 263

[8] B K P Scaife, 'On the low-field, low-frequency susceptibility of magnetic fluids', J. Phys. D: Appl. Phys. **19** (1986) L195-L197

[9] Vibrating sample magnetometer, (Oct. 31st, 2012), from *http://en.wikipedia.org/wiki/Vibrating_Sample_Magnetometer*

[10] Scanning electron microscope, (Oct. 31st, 2012), from *http://en.wikipedia.org/wiki/Scanning_electron_microscope*

[11] Transmission electron microscope, (Oct. 31st, 2012), from *http://en.wikipedia.org/wiki/Transmission_electron_microscopy*

[12] Dynamic light scattering, (Oct. 31st, 2012), from *http://en.wikipedia.org/wiki/Dynamic_light_scattering*

Chapter 2 Mixing Frequency Method

2.1 Search-coil Detection

Magnetic nanoparticle detection for biological and medicinal applications has been achieved by a variety of sensing schemes. The search-coil based sensing scheme is one of good candidates among them for future point-of-care devices and systems because of its unique integrated features: relatively high sensitivity at room temperature[13], dynamic volume detection (non-surface binding), intrinsic superiority to measure ac magnetic field, functionality as an antenna for wireless information transmission, application driven properties such as low cost, portability and easy to use.

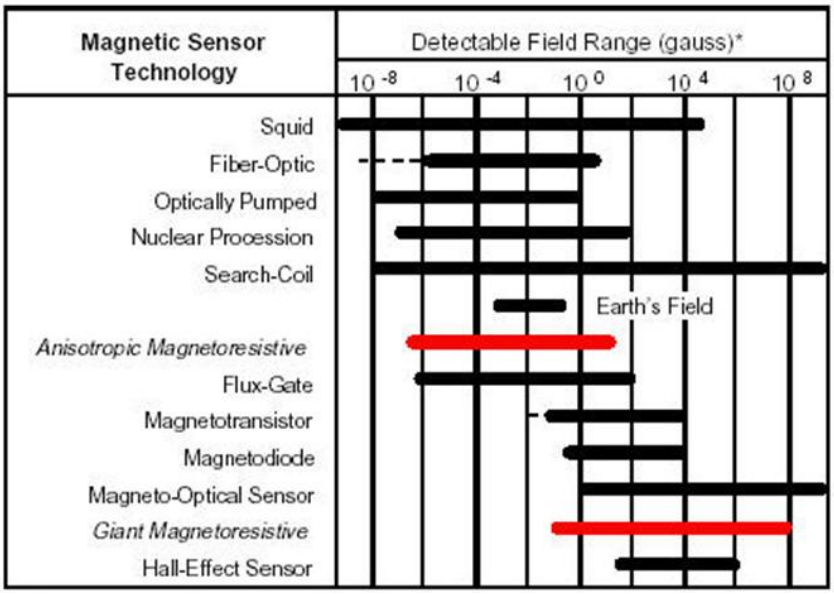

Figure 2-1 detection ranges of various magnetic field sensors[14]

Figure 2-1 summarizes the detection ranges of various magnetic field sensors. Squid is the most sensitive sensor of static magnetic field. Search coil has a wide

detection range, and a very high detection limit. For bio-immunoassay, the popular research topics nowadays are Search-coil, Flux-gate, Giant Magneto-Resistive(GMR) sensor, and Hall-effect sensor. GMR sensor usually requires the MNPs to be concentrated on the sensor surface, while search-coil can achieve volume detection. Figure 2-2 shows each sensor's sensitivity along frequency. The majority of the sensors have slightly higher sensitivity at higher frequency due to the nature of 1/f noise. However, the sensitivity of search coil depends strongly on the frequency, because the Faraday's law of induction shows that the voltage signal on the pick-up coil is proportional to the field frequency. So above 1kHz, search-coil can out-perform most of the other sensors.

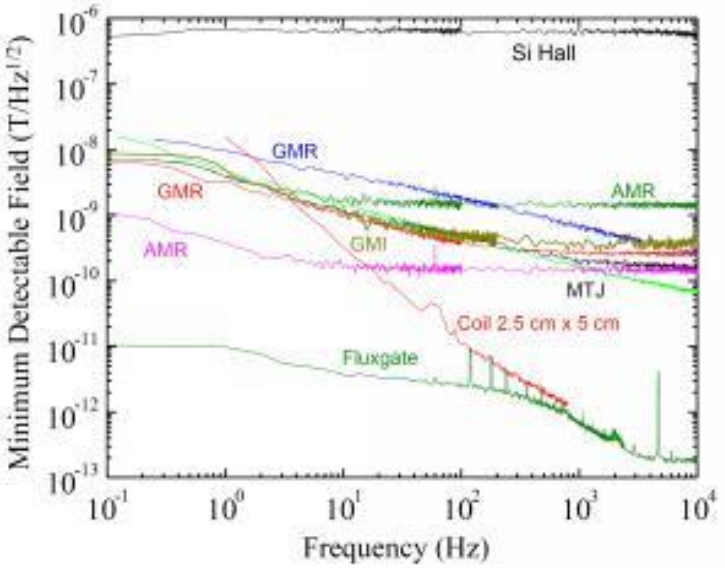

Figure 2-2 sensitivity of various magnetic field sensors along frequency.[15]

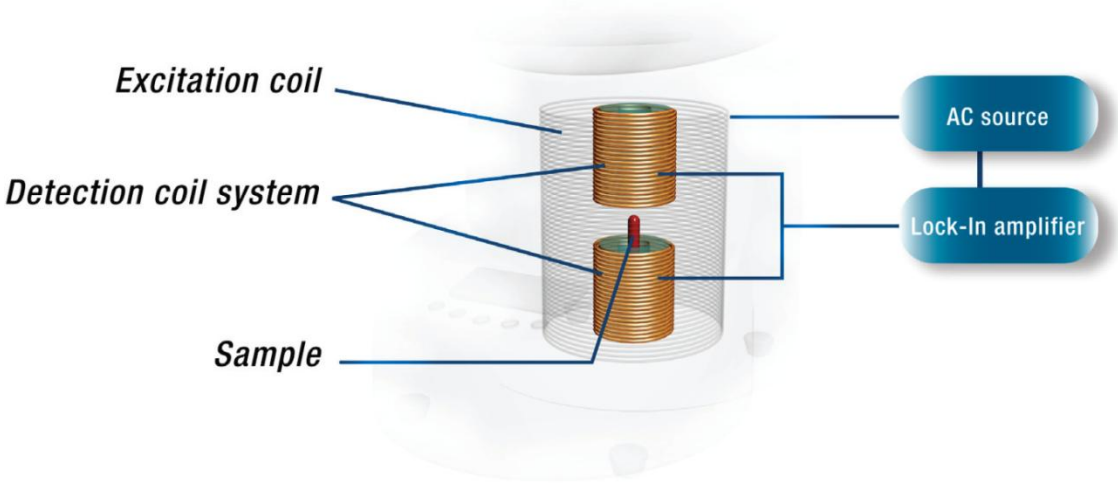

Figure 2-3 Schematic of traditional susceptometer setup.

In traditional ac magnetic susceptibility measurement such as Physical Property Measurement System (PPMS)[16], DynoMagSusceptometer[17] (shown in Figure 2-3) and Slit Toroid Device[18], a pair of balanced coils picks up the magnetization of the sample under an ac magnetic field and a lock-in amplifier or impedance analyzer is used to detect the complex ac susceptibility. However, this method suffers from high background fluctuation due to the thermal and mechanical instability of the coils, as well as the magnetic moment contribution from sample matrix (e.g. water) and/or container (e.g. plastic tube). Given the small amount of MNPs sample in the paramagnetic or diamagnetic environment, the background is a significant portion of the overall signal.

2.2 MNPs magnetic flux in coil (equation and simulation)

The magnetization of a MNP can be treated as dipole model when its external dipole fields are of interests. A single MNP can generate a net magnetic flux in the detection coil.

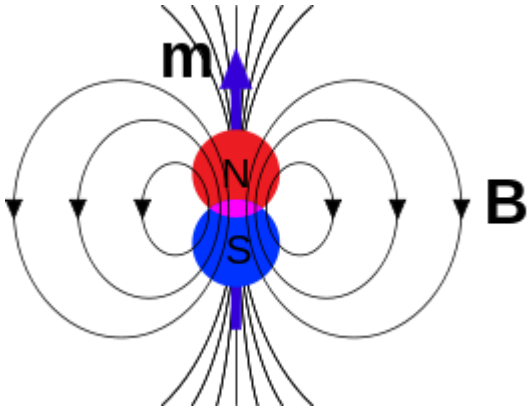

Figure 2-4 Magnetic dipole model[19]

In order to calculate the magnetic flux density **B**, magnetic potential **A** is introduced.

$$\boldsymbol{A}(\boldsymbol{r}) = \frac{\mu_0}{4\pi} \cdot \frac{\boldsymbol{m} \times \boldsymbol{r}}{r^3}$$

$$\boldsymbol{B}(\boldsymbol{r}) = \boldsymbol{\nabla} \times \boldsymbol{A} = \frac{\mu_0}{4\pi} \cdot \left(\frac{\boldsymbol{3r}(\boldsymbol{m} \cdot \boldsymbol{r})}{r^5} - \frac{\boldsymbol{m}}{r^3}\right)$$

If only the observation vector **r** is perpendicular to the magnetization **m**, magnetic field **B** can be simplified to:

$$\boldsymbol{B}(\boldsymbol{r}) = \frac{\mu_0}{4\pi} \cdot \frac{-\boldsymbol{m}}{r^3}$$

The saturation magnetization for magnetite is Ms = 121.89 emu/cc. And the saturation magnetic moment m_s=Ms * Vol. The magnetic moment of a MNP at applied field H is:

$$m(H) = m_s \cdot L(\xi) = m_s \cdot L\left(\frac{vHM_s}{k_B T}\right)$$

Where Boltzmann constant is $k_B = 1.38 * 10^{-23}$ J/K = $1.38 * 10^{-16}$ erg/K

Sample	m_0 (emu= erg/G) per particle	m (emu) per particle (at ±30 Oe)	Concentration	Core size by Langevin fitting
SHS-10, 10nm	$1.0x10^{-16}$	$1.9\text{-}2.0x10^{-18}$	1mg/mL(Fe) 0.86nmol/mL	7.7 nm
SHS-20, 20nm	$5.7x10^{-16}$	$1.03\text{-}1.13x10^{-16}$	1mg/mL(Fe) 0.11nmol/mL	13.8 nm
SHS-30, 30nm	$4.0x10^{-16}$	$1.00\text{-}1.10x10^{-16}$	1mg/mL(Fe) 0.031nmol/mL	12.3 nm
MACS, 50nm, (12 20nm MNPs)	$80.0\text{-}82.0x10^{-16}$	$22.52\text{-}24.7x10^{-16}$	3.14pmol/mL	18.2 nm
Adembeads, 100nm	$365\text{-}370x10^{-16}$	$17.01\text{-}19.03x10^{-16}$	1.6pmol/mL	

Table 2-1List of properties of 5 types of MNP

For all the iron oxide nanoparticles from Ocean NanoTechnology, their technical specifications are listed below[20],

IO size (nm):	5	10	15	20	25	30	40	50
Size tolerance (nm):	2.5	2.5	2.5	2.5	2.5	2.5	5	5
Size distribution:	<10%	<5%	<5%	<5%	<5%	<5%	<10%	<10%
Molar concentration (uM) of 5 mg/mL (Fe):	34.5	4.3	1.25	0.55	0.27	0.16	0.066	0.034
Structure:	Maghemite		Magnetite					
Chemical Formula:	Fe_2O_3		Fe_3O_4					

Table 2-2 List of properties of iron oxide MNPs from Ocean Nanotech.

From the TEM image, the MNPs have sphere shape for the size below (including) 30nm. Above 30nm, the shape MNPs is cubic or irregular.

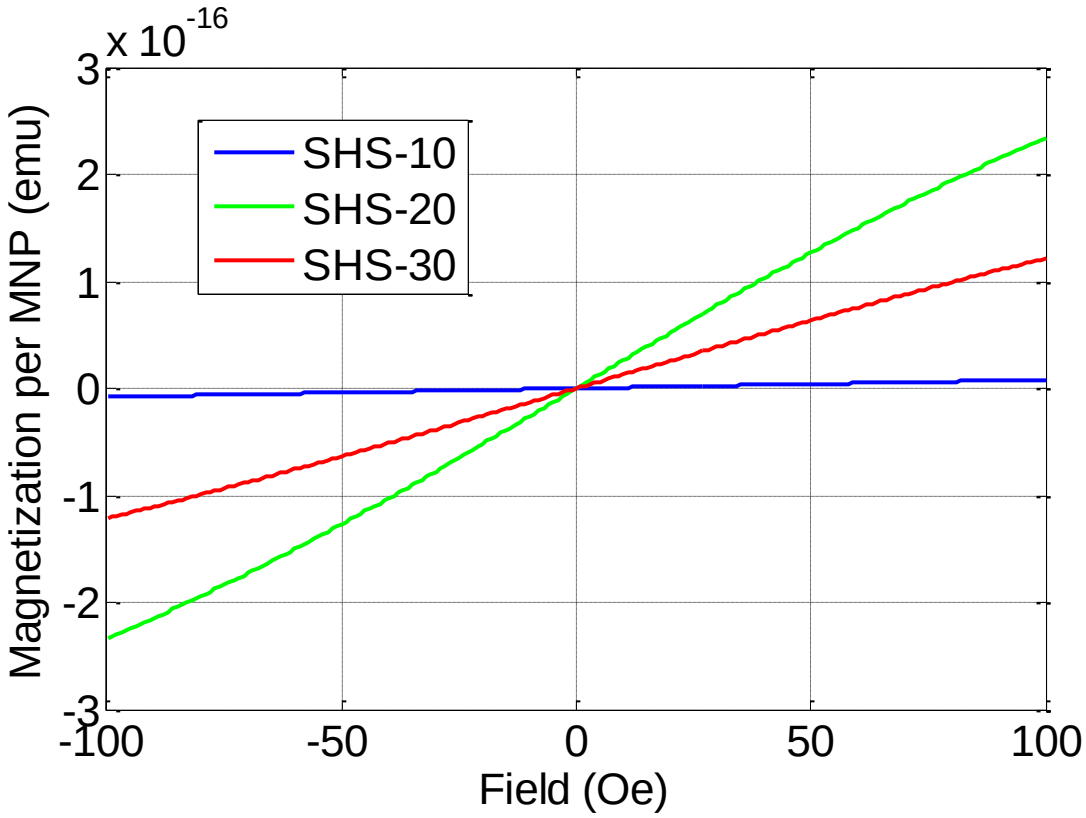

Figure 2-5 Magnetic moment of a single MNP

At 100 Oe, the magnetic moment of a single 30nm MNP is about m= 1.2e-16 emu = 1.2e-19 Am^2.

Suppose the detection coil has a radius of R=0.01m, the total magnetic flux generated by a single MNP can be calculated as:

$$\emptyset_0 = \int \boldsymbol{B} \cdot d\boldsymbol{s} = \frac{\mu_0 m}{4\pi} \int_0^{2\pi} \int_R^{\infty} \frac{1}{r^3} r \, dr d\theta = \frac{4\pi \times 10^{-7} * 1.2 \times 10^{-19}}{4\pi} * 2\pi * \frac{1}{R}$$

$$= 0.75 \times 10^{-23} \, Wb$$

Suppose the applied field is 100 Oe 100 Hz pure sin wave, and the detection coil has 500 turns. According to Faraday's law of induction, the picked-up voltage is:

$$v(t) = n\frac{d(\emptyset(t))}{dt} = n\frac{d(\emptyset_0 \times \cos(\omega t))}{dt}$$

$$= n\emptyset_0\omega \times \sin(\omega t)$$

$$= 500 \times 0.75 \times 10^{-23} \times 2\pi \times 100 \times \sin(\omega t)$$

$$= 0.23 \times 10^{-16} \times \sin(\omega t)\ \ volt$$

For our DAQ NI USB-6281, the minimum voltage range sensitivity is about 0.8 μV, so the minimum amount of MNPs detectable is:

0.8e-6/1.3e-16 = 3.4e10.

The SHS30 concentration is 0.31nmol/mL=1.87e14 MNPs/mL, and that makes the minimum detection limit to be 3.4e10/1.87e14=1.8e-4mL=180nL, that is 180ng Fe.

The more accurate to calculate the detection limit should consider the MNPs magnetic noise, magnetic field noise, cancelation effect of magnetization in the differentially wound detection coil pair, thermal noise of detection coil, noise figure of instrumentation amplifier, and tone measurement method.

2.3 Mixing Frequency Method

2.3.1 Introduction to the Mixing Frequency Method

To differentiate the MNPs from the background signal, the magnetization of them needs to be compared. MNPs are superparamagnetic, and part of the background signal is from paramagnetic material. As shown in Figure 1-1 superparamagnetic MNPs saturate much easier than paramagnetic material. Based on this property, when an ac magnetic field is applied as shown in Figure 2-6, the MNPs will be driven into saturation region while paramagnetic background is still in linear region. The nonlinear magnetization will generate higher harmonic signals on the pick-up coil. These higher harmonics are very specific to the MNPs, thus can be used for MNPs detection. Noticing that due to the rotational symmetry, the magnetization only contains the odd higher harmonics.

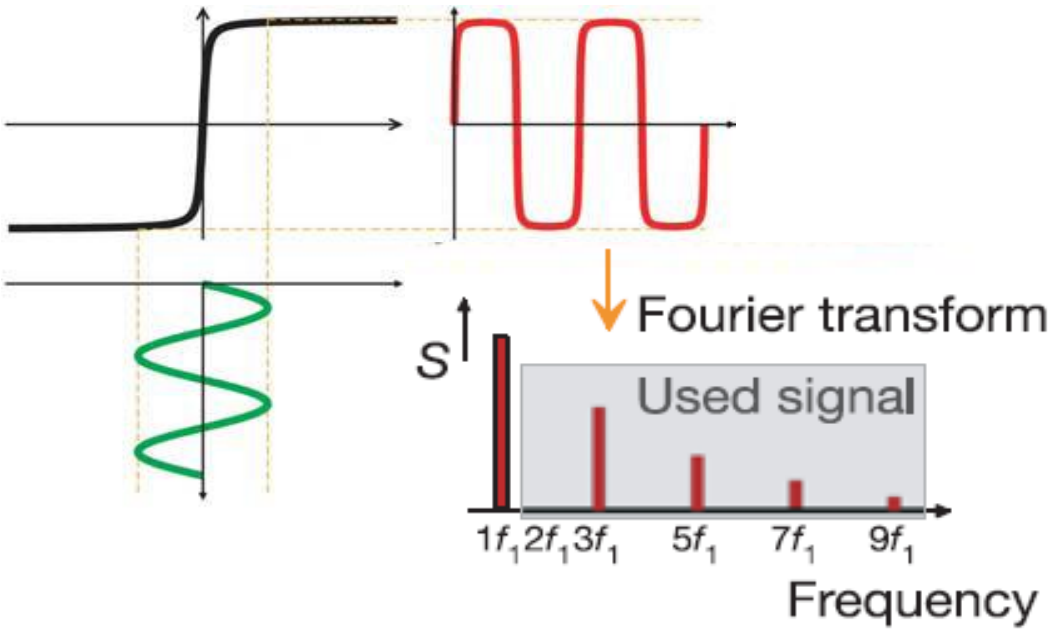

Figure 2-6 Schematic of magnetization of MNPs under an ac field, in time and frequency domain.

In order to achieve highly sensitive detection, the field strength needs to be big enough to generate strong signal of harmonics. On the other hand, Faraday's law of induction requires high frequency to generate big voltage on the pick-up coil.

However, the power amplifier that drives the excitation coils can only output a certain amount of power, and the power consumption is proportional to the current and frequency. Big field strength and high field frequency cannot be achieved at the same time. In order to solve this dilemma, a mixing-frequency method[21] has been used to detect the nonlinear magnetization of MNPs per testing sample by measuring the amplitude of the mixing frequency signals and thereby avoid the high noise at the fundamental frequencies[22,23]. A magnetic field with low frequency (e.g. f_2=10 Hz) and large amplitude drives the MNPs into their nonlinear saturation region periodically.Another magnetic field with higher frequency (e.g. f_1=20 kHz), and with a relatively small amplitude due to the inductance of excitation coil, is used to transfer the nonlinearity into the mixing frequency signals, such as $f_1 + 2 f_2$ (20.02 kHz). In this higher frequency region, the detection coil has higher output voltage amplitude, and the measurement system has lower 1/f noise, thus the mixing-frequency method can greatly improve the signal-to-noise ratio.

2.3.2 Theory of the Mixing Frequency Method

Superparamgnetic nanoparticles with small sizes are typically being used for biological applications to avoid the aggregation as well as any negative influence without external field. Its magnetization curve can be expressed as:

$$M = M_S \times L(\frac{m_0 \mu_0 H}{k_B T}) \quad (1),$$

WhereM_S is the saturation magnetization,m_0 is the magnetic moment of a singleparticle, $\mu_0$is the magnetic permeability of vacuum, $H$is the applied field, k_B is the Boltzmann constant, T is the absolute temperature, and $L$is the Langevin function.

Two sinusoidal magnetic fields are applied simultaneously: one with low amplitudeA_1, high frequencyf_1, written as$A_1\cos(2\pi f_1 t)$; the other with high amplitudeA_2, low frequencyf_2, written as$A_2\cos(2\pi f_2 t)$. The sum of these two fields (H) is transferred to magnetization (M) byLangevin function. Taylor Expansion near

zero magnetization shows that, besides the linear response, the major mixing components are as the following22:

$$[A_1\cos(2\pi f_1 t)+A_2\cos(2\pi f_2 t)]^3=\ldots+\frac{3}{4}A_1A_2{}^2\cos[2\pi(f_1\pm 2f_2)t]+\ldots \quad (2)$$

There are two relaxation mechanisms for MNPs. The physical rotation of particle in the viscous medium is called Brownian relaxation, and magnetic dipole flipping inside a stationary particle is calledNéel relaxation. Brownian relaxationdepends on an effective hydrodynamic volume.Néel relaxation depends on magnetic volume. The total relaxation process is a parallel model of these two relaxation schemes, but Brownian relaxation dominates when MNP's diameter is large, e.g. iron oxide MNP's diameter is larger than 20 nm[24]:

$$\tau_{total}\approx\tau_B=\frac{3\eta V_H}{k_BT} \quad (3),$$

where η is the viscosity of the carrier or matrix fluid, and V_H is the effective hydrodynamic volume of MNP.

When the frequency of ac applied field is low, the particles' magnetization can follow the excitation field tightly, and the susceptibility χ is a real number.Asthe excitation frequency increases, the particles' magnetization cannot follow the excitation field, and the relaxation processes introduce a phase in the complex ac susceptibility. The relationship between relaxation time τ and phase φ of ac susceptibility can be calculated using Debye model[25].

$$\chi(\omega)=\frac{\chi_0}{1+j\omega\tau}=\frac{\chi_0}{\sqrt{1+(\omega\tau)^2}}e^{-j\tan^{-1}(\omega\tau)}=|\chi|e^{j\varphi} \quad (4),$$

whereχ_0 is the static susceptibility and ω is the angular frequency. Assuming the particles' magnetization has a phase delay$\varphi_1$to the high frequency field and a phase delayφ_2 to the low frequency field, the mixing-frequency component of magnetization becomes:

$$[A_1\cos(2\pi f_1 t-\varphi_1)+A_2\cos(2\pi f_2 t-\varphi_2)]^3=\ldots+\frac{3}{4}A_1A_2{}^2\cos[2\pi(f_1+2f_2)t-\varphi_1-2\varphi_2]+\ldots$$

(5)

The total relaxation phaseφ_1+2φ_2 can therefore be determined by measuring the

phase of the mixing frequency at f_1+2f_2.If one frequency (e.g. f_2) is fixed, and the other frequency (e.g. f_1) is swept, the relaxation phase $\varphi_1+2\varphi_2$alongf_1 will show the relationship between φ_1 andf_1. Either one of f_1 and f_2 can be swept depending on whether high frequency region or low frequency region is of interest.

2.3.3 Experimental setup

Our search-coil based Susceptometry setup includes two excitation coils that generate10 Hz ac field with 100 Oe amplitudeand20 kHz ac field with 10 Oe amplitude, respectively. One pair of pick up coils with differentially wounded 500 rounds is installed. An instrumentation amplifier connected to a digital acquisition card (DAQ) is used for the signal amplification. LabVIEW program for the instrument control and Matlab program for signal processing are installed in the computer for controlling the whole setup.

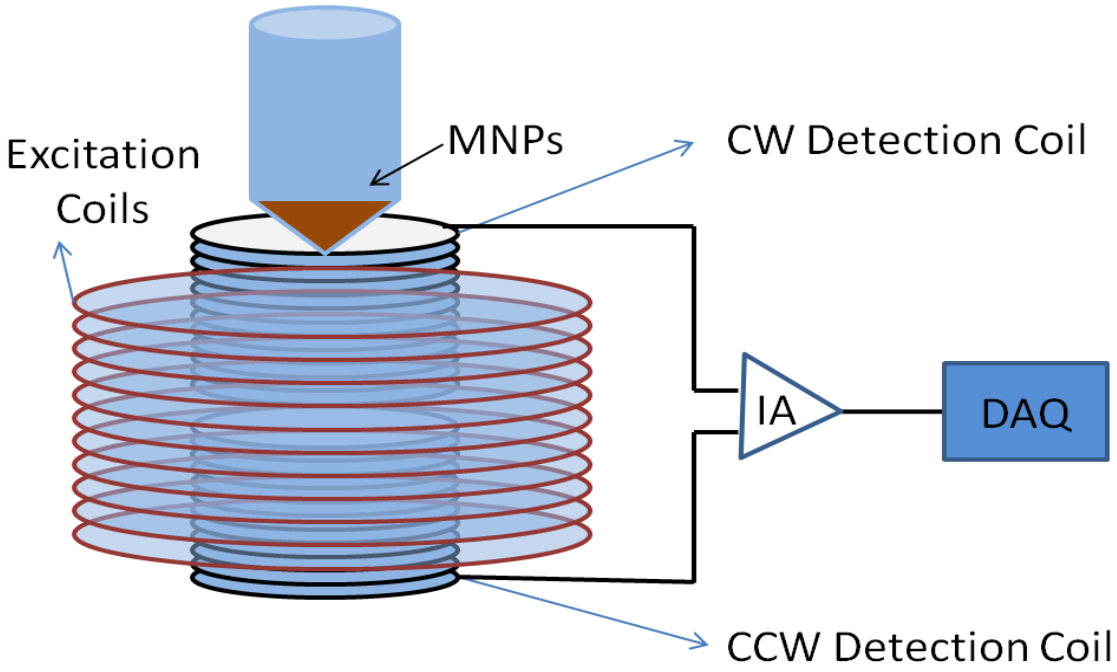

Figure 2-7 Schematic of experimental setup.

2.3.4 MNPs detection

$Fe_{40}Co_{60}$ MNPs are used for the demonstration of MNPs detections. In the room temperature, the SQUID measurement in Figure 2-8 shows that the sample is superparamagnetic. By applying two magnetic fields, the magnetization responds not only to these two frequencies respectively in Figure 2-9, but also generate mixing frequencies at $f_1 \pm 2f2$as shown in Figure 2-10.

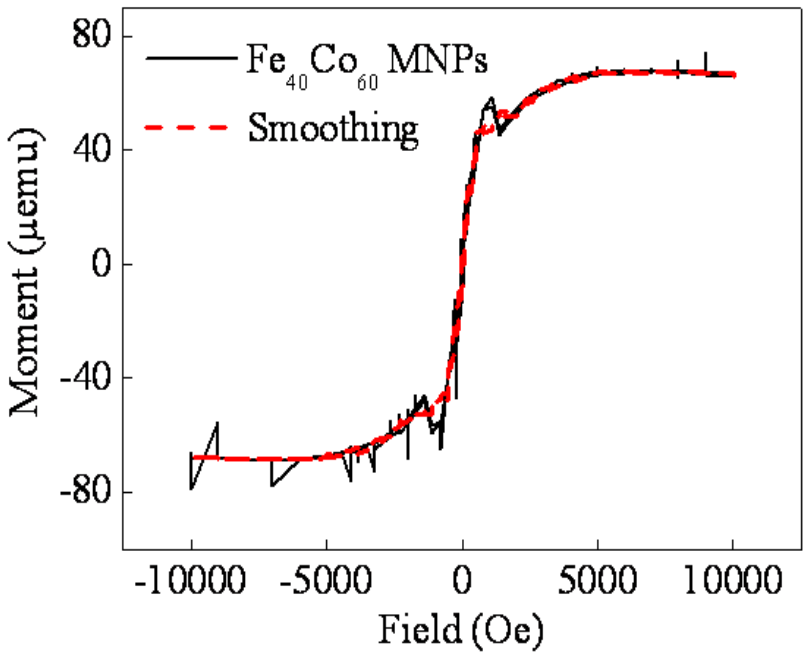

Figure 2-8 M-H loop of Fe40Co60 MNPs sample at room temperature measured by SQUID.

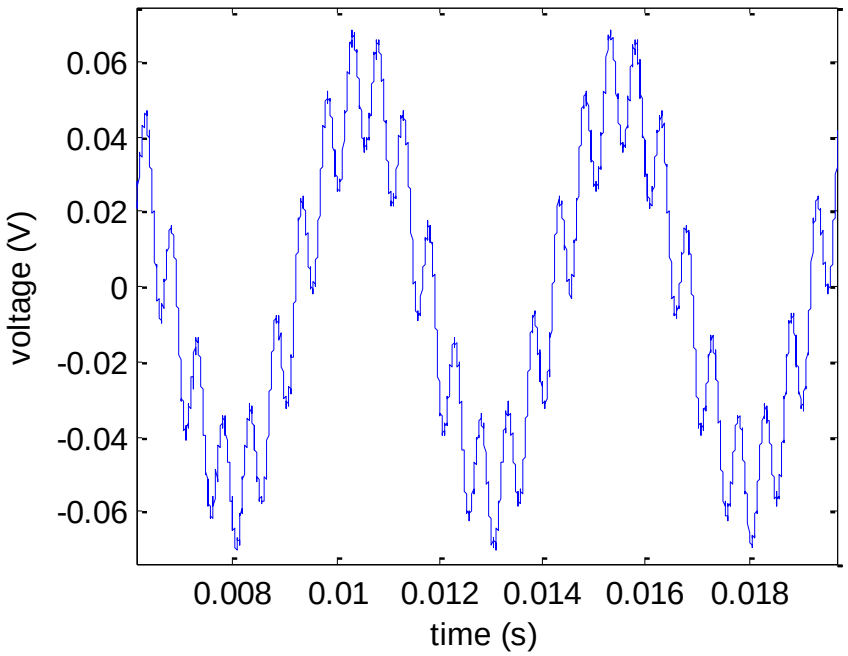

Figure 2-9 the voltage signal from the pick-up coil in time domain.

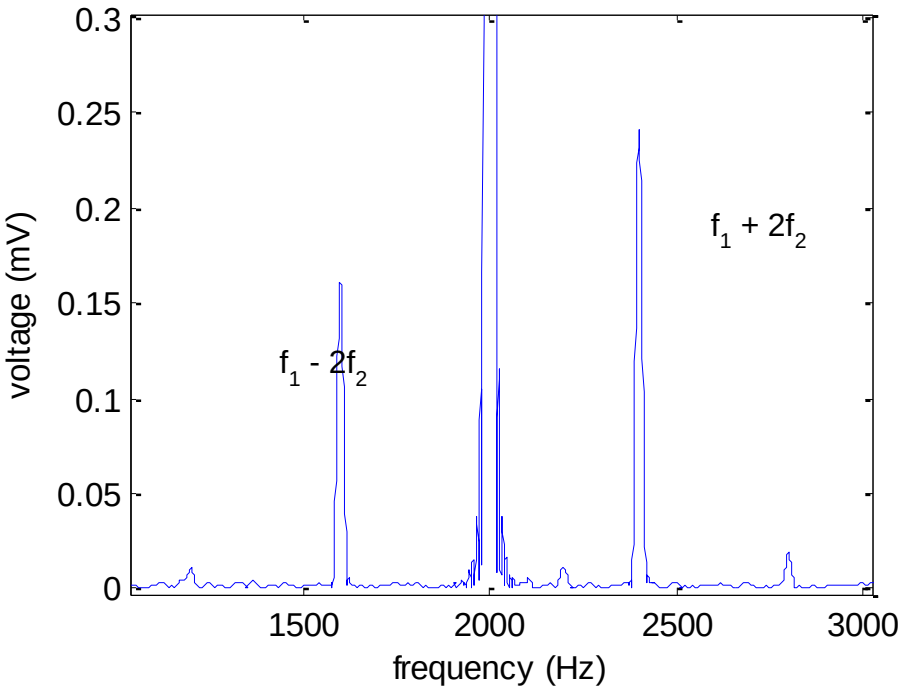

Figure 2-10 the voltage signal from the pick-up coil in frequency domain.

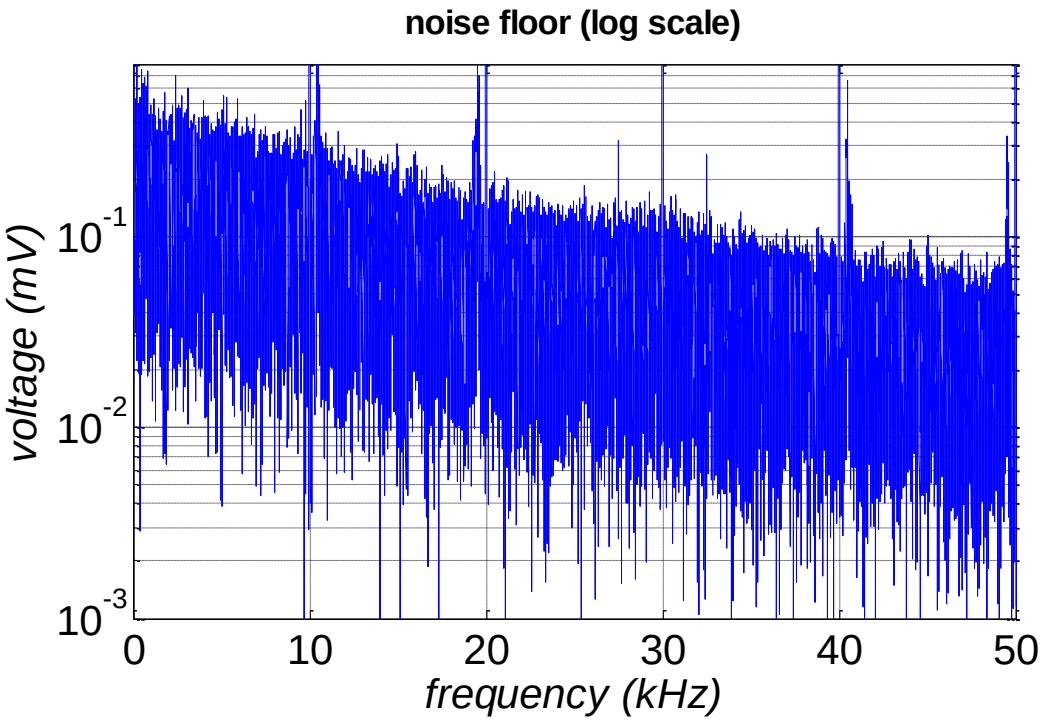

Figure 2-11 The noise floor of the detected signal.

The voltage signal after being amplified with a gain of 10000 is fed to a DAQ. The noise floor as shown in Figure 2-11 has a typical 1/f noise floor. This again explains why high frequency detection is required. To test the limit of detection, 25nm SPIO nanoparticles are used.

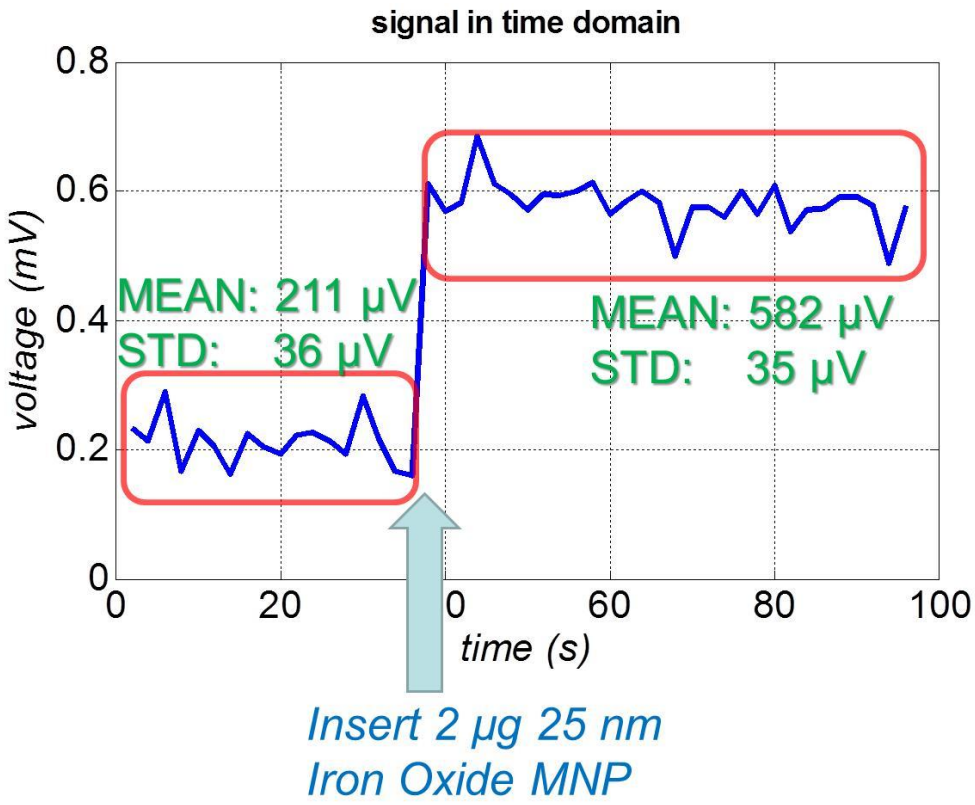

Figure 2-12 Real time detection of 25nm SPIO particles.

2μg 25nm SPIO is inserted into the detection coil around time 0. The noise is characterized by the standard deviation (STD) of the consecutive measurements. The STD is about 36μV, and the signal is about 370μV. Suppose 10 experiments are performed on this sample, the STD should decrease to $36\mu V/\sqrt{10}=11\ \mu V$. Then the signal to noise ratio (SNR) =370/11=33.6. So the limit of detection can be estimated by limiting the minimum signal to twice the noise, LOD = *2 μg /33.6 *2 = 119 ng.*

2.3.5 Theoretical Limit of Detection (LOD) by Mixing Frequency Method

Suppose the applied fields are $A_1\cos(2\pi f_1 t)$ = 1Oe*cos(2π**20000**t) and $A_2\cos(2\pi f_2 t)$ = 100Oe*cos(2π**10**t). At 100 Oe, the Langevin factor is

$\frac{m_0\mu_0 H}{k_B T} = 0.009662H = 0.9662$. Then the mixing terms will be

$$M = M_S \times L(\frac{m_0\mu_0 H}{k_B T})$$
$$\approx M_S \times \frac{m_0\mu_0}{3k_B T} H - M_S \times \frac{1}{45}(\frac{m_0\mu_0}{k_B T})^3 H^3 + ...$$

$$= .M_S \times \{...\frac{m_0\mu_0}{3k_B T} A_H \cos[2\pi(f_H)t] + \frac{m_0\mu_0}{3k_B T} A_L \cos[2\pi(f_L)t] +$$
$$+ \frac{1}{60}(\frac{m_0\mu_0}{k_B T})^3 A_H {A_L}^2 \cos[2\pi(f_H + 2f_L)t] + \frac{1}{60}(\frac{m_0\mu_0}{k_B T})^3 A_H {A_L}^2 \cos[2\pi(f_H - 2f_L)t] + ...\}$$

$$= M_S \times \{...0.00322A_H \cos[2\pi(f_H)t] + 0.00322A_L \cos[2\pi(f_L)t] +$$
$$+ 1.5e-8A_H {A_L}^2 \cos[2\pi(f_H + 2f_L)t] + 1.5e-8A_H {A_L}^2 \cos[2\pi(f_H - 2f_L)t] + ...\}$$

$$= M_S \times \{...0.0032\cos[2\pi(f_H)t] + 0.32\cos[2\pi(f_L)t] + 1.5e-4\cos[2\pi(f_H + 2f_L)t] + 1.5e...$$
$$-4\cos[2\pi(f_H - 2f_L)t] + ...\}$$

The above equation shows that the magnetization of mixing terms to that of low frequency (100Hz) field is 1.5e-4:0.32=1:2133. Section 2.2 calculates 180ng Fe is the LOD for the low frequency. Considering the 2133:1 magnetization ratio and 100:20000 frequency ratio, the LOD for the mixing frequency is180ng*2133/200=1.92μg.

2.4 Multi-tone Mixing-frequency method

Real-time magnetization of SMG30 samples can be digitized by DAQ shown in Figure 2-13. The magnetization shows nonlinear responses (bottom figure) to the applied fields (top figure). When the 10 Hz low frequency strong field reaches

maximum absolute amplitude (e.g. 0.125s, 0.175s, 0.225s, 0.275s), the MNPs show smaller magnetization response to the high frequencies due to the saturation of the nonlinear susceptibility. According to Faraday's law of induction, the electrical potential from the pick-up coil is proportional to the frequency of the magnetization. Although MNPs response mainly to 10Hz field, the higher frequency responses of magnetization are picked up by the coil. The high frequency picked-up voltage signal is modulated by the 10Hz field, and mixing frequencies are generated.

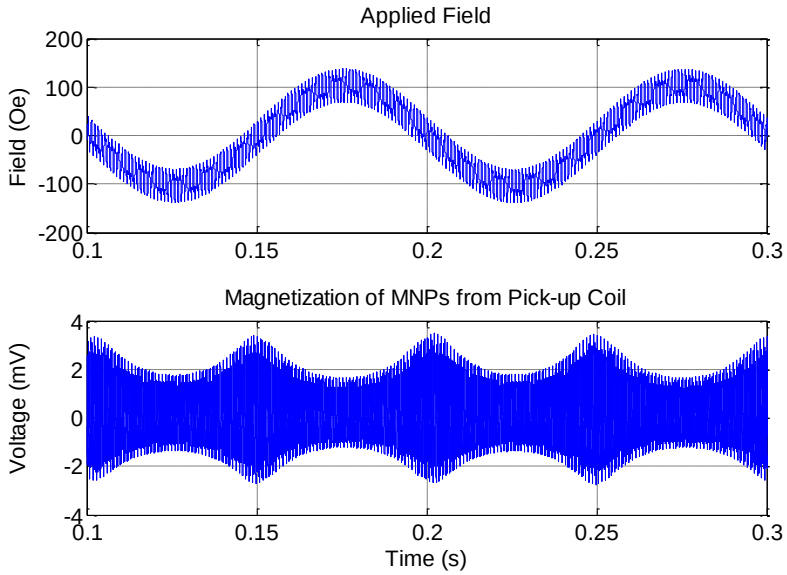

Figure 2-13 Signal from pick-up coil is digitized and recorded in time domain. The applied field (top) contains low frequency 10 Hz and multi-tone high frequencies (1 kHz, 5 kHz, 10 kHz, 15 kHz, and 20 kHz). The magnetization of MNPs (bottom) shows the periodic nonlinear response.

The number of field tones is limited by the driving capacity of power amplifier. Multiple tones will create higher PAPR (Peak to Average Power Ratio), and so the power amplifier will work in a low efficiency and high distortion region. To address this issue, low PAPR wave with multiple tones, such as square wave, can be used to probe the rich frequency responses of MNPs.

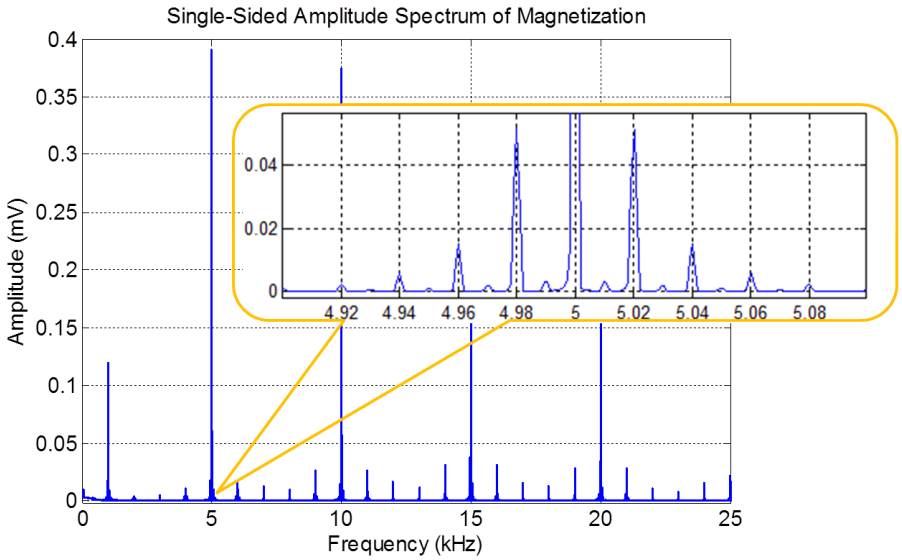

Figure 2-14 Amplitude Spectrum of Magnetization from the MNPs under multi-tone applied magnetic field.

Figure 2-14 gives a frequency overview of the magnetization from MNPs in the multi-tone field. Each tone generates multiple mixing frequencies. Using a Quadrature detection method, the phase of mixing-frequencies and the tone frequencies can be estimated. The amplitude of the mixing frequencies around 5 kHz is about 50 µV while the noise floor is about 1 µV, and this pushes the limit of detection to 0.2 µg/mL Fe or 6.2 pM concentration without any improvement by averaging.

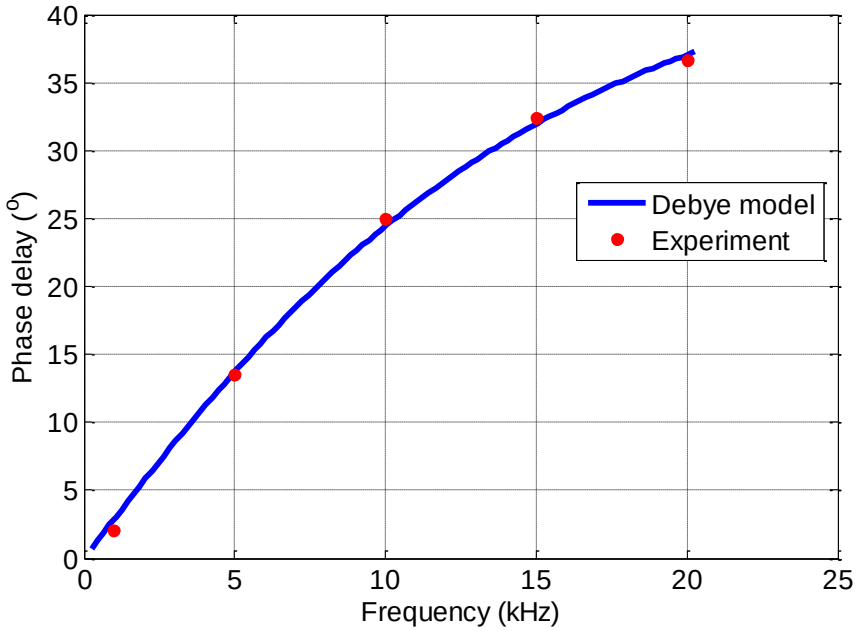

Figure 2-15 Phase delays of magnetization behind the field at 5 tones are measured at the same time.

The phase delay at five tones is plotted with red dots in Figure 2-15. Since the measurement of phase delays is an overall performance of MNPs with different hydrodynamic sizes, the size distribution can be estimated using Least Mean Square (LMS) method. Singular value decomposition (SVD) is one of the LMS methods that enable efficient and accurate estimation of the unknown variables (size distribution) from equations (phase delay)[32]. However SVD is not accurate when the number for phase delay measurements is less than the number of size distribution points, it is not applicable for the multi-tone method since the tone numbers are very limited. Fortunately most MNPs has a size distribution of Log-normal function[24],

$$f(d_h) = \frac{1}{\sqrt{2\pi}\beta d_h} e^{-\frac{\ln^2(d_h/d_{h0})^2}{2\beta^2}}$$

where d_{h0} and β are the mean and the standard deviation of hydrodynamic sizes. Under this assumption, there are only two unknown variables d_{h0} and β that needs to be estimated from the measured phase delay φ at different frequencies ω_i. The fitting

system shown below can be modeled using Matlab function *ffun=fittype(expr)*, with *expr* representing the model:

$$\varphi(\omega_i) = \angle \sum_i f(d_{hi}) \frac{\chi_0}{1 + j\omega_i \tau_i}$$

Then, the function *fit(xdata, ydata, ffun)* uses this model to get a reasonable estimation of d_{h0}= 36.5 nm and β= 0.083. Based on this estimated size distribution, phase delay over frequency is plotted in blue line in Figure 2-15. The experimental data and the estimation model matches well.

The multi-tone method uses one pick-up coil to measure different frequencies simultaneously and thus enables a very robust correlation of measurements at different frequencies. This is in contrast to the frequency sweeping method, which may be subject to system-level drift. Also, the multi-tone method is time efficient, so the size distribution of MNPs can be measured consecutively in real time, which is critical for many applications such as dynamic detection of binding kinetics and interaction affinities between biomolecules.

2.5 Relaxation modulation by field amplitude

2.5.1 Brownian relaxation modulation

A 10 µL SHP35 sample with a concentration of 5 mg/mL Fe is used for the test. SHP35 has 35nm Magnetite core and is coated with monolayer oleic acid and monolayer amphiphilic polymer which added a few nanometers to its hydrodynamic size. As shown in Figure 2-17 measured by a Dynamic Light Scattering (DLS) instrument, the sample is well dispersed in water solution and has a narrow distribution of hydrodynamic size. Under ac magnetic field, due to the large size of the magnetic core, Brownian relaxation will dominate, and MNPs will physically rotate in the solution.

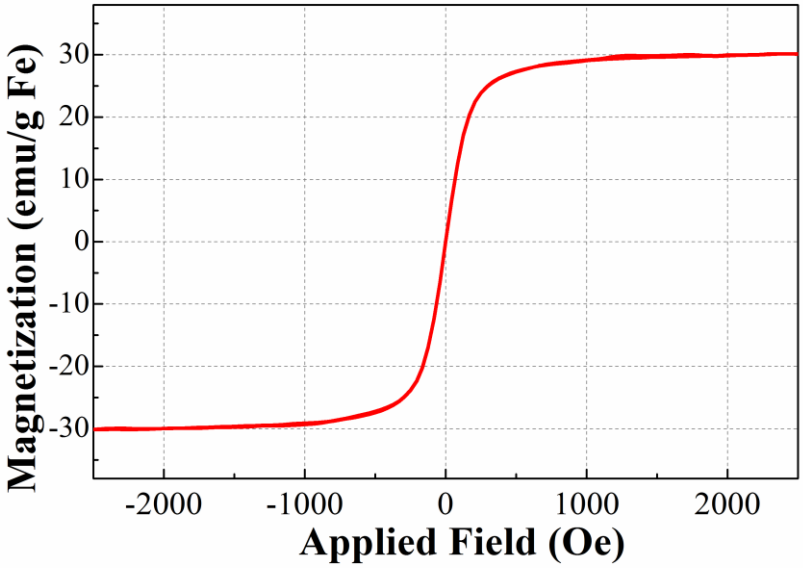

Figure 2-16 Magnetization curve of Iron Oxide Nanoparticles (SHP35, Ocean NanoTech, Springdale, AR) in water solution at room temperature measured by VSM.

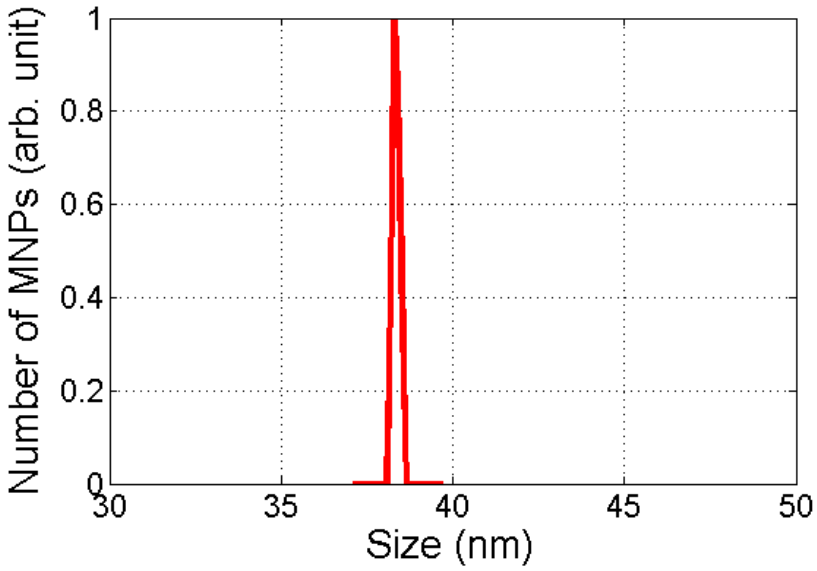

Figure 2-17 Hydrodynamic distribution of Iron Oxide Nanoparticles (SHP35, Ocean NanoTech, Springdale, AR)in water solution at room temperature measured by DLS.

A 10 Hz 99 Oe magnetic field is applied to saturate the SHP35 samples periodically, and a high frequency field is applied to generate mixing-frequency signals. The high frequency field is swept from 2 kHz to 20 kHz, and the measured phase delay φ_H to the high frequency is plotted in the red line in Figure 2-18. Phase delay φ_L to the low frequency is a small constant number and is not shown here. An interesting finding is that when decreasing the amplitude of 10 Hz field to 66 Oe and further to 33 Oe, the phase delay φ_H of MNPs increases. Similar results have been reported and discussed in other studies [26,27].

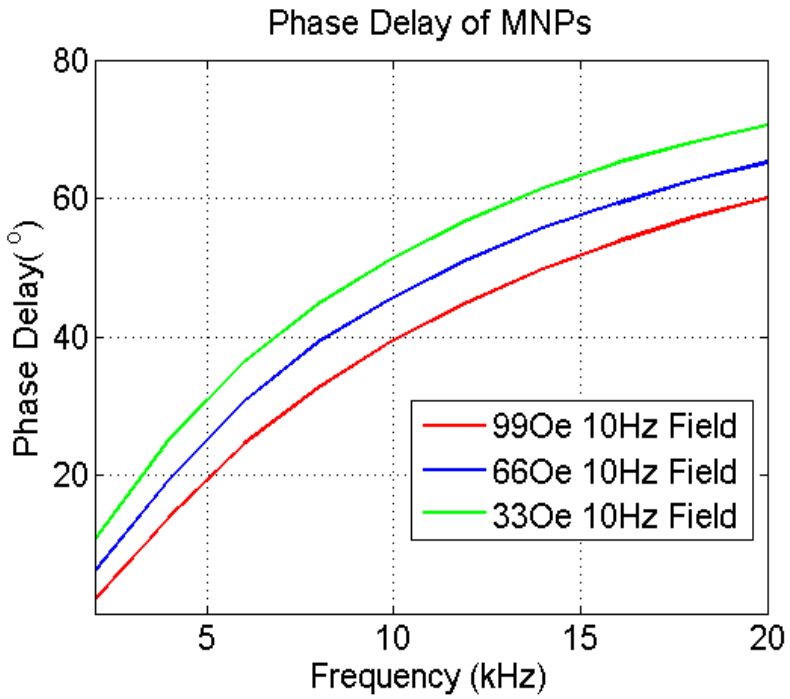

Figure 2-18 High frequency field is swept from 2 kHz to 20 kHz, and the phase delay of MNPs is measured at each frequency. A 10 Hz field is applied to saturate the MNPs with the peak amplitude of 33 Oe, 66 Oe and 99Oe respectively.

To explain the field amplitude dependence of the phase delay, magnetization of SHP35 samples is digitized by a Digital AcQuisition card (DAQ) in the time domain as shown in Figure 2-19. The magnetization shows nonlinear responses

(middle figure) to the applied fields (top figure). When the 10 Hz low frequency strong field reaches the maximum absolute amplitude (e.g. at 0.025 s, 0.075 s), the MNPs show smaller magnetization response to the high frequencies due to the saturation of the nonlinear susceptibility. The amplitude of the high frequency response can be interpreted as the first derivative of the MH curve[28]. According to the Faraday's law of induction, the electrical potential from the pick-up coil is proportional to the frequency of the magnetization. Although MNPs respond mainly to 10 Hz field, the higher frequency responses of magnetization picked up by the coil are much stronger. The high frequency picked-up voltage signal is modulated by the 10 Hz field, and mixing-frequencies are generated. The bottom figure of Fig. 4 shows that not only is amplitude of magnetization modulated by the 10 Hz field, but the phase of magnetization is also modulated. The 10 Hz field changes much slower than 20 kHz field, and thus can be viewed as a quasi-static field. During each period of the 20 kHz field, the phase of the magnetization can be measured using a Quadrature detection method. When this quasi-static 10 Hz field reaches zero amplitude, MNPs have the maximum phase delay to the 20 kHz field. This indicates that SHP35 has smaller Brownian relaxation time in a bigger applied offset magnetic field. The phase variation means that the measured φ_H depends on the field amplitude and is related to the overall phase delay in one period of low frequency.

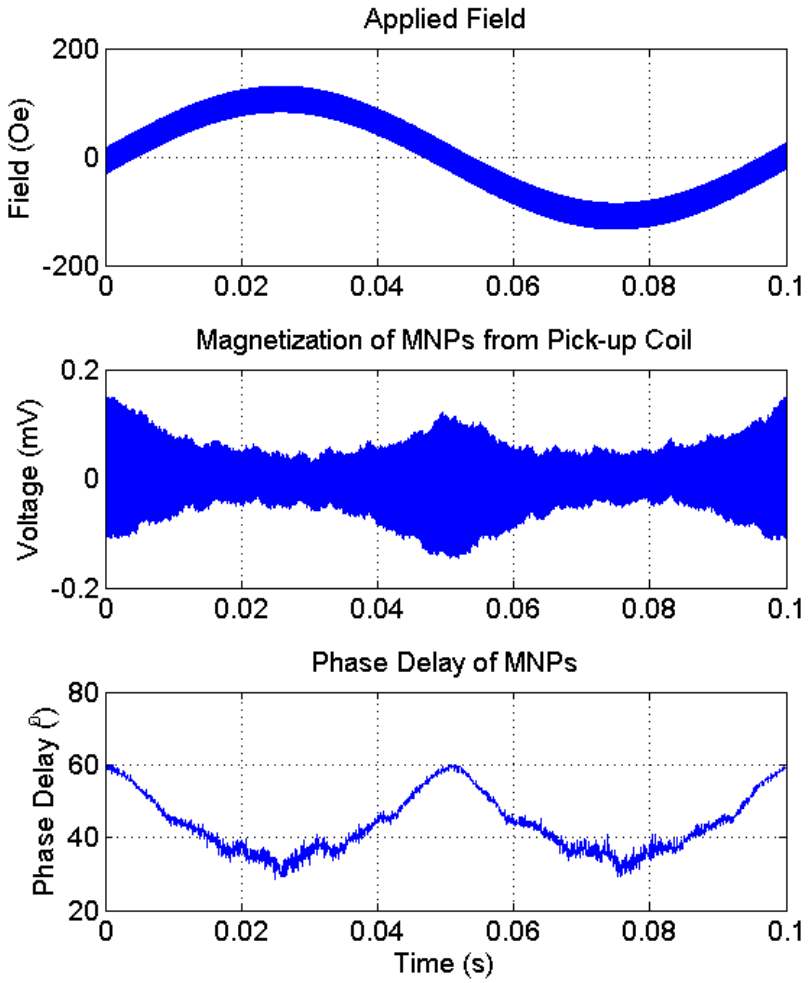

Figure 2-19 Signal from pick-up coil is digitized and recorded in time domain. The applied field (top) contains 10 Hz 99 Oe field and 20 kHz 10 Oe field. The Brownian magnetization of MNPs (middle) shows periodic nonlinear response. The phase delay of MNPs (bottom) due to Brownian relaxation also shows periodic response.

2.5.2 Néel relaxation modulation

The same phenomenon is observed for Néel relaxation in superparamagnetic MNPs with iron oxide core of 12 nm, on average, plus a fatty acid coating and a polymer coating. These MNPs has been tested for the purpose of hyperthermia, and they generate the same amount of heat in liquid solution and in agarose gel, which indicates that Néel relaxation dominates the magnetization dynamics. Figure 2-20 shows the phase delay of Néel magnetization behind the 20 kHz field during one period of 10Hz strong field with the amplitude of 33Oe (green), 66Oe (blue) and 99Oe (red). The phase of 20 kHz magnetization is traced in real time using Quadrature detection. At zero quasi-static field, phase delay reaches maximum, and drops as the field amplitude increases.

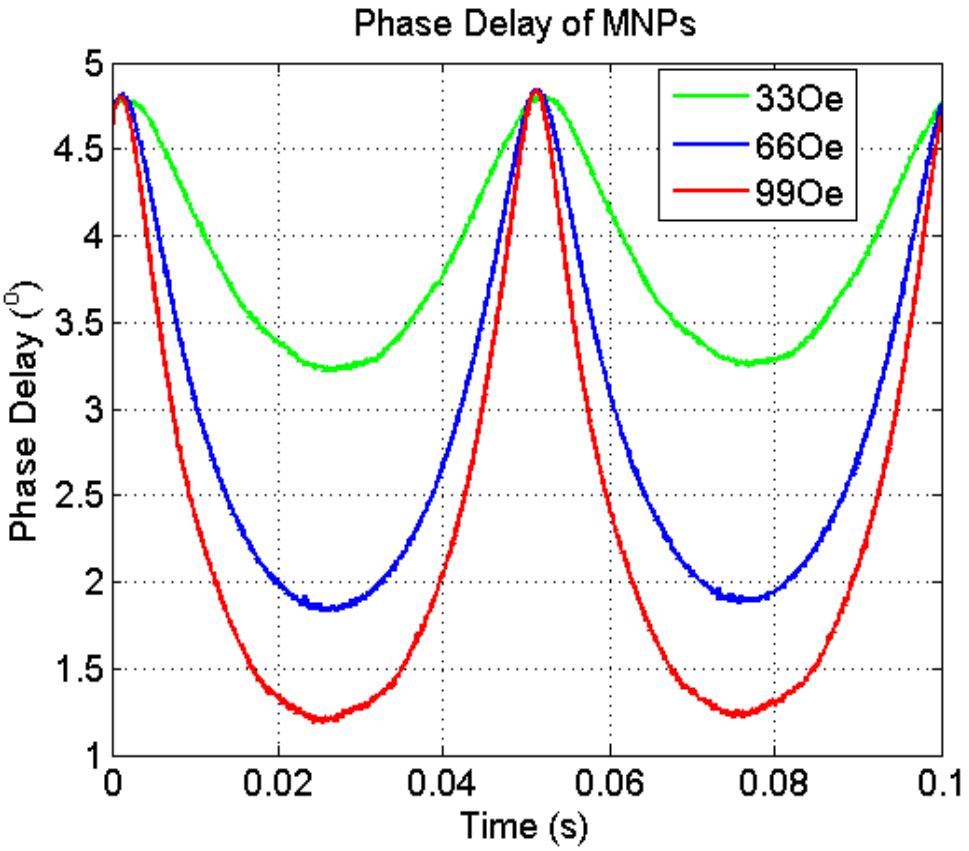

Figure 2-20 Phase delay of Néel magnetization behind the 20 kHz field is recorded during one period of 10 Hz strong field with the amplitude of 33 Oe (green), 66 Oe (blue) and 99 Oe (red).

Néel relaxation model in Figure 2-21 intuitively shows a simple treatment that the $\ln(\tau_N)$ is positively correlated with the energy barrier. When an offset field H_0 is applied, the energy barrier decreases (by $M H_0$), as do τ_N and $\varphi = \tan^{-1}(\omega\tau_N)$. A more theoretical treatment of relaxation time can be found in Ref. [4]. In the case of small ξ, $\tau_N \approx \tau_{N0}(1-2\xi^2/15)$, where τ_{N0} is the Néel relaxation time in zero static field; in the case of large ξ, $\tau_N \approx \tau_{N0}/\xi^{29}$. Since the MNPs used for Néel relaxation measurement form clusters, the effective field energy becomes much bigger, and the measurement results in Figure 2-20 agrees with the second case where ξ is comparably large.

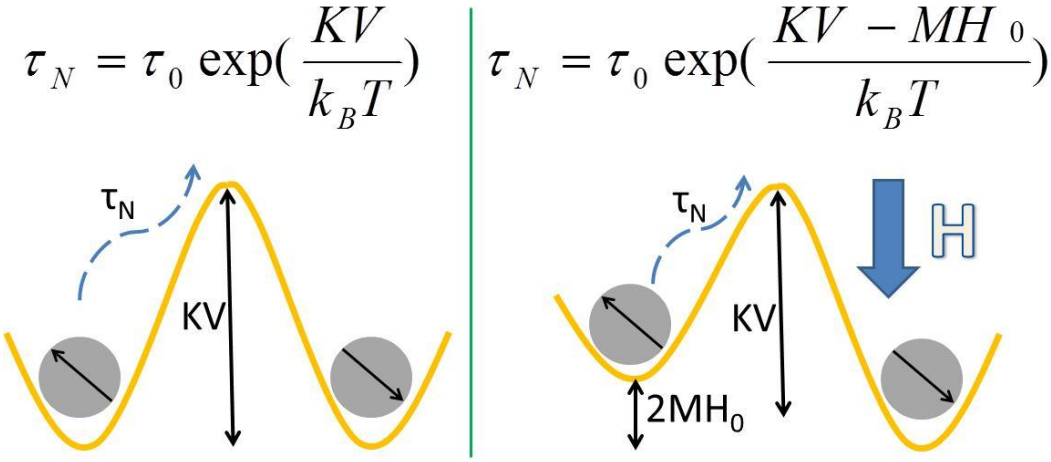

Figure 2-21 Left figure: energy barrier under zero offset field; Right figure: energy barrier under an offset field.

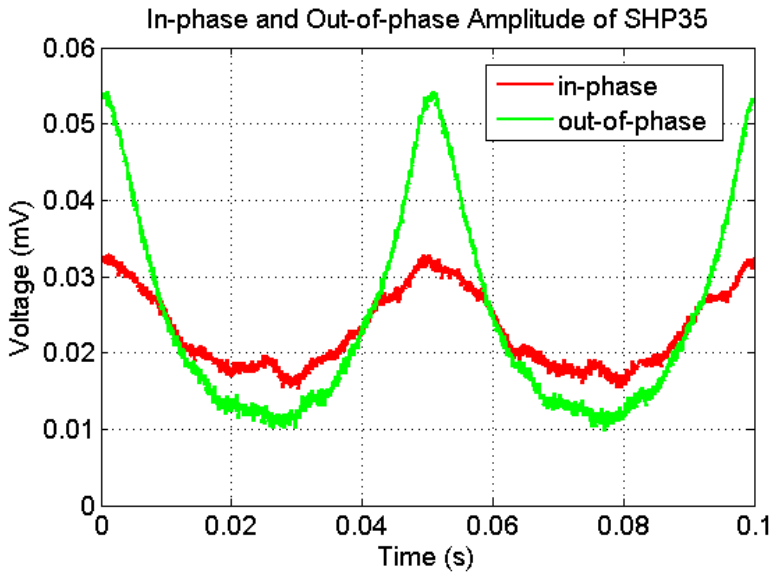

Figure 2-22 In-phase and Out-of-phase Amplitude of Brownian relaxation of SHP35 behind the 20 kHz field is recorded in one period of 10 Hz 99 Oe field.

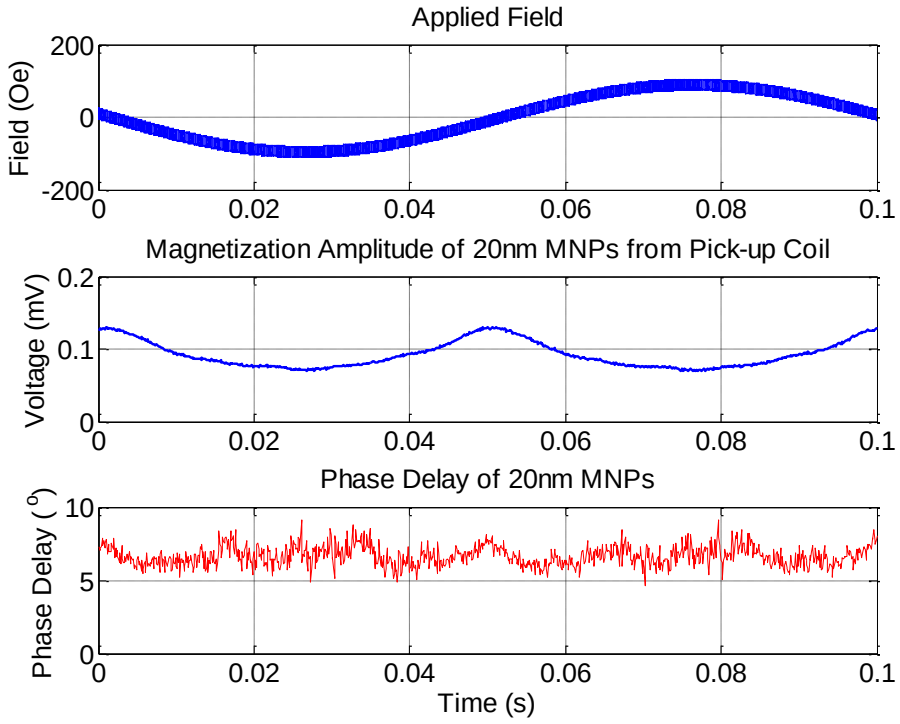

Figure 2-23 Signal from pick-up coil is digitized and recorded in time domain. The applied field (top) contains 10 Hz 99 Oe field and 20 kHz 10 Oe field. The magnetization of SHS20 (middle) shows a periodic nonlinear response. The phase delay of SHS20 (bottom) due to Brownian relaxation also shows periodic response.

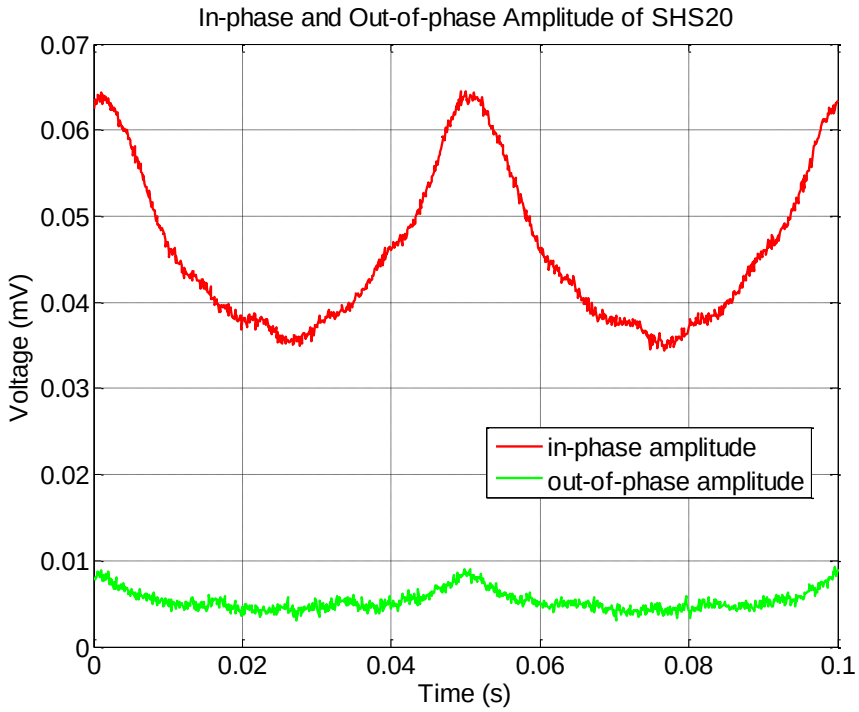

Figure 2-24 In-phase and Out-of-phase Amplitude of relaxation of SHS20 behind the 10 kHz field is recorded in one period of 10 Hz 99 Oe field.

Figure 2-23 and Figure 2-24 show the magnetization response from SHS20. For this MNPs, the phase is not modulated by the low frequency field, only the amplitude is modulated.

The discussion above shows that both the amplitude and the phase of the MNPs are modulated by a frequency $2f_L$. Both the modulations lead to a mixing frequency $f_H \pm 2f_L$. Figure 2-22 shows that in-phase and out-of-phase amplitudes of SHP35 are modulated by a frequency $2f_L$. The out-of-phase amplitude is affected more by the quasi-static field. All these factors increase the complexity in susceptibility modeling. However, this study improves the previous understanding of the mixing-frequencies from the MNPs, and can help to tailor MNPs to specific application, such as MPI where gradient static field is used to determine the location of MNPs. Also, this study provides an experimental method to design new detection

instruments. For example, if SHP35 MNPs are used as detection probes, the out-of-phase detection will be more effective, because it not only avoids the interference from the high frequency field but also is heavily modulated by the low frequency field.

2.5.3 Simulation of relaxation modulation

Both the amplitude and phase of the high frequency f_H magnetization are modulated by the low frequency f_L field, and both modulations contribute to the amplitude and phase of the mixing frequencies $f_H \pm 2f_L$. How the modulations affect the amplitude and phase is complicated. Below analytical and simulation results are shown.

Under two magnetic fields: H = $A_H \cos(2\pi f_H t) + A_L \cos(2\pi f_L t)$, assume magnetization of MNP has phase delay $\varphi_H$to the high frequency field, and assume we can ignore the small phase delay φ_L to the low frequency field. The amplitude and phase of the magnetization at f_H are modulated by the low frequency field with factors m and n. So the magnetization can be written as:

$$M(t) = \cos\{2\pi f_H t - [\varphi_H - |n \times \cos(2\pi f_L t)|]\} \times [1 - |m \times \cos(2\pi f_L t)|]$$

The modulation factors $|n \times \cos(2\pi f_L t)|$ and $|m \times \cos(2\pi f_L t)|$ have a fundamental frequency of $2f_L$.When the phase of a sinusoidal wave $\cos(\omega_c n)$ is modulated by another sinusoidal wave $\cos(\omega_m n)$, the signal can be decomposed of mixing frequencies terms[30].

$$x[t] = \cos(\omega_c n + a\cos(\omega_m n))$$

$$x[t] = \cos(\omega_c n)\cos(a\cos(\omega_m n)) - \sin(\omega_c n)\sin(a\cos(\omega_m n))$$

$$x[t] = J_0(a)\cos(\omega_c n)$$

$$+J_1(a)\cos((\omega_c + \omega_m)n + \frac{\pi}{2}) + J_1(a)\cos((\omega_c - \omega_m)n + \frac{\pi}{2})$$

$$+J_2(a)\cos((\omega_c+2\omega_m)n+\pi)+J_2(a)\cos((\omega_c-2\omega_m)n+\pi)$$

$$+J_3(a)\cos((\omega_c+3\omega_m)n+\frac{3\pi}{2})+J_3(a)\cos((\omega_c-3\omega_m)n+\frac{3\pi}{2})+\cdots$$

Where $J_k(a)$ are the Bessel functions of the first kind, ω_c corresponds to f_H and ω_m corresponds to $2f_L$. The mixing frequency $f_H \pm 2kf_L$ should have a phase of $k\pi/2$. However, the amplitude modulation will also generate mixing frequency $f_H \pm 2kf_L$. The final mixing term $f_H \pm 2f_L$ will be from numerous combinations of phase modulation and amplitude modulation. The analytical solution will be so complicated that numerical simulation is used to help guide the study.

In the Matlab simulation, we try to simulate the situation in Figure 2-19 wheref_H =20000, f_L =10, and φ_H =60°. Now modulation factors m and n are swept to study the phase of $f_H + 2f_L$.In Figure 2-25, it showsMNP phase delay dependence on phase modulation factor n and amplitude modulation factor m. When amplitude modulation factor m is 0, only the phase modulation plays a role in generating the mixing frequencies $f_H \pm 2f_L$. However, the phase modulation decreases the phase delay φ_H.When the phase modulation n is fixed, the amplitude modulation m will also decrease the phase delay φ_H. When the amplitude modulation m is fixed, the phase modulation n will increase thephase delay φ_H. In Figure 2-26, both amplitude modulation factor m and phase modulation n will contribute the amplitudes of the mixing frequencies. However, the relationship between phase/amplitude and modulation factors m/n is too complicated to generalize an exact rule.

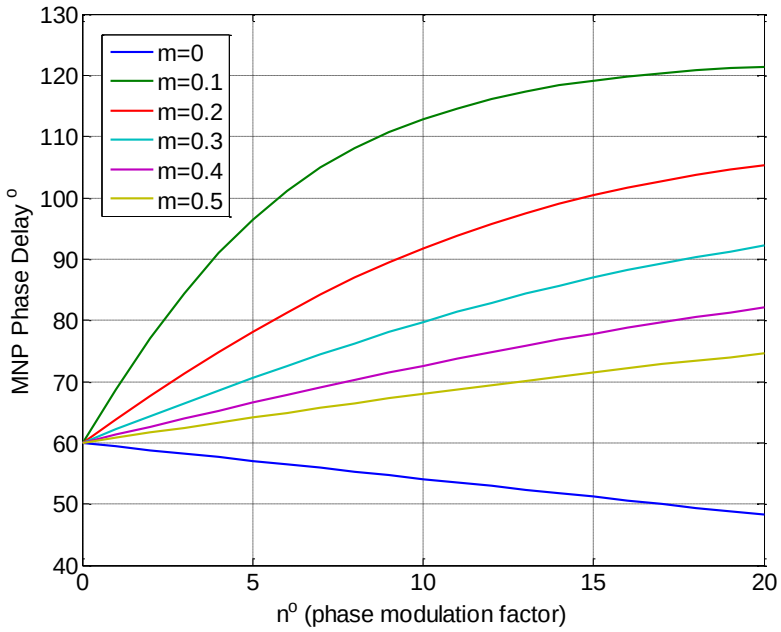

Figure 2-25 MNP phase delay dependence on phase modulation factor n and amplitude modulation factor m (simulation).

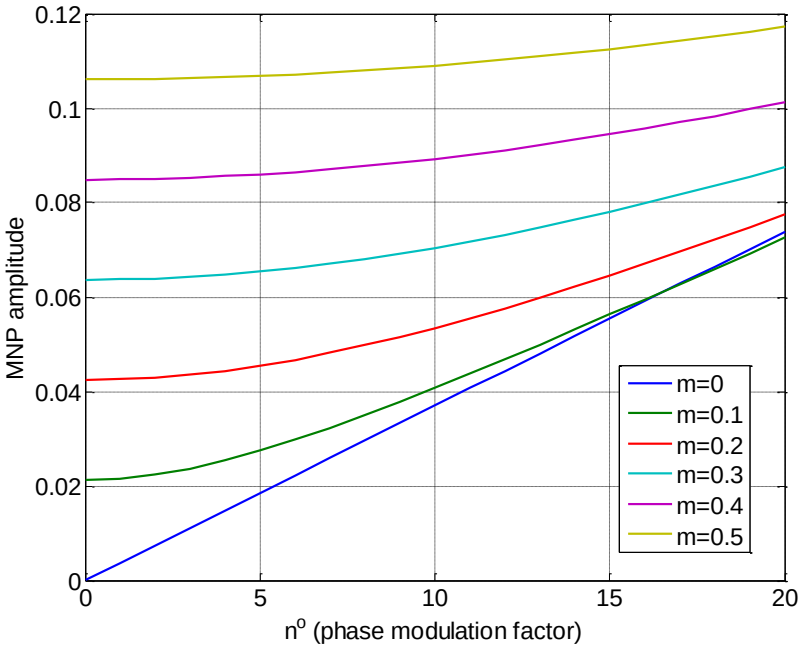

Figure 2-26 MNP amplitude dependence on phase modulation factor n and amplitude modulation factor m (simulation)

[13] J. Lenz, IEEE Proceedings, **78**, 973, (1990)

[14] Caruso, Michael J; Tamara Bratland; Carl H Smith, PhD; and Robert Schneider, "A New Perspective on Magnetic Field Sensing," Honeywell Inc, May 1998, www.ssec.honeywell.com/ magnetic/datasheets/new_pers.pdf

[15]http://www.boulder.nist.govdiv81881803MagneticDevicesandNanoStructuresindex.html

[16] Quantum Design, San Diego, CA, 'http://www.qdusa.com/products/ppms.html'

[17]Imego Institute, Göteborg, SWEDEN, 'http://www.imego.com/Products/dynomag/index.aspx'

[18]P.C. Fannin, B.K.P. Scaife, J. Magn.Magn.Mater.**72**, 95 (1988)

[19] Magnetic dipole, 11/9/2012, from 'http://en.wikipedia.org/wiki/Magnetic_dipole'

[20] http://www.oceannanotech.com/upload/090604131348592520yef2g1.pdf

[21] T.L. Paoli and J.F. Svacek, Rev. Sci. instrum., **47**, 9 (1976)

[22]Petr I. Nikitin, Petr M. Vetoshko, and Tatiana I. Ksenevich, J. Magn. Magn.Mater.**311**, 445 (2007)

[23]Hans-Joachim Krause, Norbert Wolters, Yi Zhang, Andreas Offenhausser, Peter Miethe, Martin H.F. Meyer, Markus Hartmann, and Michael Keusgen, J. Magn. Magn.Mater.**311**, 436 (2007)

[24] R.E. Rosensweig, J. Magn. Magn.Mater.**252**, 370 (2002)

[25]M.I. Shliomis, Yu.L. Raikher, IEEE Trans. Magn. **MAG-16**, 237 (1980)

[26]J Dieckhoff, M. Schilling, and F. Ludwig, "Fluxgate based detection of magnetic nanoparticle dynamics in a rotating magnetic field."*Appl. Phys. Lett.*, vol. 99, p. 112501, 2011

[27] T. Yoshida, K. Enpuku, J. Dieckhoff, M. Schilling, and F. Ludwig, "Magnetic fluid dynamics in a rotating magnetic field" J. Appl. Phys., vol. 111, pp. 053901, 2012

[28] T. L. Paoli and J. F. Svacek, "Derivative measurement by frequency mixing," Rev. Sci. Instrum., vol. 47, p. 1016, 1976

[29] W. T. Coffey, P. J. Cregg, and Y. P. Kalmykov, "On the theory of Debye and Néel relaxation of single domain ferromagnetic particles," *Advances in Chemical Physics*, vol. 83, p. 263, 1993

[30] http://crca.ucsd.edu/~msp/techniques/v0.11/book-html/node86.html

Chapter 3 Application of Mixing Frequency Method

1. 1 Brownian Relaxation Measurement

3.1.1 Brownian Relaxation Measurement by Mixing Frequency Method

Under two magnetic fields: H = $A_H \cos(2\pi f_H t) + A_L \cos(2\pi f_L t)$, the sum of these two fields (H) is transferred to magnetization (M) according to the Langevin function. Assuming the particles' magnetization has a phase delay φ_H to the high frequency field and a phase delay φ_L to the low frequency field, Taylor Expansion near zero magnetization shows that, besides the linear response, the major mixing components with no DC field are as the following[31]:

$$M = M_S \times L(\frac{m_0 \mu_0 H}{k_B T})$$

$$\approx M_S \times \frac{m_0 \mu_0}{3 k_B T} H - M_S \times \frac{1}{45} (\frac{m_0 \mu_0}{k_B T})^3 H^3 + \ldots$$

$$= \ldots + \frac{1}{60} (\frac{m_0 \mu_0}{k_B T})^3 A_H A_L{}^2 \cos[2\pi(f_H + 2 f_L)t - \varphi_H - 2\varphi_L + \pi] +$$

$$\frac{1}{60} (\frac{m_0 \mu_0}{k_B T})^3 A_H A_L{}^2 \cos[2\pi(f_H - 2 f_L)t - \varphi_H + 2\varphi_L + \pi] + \ldots$$

According to Faraday's Law of Induction, the voltage signal from the pick-up coil has a 90° phase shift from the magnetization of MNPs.

$$V \propto \frac{dM}{dt}$$

$$= \ldots + \frac{\pi}{30} (\frac{m_0 \mu_0}{k_B T})^3 A_H A_L{}^2 (f_H + 2 f_L) \cos[2\pi(f_H + 2 f_L)t - \varphi_H - 2\varphi_L + \frac{3}{2}\pi]$$

$$+ \frac{\pi}{30} (\frac{m_0 \mu_0}{k_B T})^3 A_H A_L{}^2 (f_H - 2 f_L) \cos[2\pi(f_H - 2 f_L)t - \varphi_H + 2\varphi_L + \frac{3}{2}\pi] + \ldots$$

The relaxation phase φ_H and φ_L can therefore be determined by measuring the phase of the mixing frequency at $f_1 \pm 2f_2$.

$$\varphi_H = -\frac{\varphi_{f_1+2f_2} + \varphi_{f_1-2f_2}}{2}$$

$$\varphi_L = \frac{\varphi_{f_1-2f_2} - \varphi_{f_1+2f_2}}{4}$$

3.1.2 Real-time Brownian Relaxation Measurement

Three commercial iron oxide MNPs samples (Ocean Nanotech, Springdale, AR) are used for Brownian relaxation study: SHP35 (MNPs with 35 nm core size, 4 nm oleic acid and amphiphilic polymer coating, 0.1 mL, 5 mg/mL in H_2O-Carboxylic Acid solution), IPG35 (SHP35 conjugated with around 10 nm protein G layer, 0.1 mL, 1 mg/mL), and IPG35-Ab (IPG35 conjugated with around 10 nm Goat anti-Human IgG (an antibody isotype of mammals) HRP with ratio 1:100, 0.1 mL, 1 mg/mL). Particle size distributions are measured by a Dynamic Light Scattering (DLS) instrument ('90 Plus Particle Sizer', Brookhaven Instruments Corp., Holtsville, NY) and are shown in the Figure 3-1. The DLS measurement results are consistent with the data provided by Ocean Nanotech. All the three samples are from the same batch of 35 nm iron oxide MNP core, so the wide hydrodynamic size distribution of IPG35-Ab shows that IPG35 binds with antibodies in a range of binding affinity. This is also confirmed by an independent gel electropherosis measurement (results not shown here).

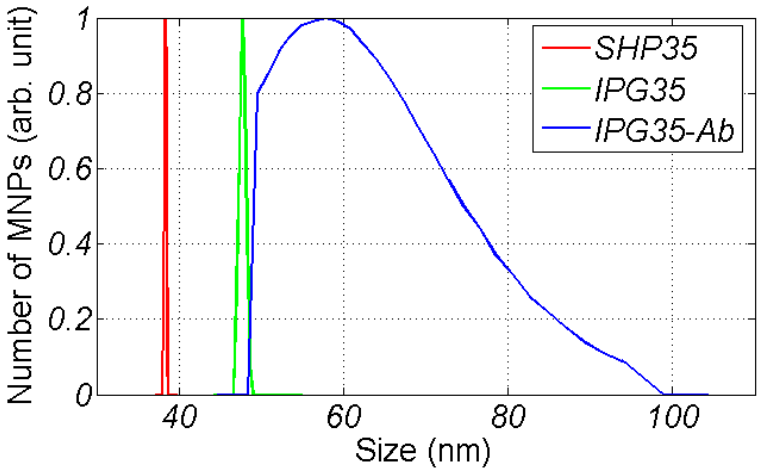

Figure 3-1 Size distributions of SHP35, IPG35 and IPG35-Ab samples measured by Dynamic Light Scattering (DLS).

We measured the MNPs' phase delay of these three samples under ac fields. Phase delay of the mixing-frequency signal is measured by scanning the frequency of f_1 up to 10 kHz. The results of 10 times average are shown in Figure 3-2. To prevent any temperature drift due to joule heating of the coil, tone bursts are applied rather than continuous ac field. The experimental results are fitted by the Debye model in Eq. (4). Since the particles are not monodispersed, the total susceptibility comes from the contributions of all MNPs with various sizes. As shown in the Figure 3-2, Debye model with the superposition of MNPs' hydrodynamic size distribution[32] is a good fit in our case, although it is argued that Debye model is only valid for small-amplitude (<1 kA/m)[33] low-frequency[34] applied ac field and a high frequency susceptibility χ_∞ is needed for the Debye fitting[33].

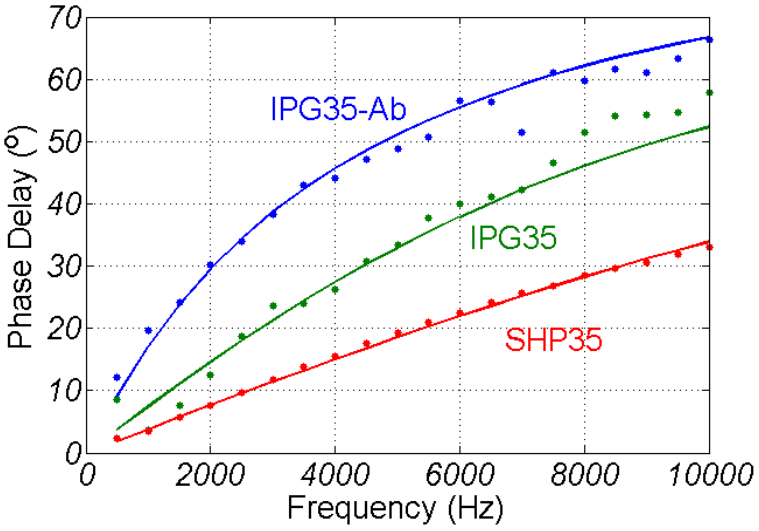

Figure 3-2 Experimental plots (dots) of phase delay of mixing-frequency f_1+2 $f_2$alongscanning frequencyf_1 for three MNP samples in water solution. Debye model (solid lines) with the superposition of MNPs size distribution shown in Figure 3-1 is plotted to compare with the experimental data.

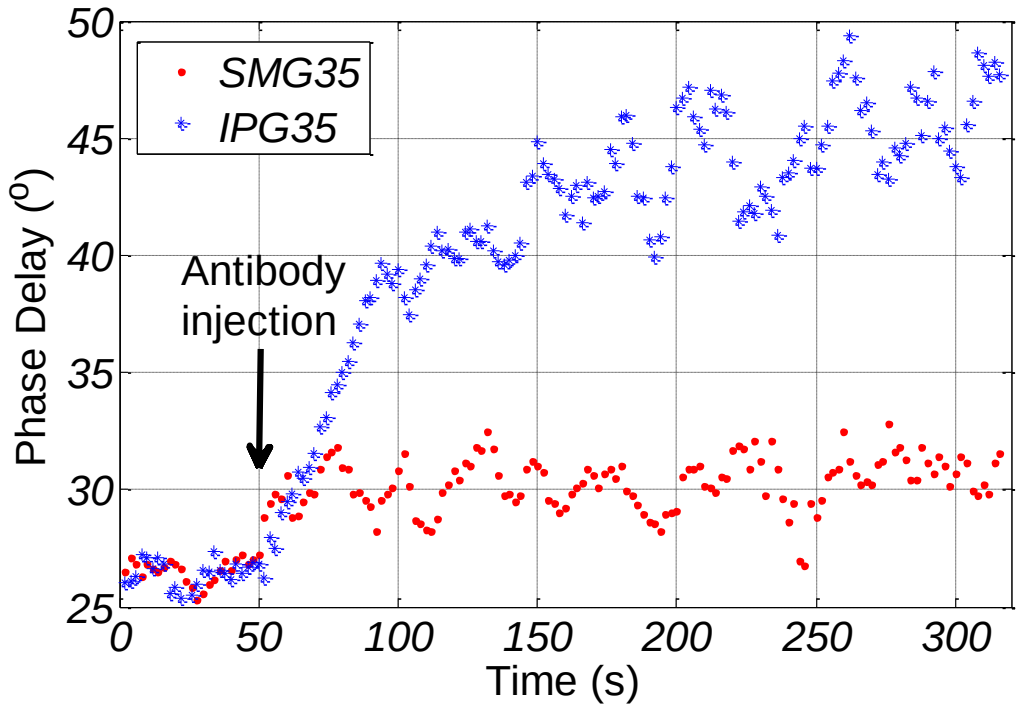

Figure 3-3 Real time measurement of phase delay of IPG35 in blue and control sample SMG35 in red, with antibody injection at the 50th second;

The binding process of the antibody to protein coated MNPs solution is detected by monitoring real time relaxation. Instead of the time-consuming whole frequency scan, the frequencyf_1 is fixed at a 4 kHz due to the high signal-to-noise ratio around this frequency region (detection coil is not sensitive in lower frequency region while MNP has low ac susceptibility in higher frequency region). 0.05 mL antibody (Goat anti-Human IgG HRP conjugated, 5 mg/mL) is dropped onto 0.1 mL IPG35 sample. The antibody sample will then diffuse slowly into IPG35 solution, and gradually bind to protein G on the surface of MNPs, until protein G binding sites on MNPs are saturated with antibody and has the same hydrodynamic size distribution as the standard IPG35-Ab sample prepared by the Ocean NanoTech. On the surface of IPG35 MNPs where protein G is not attached, hydrophilic polyethyleneglycol (PEG) is coated to block non-specific binding. Both the phase transition (Figure 3-3) and amplitude transition (not shown here) during protein G – antibody binding process are recorded. After the antibody is added to the sample at the 50th second, the detected amplitude of the mixing frequency is dropping sharply because

the sample gets diluted (away from the center of the detection coil), and also binding events will decrease the MNPs' susceptibility $|\chi|$ $|\chi|$as shown in Eq. (4). The amplitude of susceptibility has been used to determine particle clustering and binding[35], but it is heavily affected by the spatial distribution and concentration of the MNPs. In contrast, the phase information records the binding process reliably. As shown in Figure 3-3, the antibody solution is added into IPG35 solution at 50th second. As antibodies diffuse into IPG35 solution and bind with MNPs, the phase delay of magnetization then begins to increase, and gradually reaches a plateau which is very close to that of the standard IPG35-Ab. The control experiment is conducted by dropping 0.05 mL antibodies into 0.1 mL SMG35 (SHP35 conjugated with around 10 nm PEG layer, 1 mg/mL). The phase delay measurement shows very little increase because PEG out layer of SMG35 MNPs effectively blocks the non-specific binding between MNPs and antibodies. The slight increase is possibly because of the higher viscosity from the abundant antibodies in the solution. The experimental and control results show that our system accurately detects the binding between the protein G and antibodies in real time. There are two sources for the relatively large noise for the real time phase delay measurement. Since the MNPs concentration decreases due to dilution, the output signal amplitude decreases and the phase delay measurement suffers from smaller signal-to-noise ratio. Another noise source is from the digitization device when measuring the small mixing frequency signals buried in the large carrier frequency signals. Dynamic carrier tone cancellation scheme[36] can be implemented to reduce the noise and this is in progress.

3.2 MNP coloring

3.2.1 MNP responses along frequency

Phase and amplitude of various MNPs are measured over frequencies. The MNPs samples include iron oxide nanoparticles with size 15nm, 20nm, 25nm, 30nm, 35nm. All these iron oxide MNPs are from Ocean NanoTech. Another two beads MACS (50nm) and

Adembeads(100 nm) are also measured. Magnetic nanoparticles are embedded in the beads, so only Néel relaxation will occur when an ac magnetic field is applied.

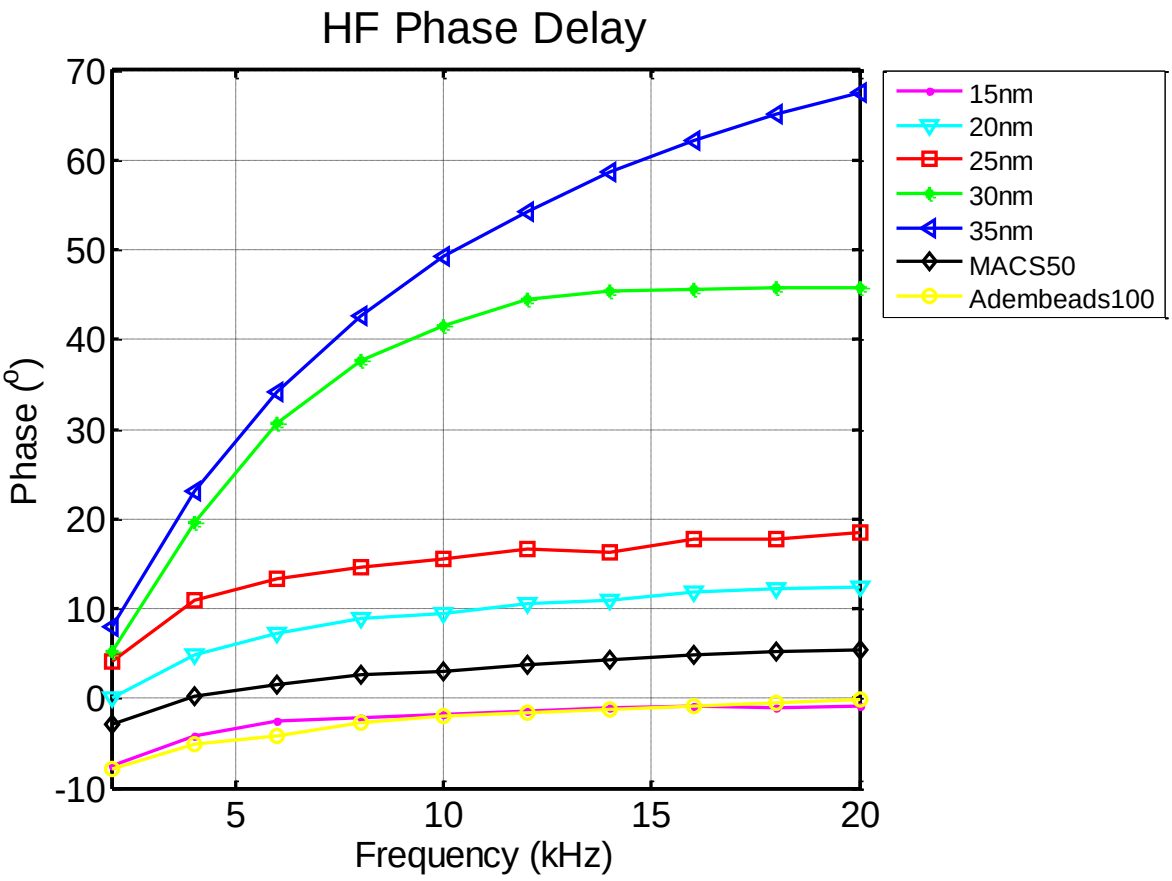

Figure 3-4 Phase delay over high frequencies for various MNPs.

Figure 3-4 shows the phase delay over frequency for various MNPs. As expected, the phase delay increases as frequency increases, and the bigger MNPs have bigger phase delay. The negative phase of mixing frequencies is from the complexity of amplitude and phase modulation of magnetization. Although it is hard to directly interpret the size distribution from the phase measurement, each MNPs has its own signature of phase, and thus can identified from other MNPs.

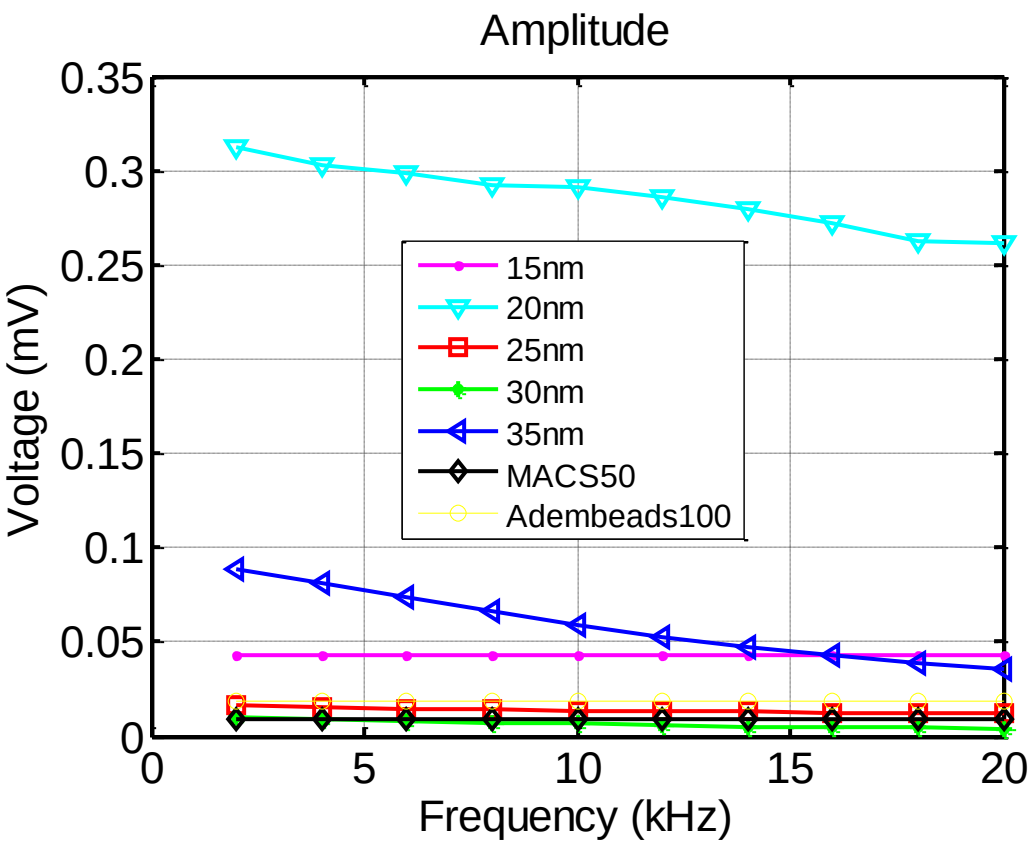

Figure 3-5 Amplitude over high frequencies for various MNPs.

Figure 3-5 shows the amplitude of MNP magnetization over frequencies. The amplitude decreases as frequency increases. The different value of magnetization amplitude between each MNP is mainly due to the amount of sample measured. In order to compare the samples, all the measured amplitudes are normalized to the first point at 2 kHz, as shown in Figure 3-6. 15nm Iron Oxide MNPs and Adembeads have so small size that their magnetization amplitudes are constant below 20 kHz frequency range. As the size increases, the magnetization amplitudes drop more rapidly over frequency.This indicates that for bigger MNPs, it cannot follow high frequency field, and is not suitable for high-sensitivity detection using high frequency field.

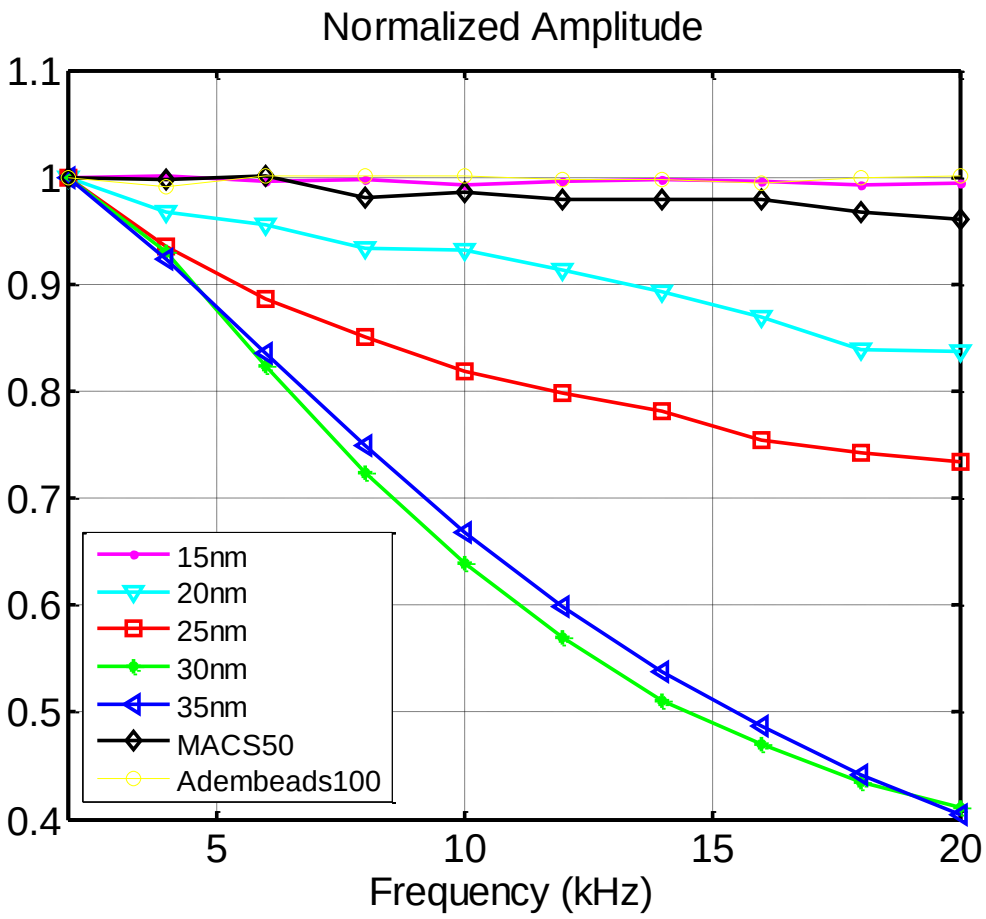

Figure 3-6 Normalized amplitude over high frequencies for various MNPs.

Figure 3-7 shows the low frequency response of several MNPs. In this measurement, the low frequency field in the mixing frequency method is scanned up to 200Hz. This measurement shows that the magnetization amplitude is almost constant in the low frequency range.

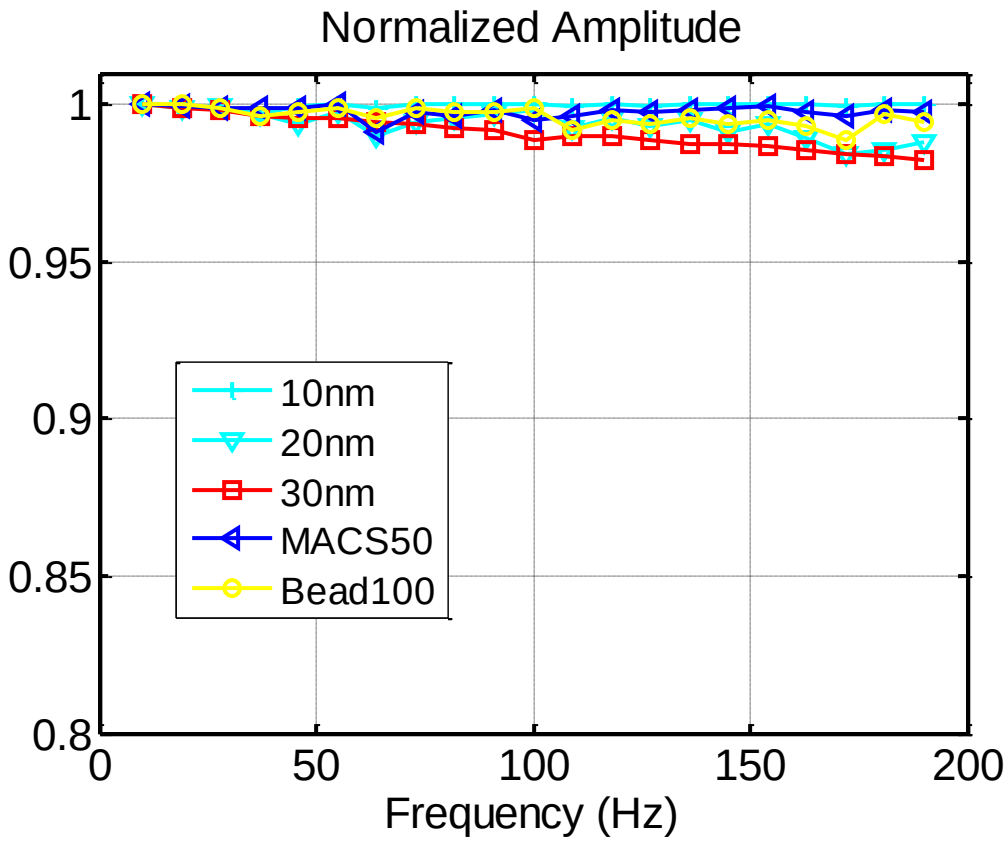

Figure 3-7 Normalized amplitude over low frequencies for various MNPs.

3.2.2 MNP coloring simulation

Apply two ac magnetic fields to 3 MNPs with different Langevin M-H curve:0.3 + 0.4*sin(250Hz*2πt)+0.02*sin(50KHz*2πt).The Fundamental higher harmonics and mixing term frequency amplitude (250 Hz, 500 Hz, 50 kHz, 50.25 kHz, 50.5 kHz…) are used for colorization. 3 MNP samples with different magnetization curves shown in Figure 3-8 are used for test. As shown on the Figure 3-9, 3 MNPs have different time-domain response, and the patterns of ratio of mixing terms around 10 kHz in frequency domain in

Figure 3-10 are different. Three peaks can provide three equations to solve the three unknown variables (amount of MNPs).Least Square method for estimation can be used if more equations are available. A generated random noise is added in the signal. Since the solution must be nonnegative, Matlab function 'lsqnonneg' is used to estimate the amount of each MNPs.

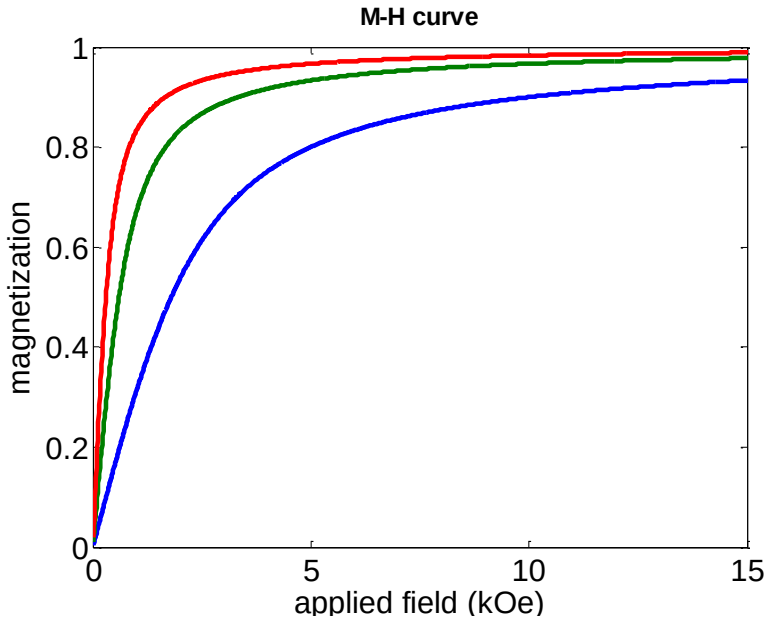

Figure 3-8 MH curve for three MNP samples

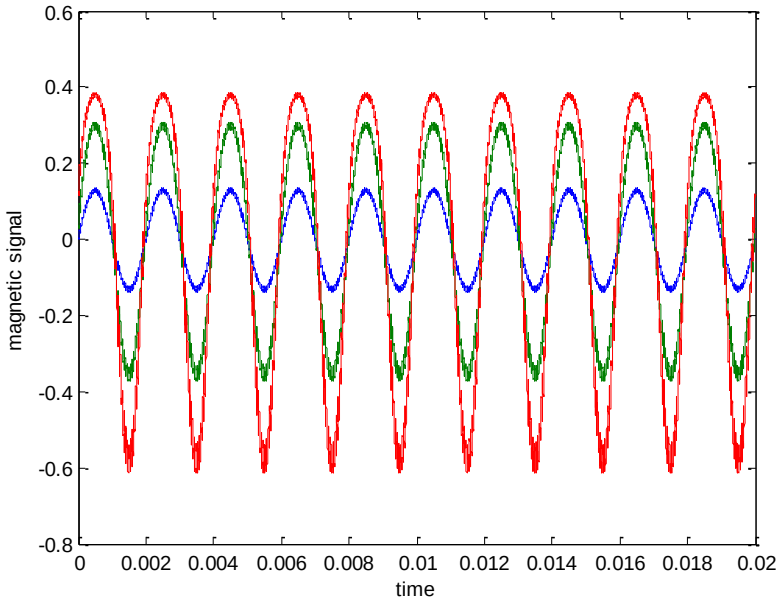

Figure 3-9 Mixing frequency response in time domain

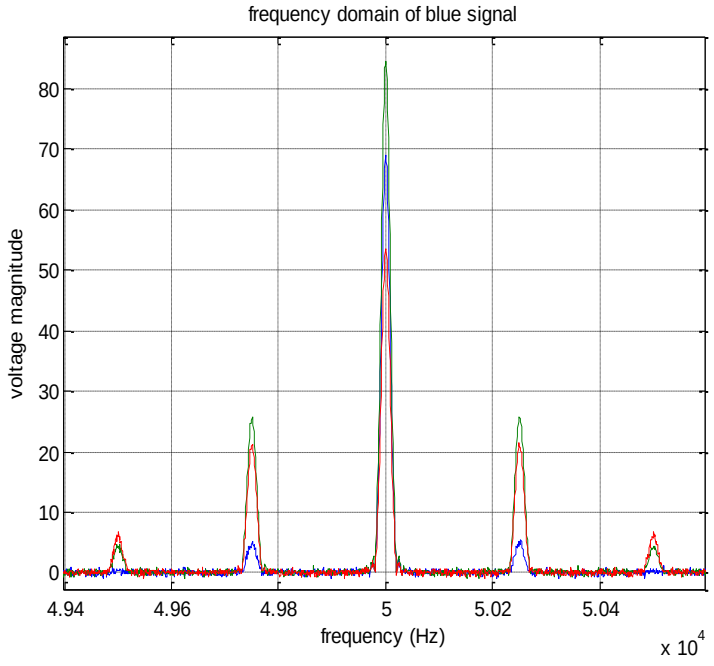

Figure 3-10 Mixing frequency response in frequency domain

The output signals per unit particles have the following frequency components,

	49/51 KHz	49.5/50.5 KHz	99.5/100.5 KHz
Blue	1.173	3.708	0.1173
Green	14.49	65.51	1.448
Red	9.533	227.5	2.911

Now we mix three MNPs together with the following ratio,

	Blue	Green	Red
Amount (unit)	2.4	5.5	4.3

The mixed output signal has the following frequency component,

	49/51 KHz	49.5/50.5 KHz	99.5/100.5 KHz
mixed	123.5	1347	20.76

Solve the equations below,

$X*1.173 + y* 14.49 + z * 9.533 = 123.5$

$X*3.708 + y* 65.51 + z * 227.5 = 1347$

$X*0.1173 + y* 1.448 + z * 2.911 = 20.76$

The calculated amount of particles of blue, green and red MNPs are,

	Blue	Green	Red

Calculated Amount (unit)	2.52	5.49	4.299
Error percentage	5.2%	0.17%	0.03%

3.2.3 MNP coloring using amplitude of magnetization

Two kinds of MNPs are used to demonstrate the colorization using the mixing frequency method. The two samples are 15nm magnetite SOR15 and 20nm magnetite SOR20. The concentration is both 20 mg/mL Chloroform. Use 200 μg or 10 μL as 1 unit for convenience. Mix the two samples with different ratios. By using 1 unit SOR15 and 1 unit SOR20 as references, we can determine the mixing ratio of other samples as shown below.

SOR15 and SOR20 mixed solution. (1 unit = 200 μg MNP sample)						
	Mix 1	Mix 2	Mix 3	Mix 4	Mix 5	Mix 6
SOR15: *(sample)*	0.5	1	1.5	0.7	2	0
Test 1 *(measured)*	0.56	1.28	1.86	0.88	1.99	0.01
Test 2 *(measured)*	0.52	1.20	1.74	0.85	2.04	0.01
SOR20: *(sample)*	1.5	1	0.5	1.3	0	2
Test 1 *(measured)*	1.68	0.87	0.28	1.2	0.01	2.01
Test 2 *(measured)*	1.67	1.02	0.57	1.47	0.04	2.05

The errors shown in the results of experiment may be from:

1. Measurement Error:

   Measurement is not stable suffering from fluctuation noise.

2. Pipette Error:

   Pipette is not accuracy enough to deliver μL sample. Also, solvent evaporation will affect the results.

3. MNPs Dispersion Error:

   When mixing two different solutions, the MNPs may not mix and disperse very well. Ultrasonic shaking must be done before the test.

Multiple measurements show Pipette Error is the main contributing factor. Two same prepared samples will have different signals, and this difference is much larger than the measurement fluctuation from the system. Even though there are various uncertainties affecting the measurement reliability, the trending still shows a good estimation. The figures below show the estimation errors distribution. The red color shows less errors, or higher possibility, and the blue color shows more errors, or less possibility.

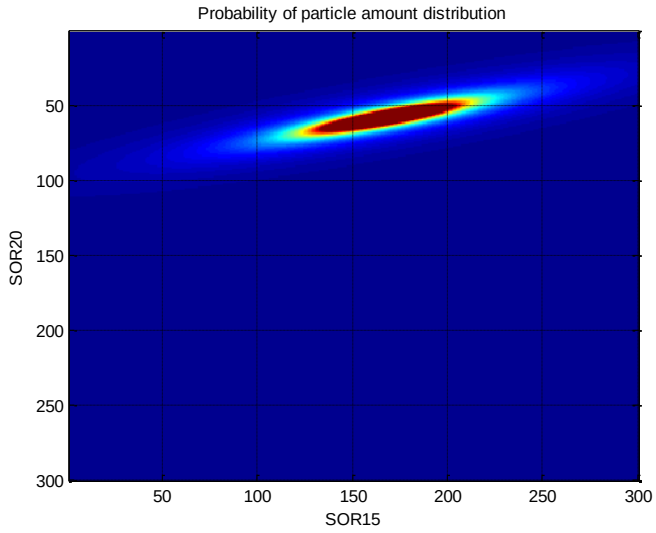

Figure 3-11 Calculated probability map of 150 μg SOR15 and 50μg SOR15.

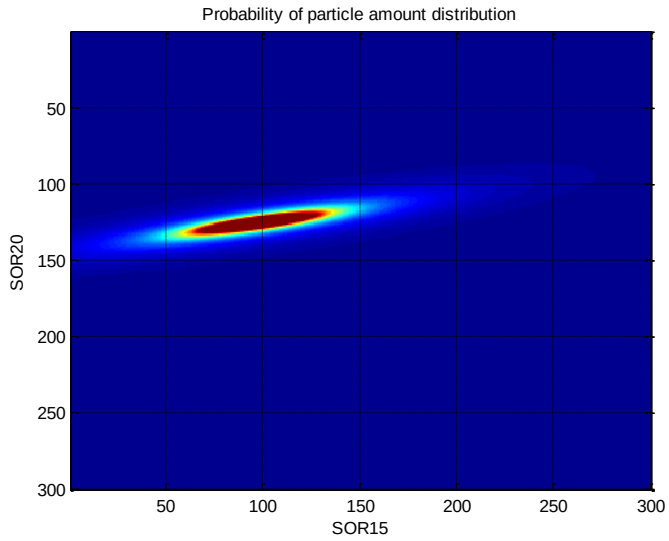

Figure 3-12 Calculated probability map of 100 µg SOR15 and 100µg SOR15.

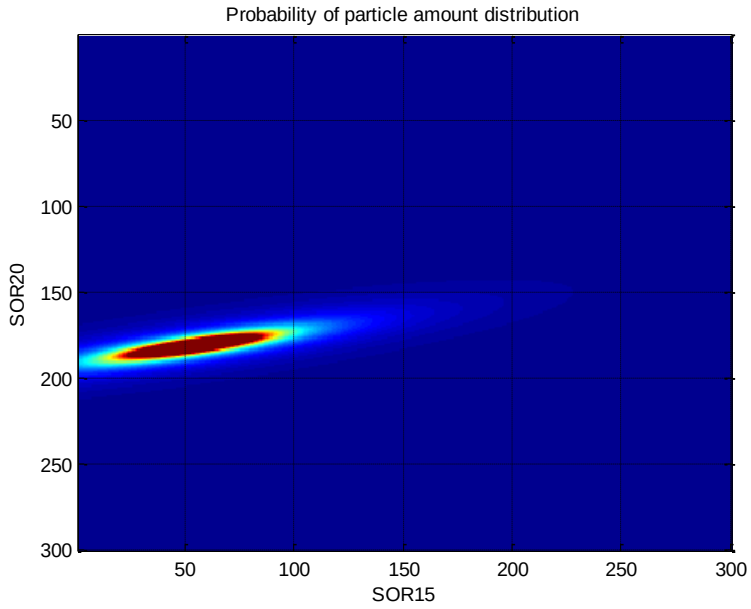

Figure 3-13 Calculated probability map of 50 µg SOR15 and 150µg SOR15.

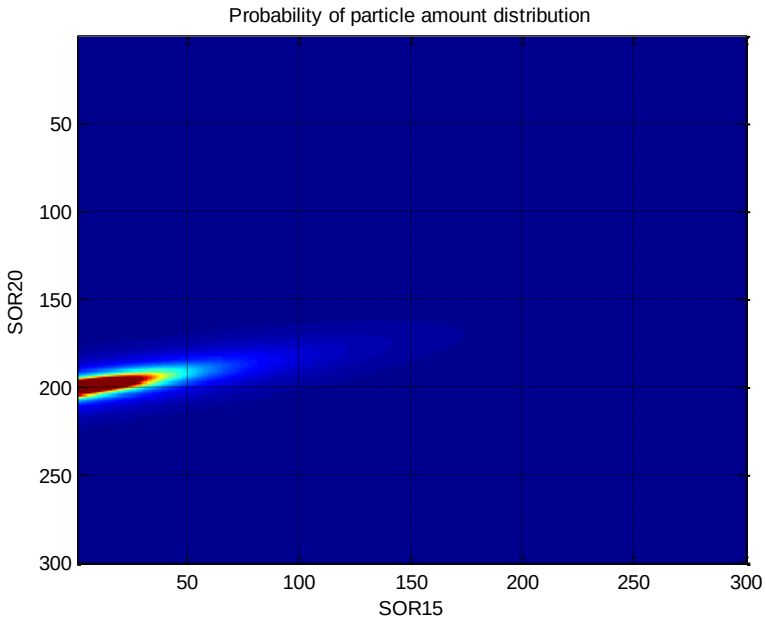

Figure 3-14 Calculated probability map of 200 μg SOR15.

	Samp1	**Samp3**	**Samp4**	**Samp5**	**Samp6**	**Samp2**
Mixing ratio in 5 uL solution	1 A	0.8 A 0.2 B	0.6 A 0.4 B	0.4 A 0.6 B	0.2 A 0.8 B	1 B
f1 (1e-3)	19.8098	15.0095	13.2195	7.9040	5.3095	3.9365
f2 (1e-3)	11.1730	7.6945	6.4935	4.8825	3.6875	2.0215
f1 +2f2 (1e-3)	2.7942	1.7645	1.2471	0.7947	0.4184	0.0462
f1 +4f2 (1e-3)	0.7668	0.4813	0.3317	0.2064	0.1002	0.0041

Table 3-1 Amplitude of linear and mixing frequencies of each sample

Another experiment uses sample A (20nm magnetite from medical school of UMN) and sample B (50nm magnetite from Ocean NanoTech). 1 unit is 85μg. All the measurement samples are mixed in 5 μL cyclohexane solution. Below are the measurement results.

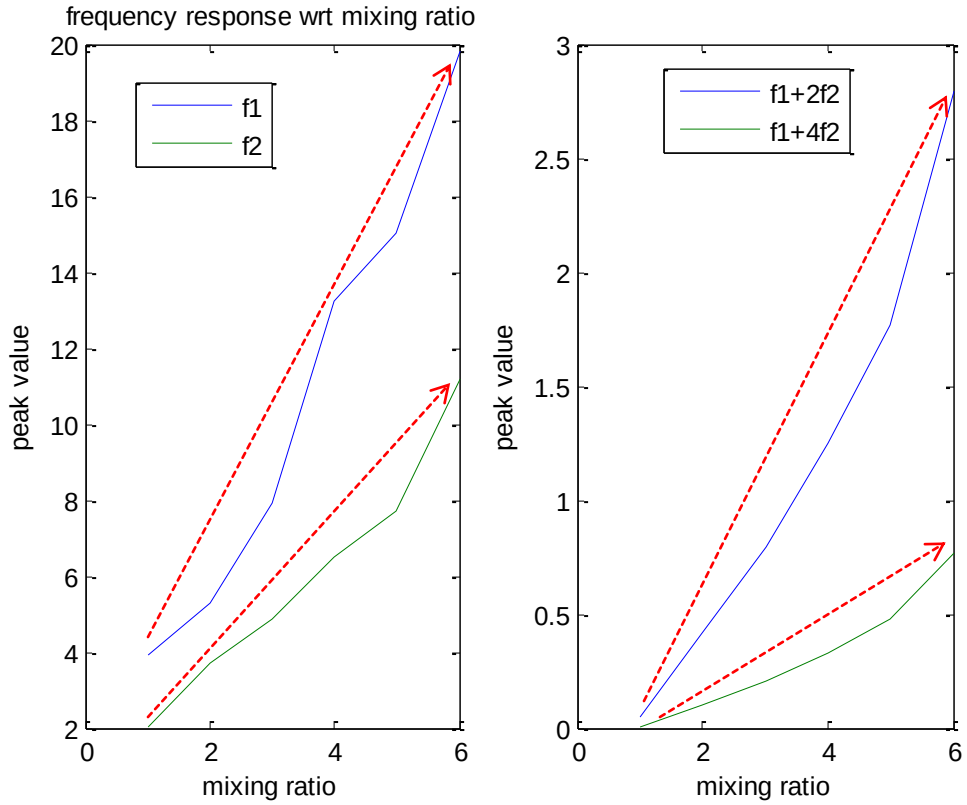

The above measurement results show that the mixing of two MNPs have effects on the overall measurements. The signal value has a nonlinear relation with the mixing ratio.

3.2.4 MNP coloring using amplitude and phase of magnetization

Two kinds of MNPs with 20nm and 35nm Iron Oxide core are used for this experiment. They are divided into 5 samples with different ratio as shown below.

Unit: μL	Sample 1	Sample 2	Sample 3	Sample 4	Sample 5
20 nm MNP	4	3	2	1	0
35 nm MNP	0	1	2	3	4

Table 3-2 Composition of 20 nm and 35 nm MNPs in each sample

The measurement results show the amplitude Figure 3-16 and phase delay Figure 3-17 of each sample. Clearly there is trend for the 5 samples in both phase delay and amplitude. The in-phase and out-of-phase amplitude also can be calculated and plotted in Figure 3-18. With all these information, the amount of 20 nm MNP and 30 nm MNP can be estimated by least mean square method with positive solution ('lsqnonneg' in Matlab). Table 3-3 lists the colorization errors from the estimations using only the amplitude and using amplitude/phase over the whole frequency span. Although the error may be from sample preparation process, such as pipette calibration error, the overall results show that by using amplitude and phase, the error is comparably smaller. Figure 3-19 shows the error distribution along the frequencies. When frequency is low, there are not many differences between 'Amp+Phase' and 'Amp'. As the frequency increases, the 'Amp' estimation clearly suffers from the lack for information of the phase. So phase must be considered for colorization in the high frequency region.

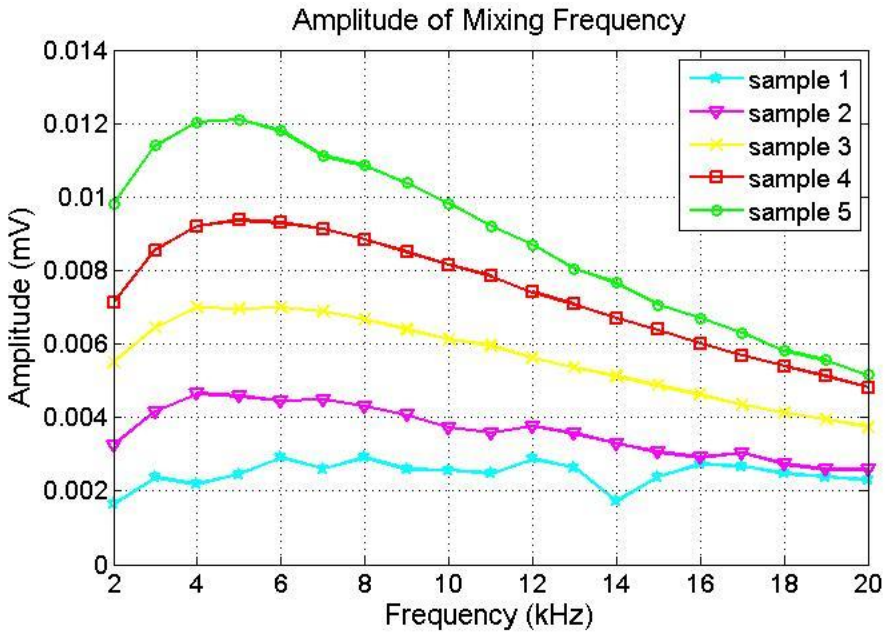

Figure 3-16 Amplitude of Mixing Frequency along frequency for 5 samples

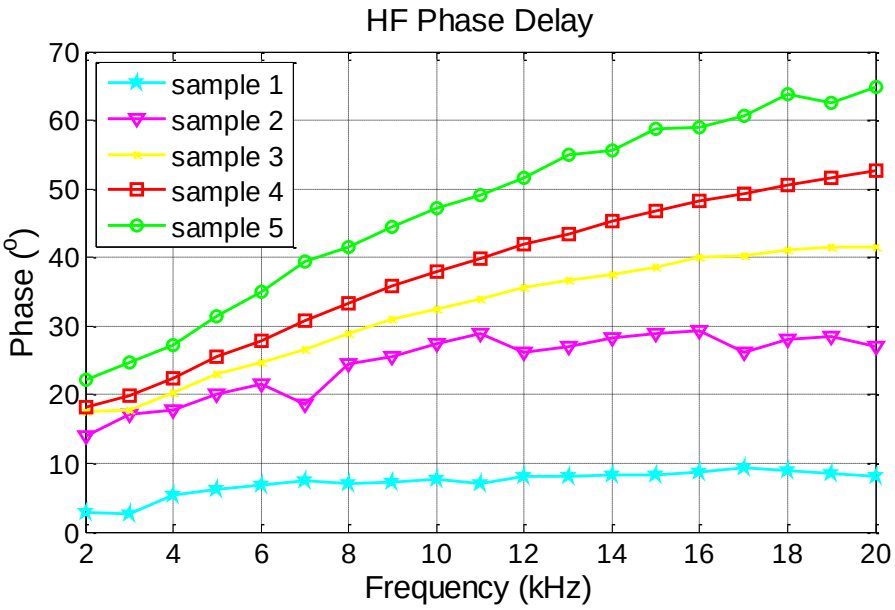

Figure 3-17 Phase delay of high frequency along frequency for 5 samples

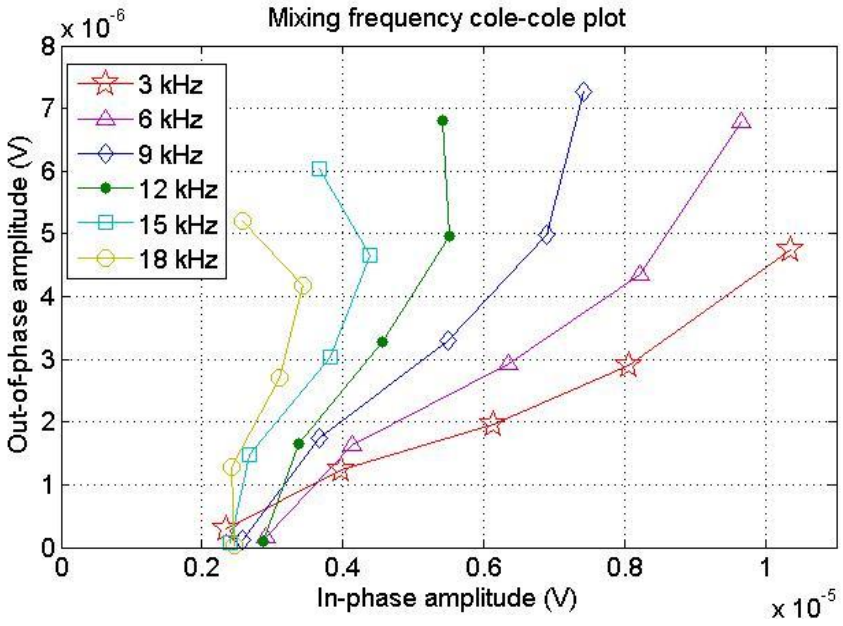

Figure 3-18 Cole-cole plot of complex magnetization amplitude of the 5 samples at different frequencies.

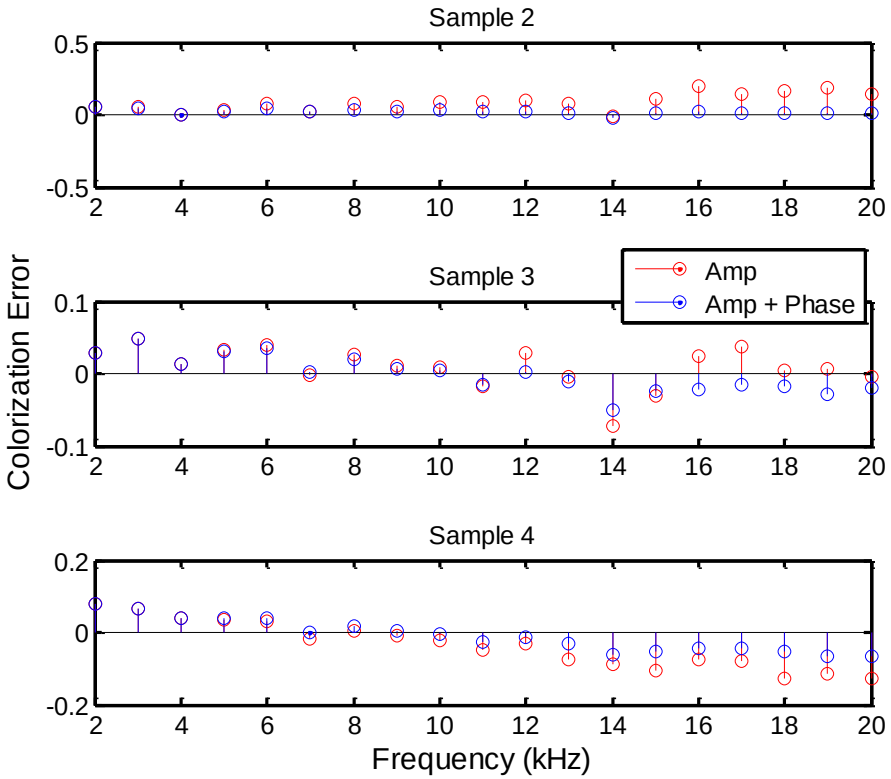

Figure 3-19 Estimation error based on amplitude and phase at each frequency

Error (%)	Sample 2	Sample 3	Sample 4
Estimation error using amplitude Only	5.95	1.54	0.07
Estimation error using Amplitude and Phase	2.28	0.78	0.74

Table 3-3 Estimation error based on amplitude and phase over the whole frequency span

3.2.5 MNP coloring by adding a static field

If the Taylor expansion of Langevin equation is not around zero, then $f_H \pm f_L$ will be generated. A current source is used to generate a static field, and 5 higher harmonics are recorded along the static field. Two samples are used for comparison. One is FeCoAu grown by the phase-target method in our group, and the other is FeO30 grown by chemical method in medical school. Figure 3-20shows the MH loop of these two MNPs. Figure 3-21 and Figure 3-22 shows the trend of these 5 harmonics along static field for FeCoAu and FeO30. It is clear that both the ratio and trend of these 5 harmonics are very different between the two MNPs. $f_H \pm f_L$ will increase and $f_H \pm 2f_L$ will decrease along static field. Above certain static field, $f_H \pm f_L$ will surpass $f_H \pm 2f_L$ and will be optimum for detection.

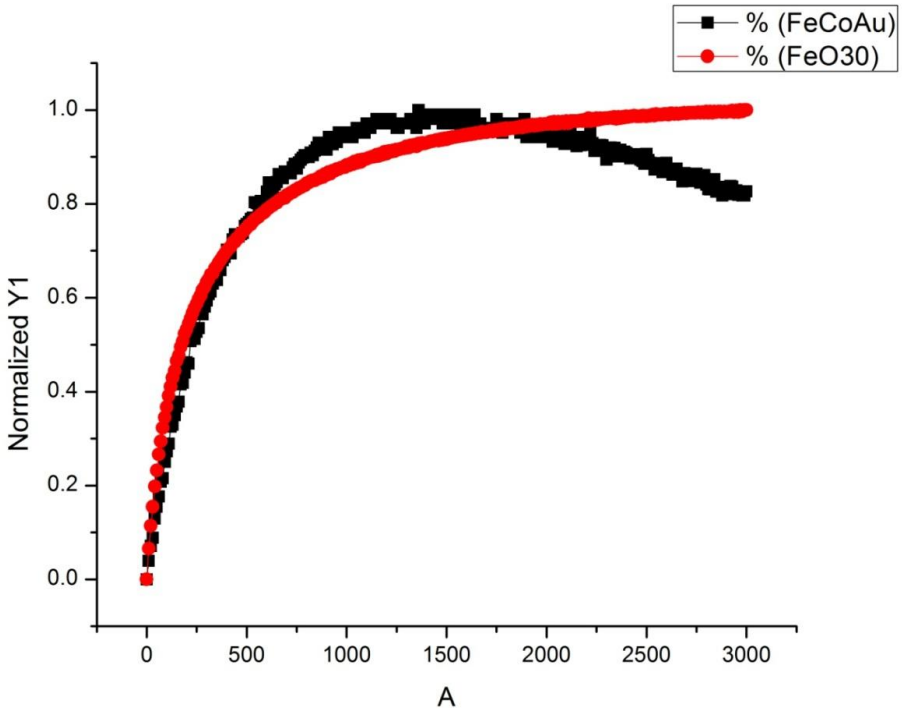

Figure 3-20 MH loop of FeCoAu and FeO30

At zero static field, the two MNPs shows different pattern of amplitude in

frequency domain. From Figure 3-20, FeO30 reaches saturation at smaller field, so it is more 'soft' than FeCoAu. The frequency measurement also shows that the mixing terms of FeO30 are bigger due to bigger nonlinearity. For coloring application, FeO30 and FeCoAu not only have different response at zero static field, but also has dramatic difference when an external static field is applied.

Unit: V	f_H	f_L	f_H+2f_L	f_H+4f_L	$2f_H+f_L$	$2f_H+3f_L$
FeCoAu	0.0013000000	0.0000373720	0.0000599620	0.0000102420	0.0000348950	0.0000136180
Normalized	1.0000000000	0.0287476923	0.0461246154	0.0078784615	0.0268423077	0.0104753846
FeO 30nm	0.0033000000	0.0000858460	0.0002449600	0.0000365300	0.0001299400	0.0000451200
Normalized	1.0000000000	0.0260139394	0.0742303030	0.0110696970	0.0393757576	0.0136727273

Table 3-4 Amplitude of linear and mixing frequencies of each sample

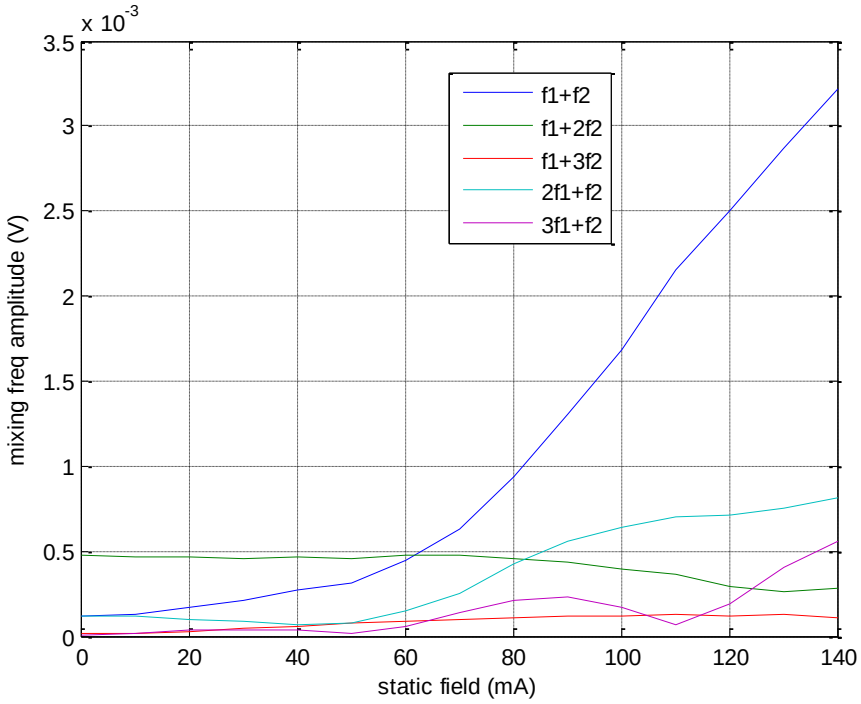

Figure 3-21 Mixing frequencies of FeCoAu along static field.

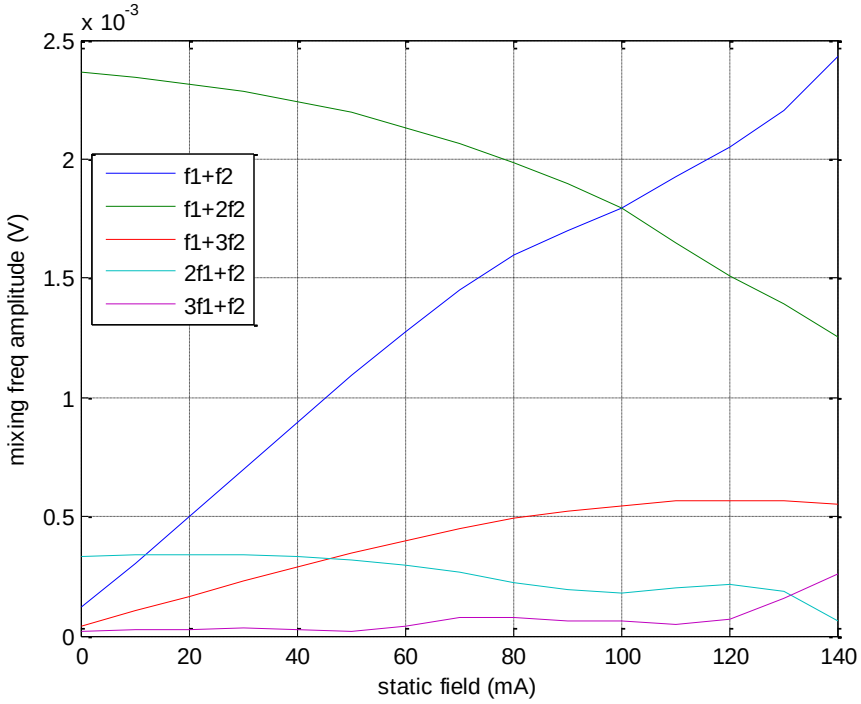

Figure 3-22 Mixing frequencies of FeO30 along static field.

3.3 Bulk material measurement

Bulk ferromaterial can also be measured by mixing frequency method. The magnetization comes from the domain wall movement and domain nucleation. The magnetization curve is usually very sharp, thus nonlinearity is strong. Below are the high frequency and low frequency measurement of a FeCo bulk sample. The mixing frequency model for bulk will be complex, and the meaning of the results, Figure 3-23 and Figure 3-24 will not be discussed here.

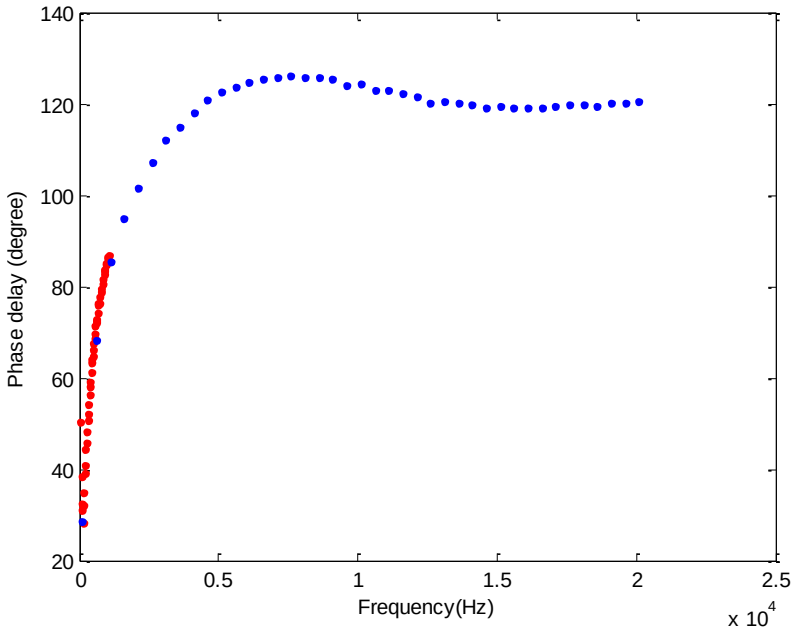

Figure 3-23 Phase delay over the range of high frequency.

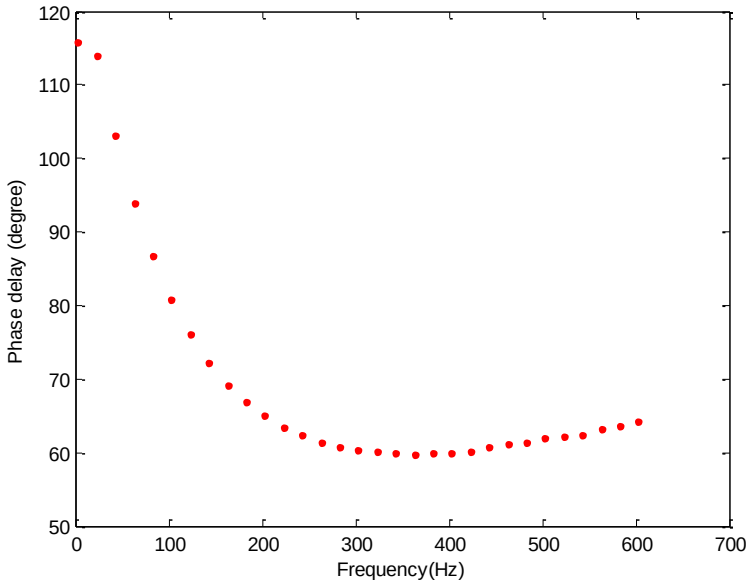

Figure 3-24 Phase delay over the range of low frequency.

3.4 Thin film measurement

Thin film can also be measured by mixing frequency method. $Fe_{16}N_2$, as the most magnetic material, is grown by facing target sputtering method on Fe thin film underlayer and GaAs substrate. The magnetic field is applied parallel to the film plane of the sample FN09b. The magnetization curve measured by VSM shows that Fe thin film will saturate first and $Fe_{16}N_2$ will saturate gradually. So in our applied field range, the main contribution to the signal is from Fe.

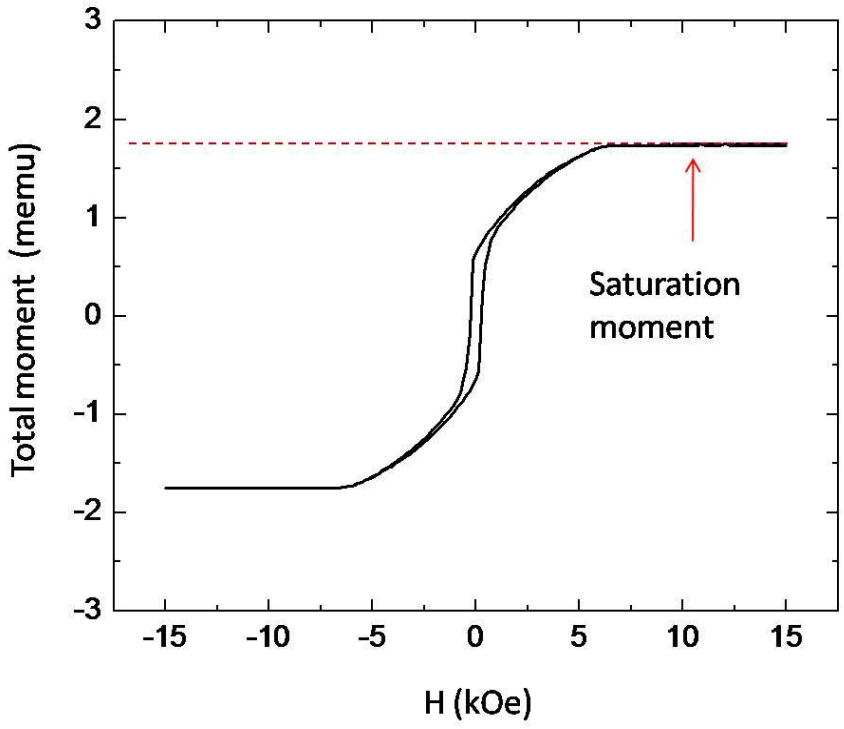

Figure 3-25 In-plane MH loop of $Fe_{16}N_2$/Fe thin film.

A 10 Hz 100 Oe field and a 10 kHz 10 Oe field are applied to the sample. The low frequency field can easily saturate the Fe film, so only around zero field the magnetization reversal can be observed. Around the static field, the 10 kHz field can facilitate the magnetization reversal to further states periodically. The jumps to the new states in Figure 3-27 of magnetization generate voltage peaks in Figure 3-26.

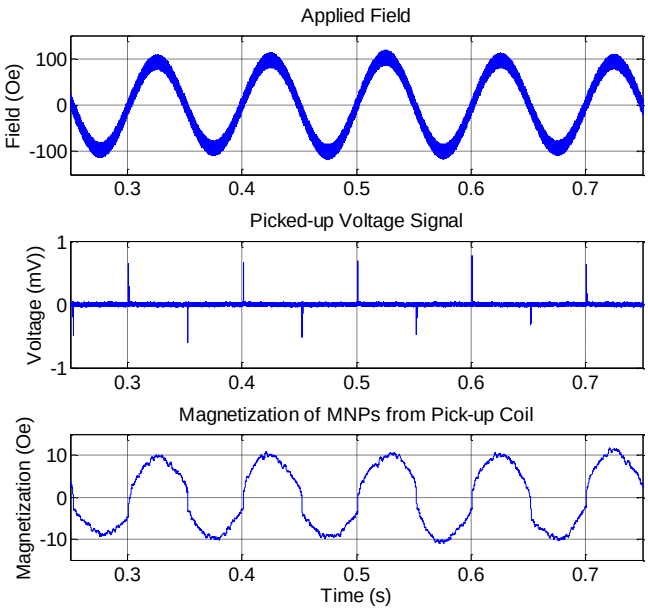

Figure 3-26 Top figure is the applied field. Middle figure shows the picked-up voltage from the coil. Bottom figure shows the magnetization calculated from the voltage signal.

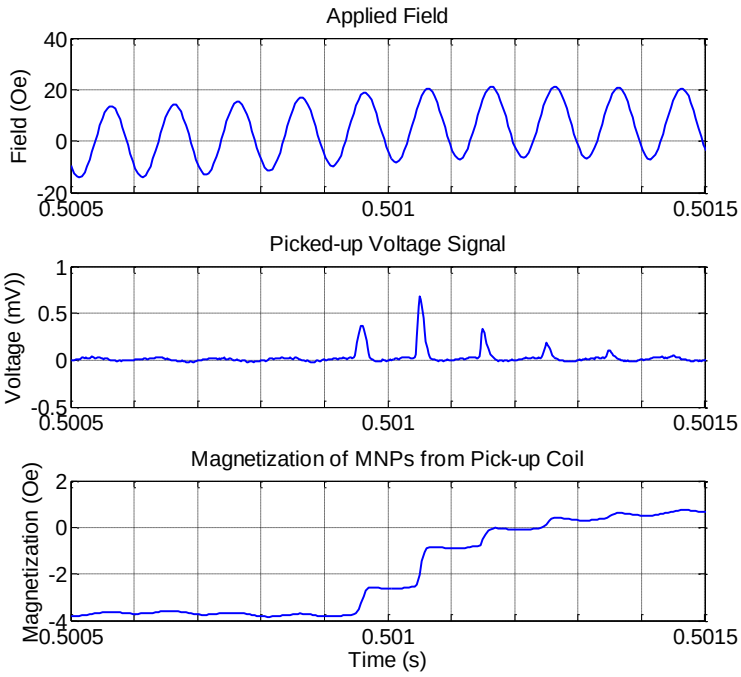

Figure 3-27 Zoomed-in plots of Figure 3-26

3.5 Magnetosome measurement

Magnetosomes are magnetite nanocrystals surrounded by lipid bilayer membrane in magnetotactic bacteria. Compared with synthetic magnetites, magnetosome has better crystallographic performance, narrower crystal size distribution, and better biocompatibility. By gene manipulation, it can be mass produced and well controlled. Magnetosome can be isolated from cells by ultracentrifugation and magnetic seperation. In solution, magnetosome usually forms closed loop or chain structure, and exhibits hysteresis loop.

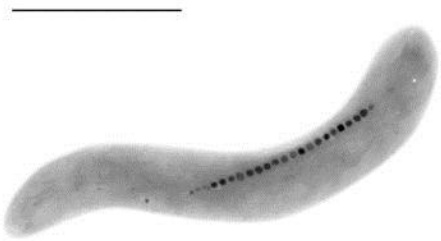

Figure 3-28 MS-1 cell with magnetosomes (bar=1μm).

It is observed that phase delay (relaxation time) of magnetosomes increases after ac field is applied, and converge after certain time. This is an indication that magnetosome agglomerate under ac field. The TEM image Figure 3-31 shows the average size of magnetite core is 45 nm. However, the size estimation Figure 3-32 from the phase delay shows the hydrodynamic size is around 500nm, which is also an indication of the agglomeration in the solution.

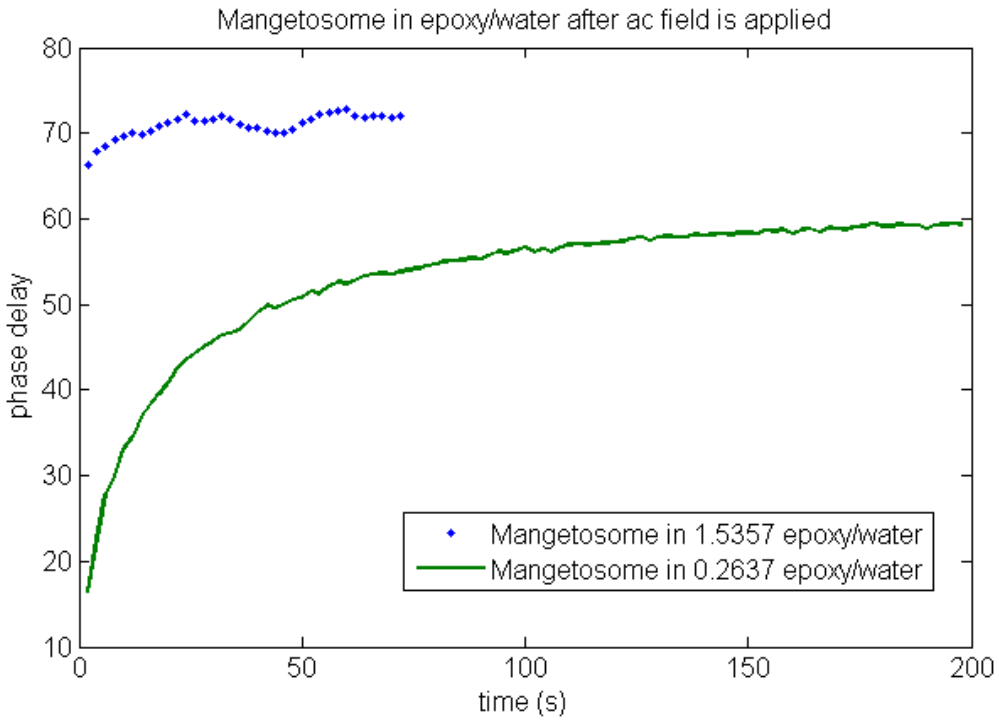

Figure 3-29 Phase delay along time of magnetosomes in two solution with different viscosity.

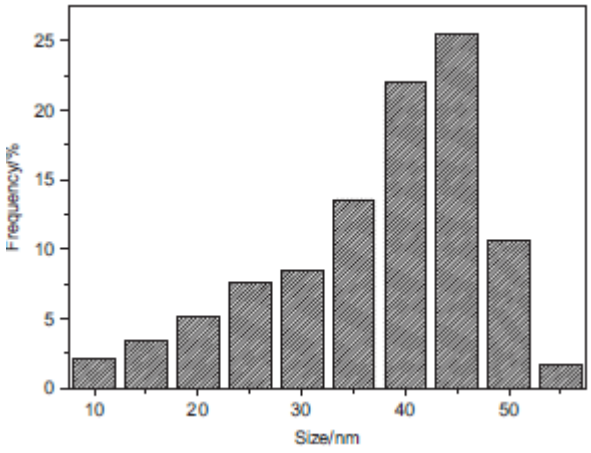

Figure 3-30 Size distribution of single magnetosome crystals

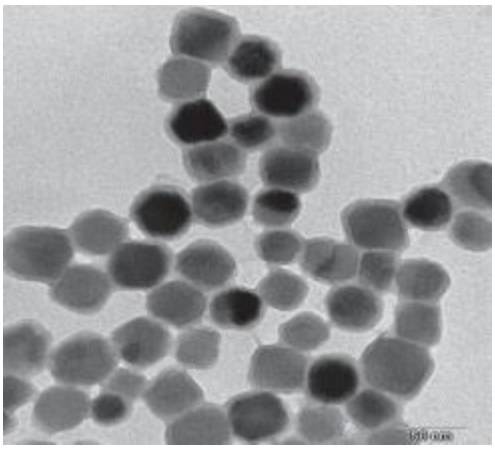

Figure 3-31 TEM of clusters of magnetisomes.

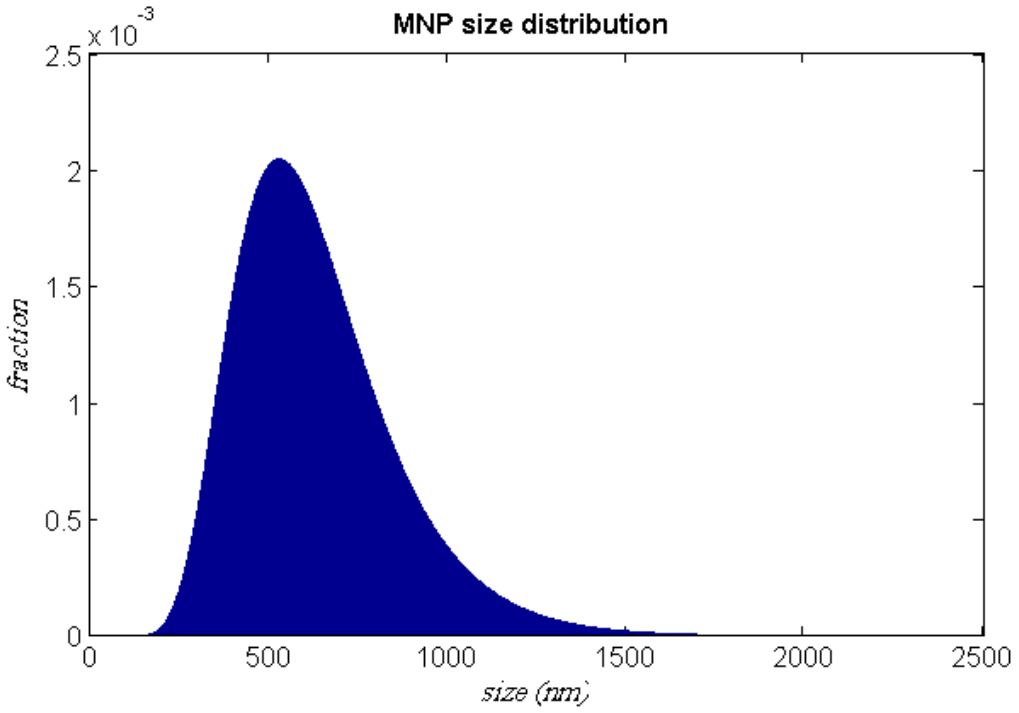

Figure 3-32 Estimated hydrodynamic size distribution of magnetosome clusters.

3.6 Viscosity measurement

Magnetosomes have been tested in three solutions with different epoxy to water ratio. The higher ratio creates a higher phase delay, because the viscose solution drags the rotation of the MNPs.

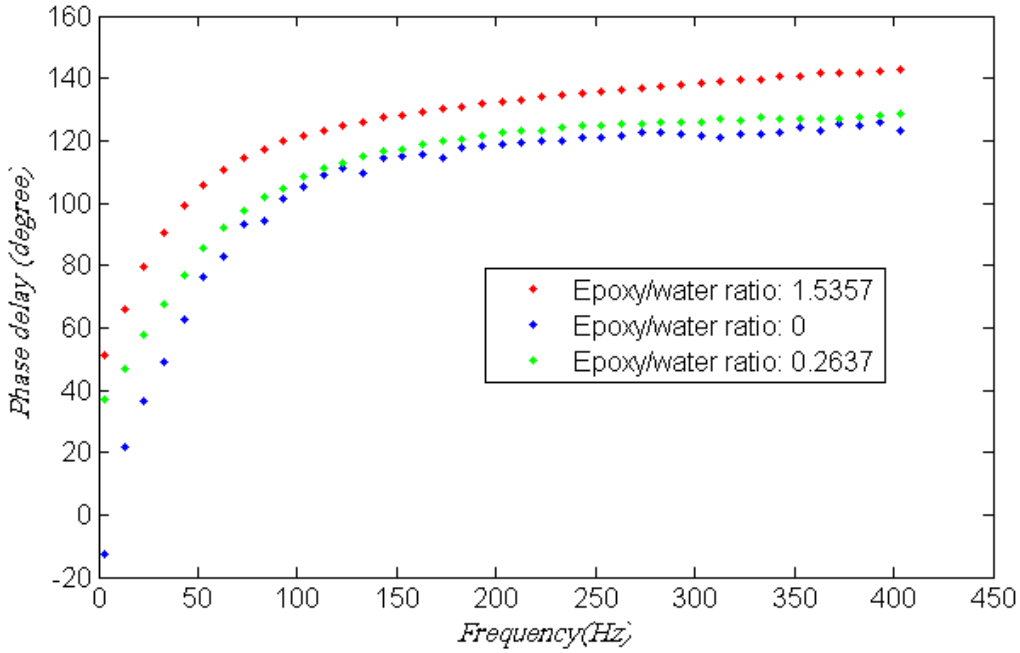

Figure 3-33Phase delay over frequencies of magnetosome in different solutions.

Also 25nm FeO MNPs are tested in chloroform and in 1:1 chloroform/epoxy solutions. The relaxation time estimation from Figure 3-34 is $\tau_{experiment-1}$ =85 μs and $\tau_{experiment-2}$ =400 μs. The 25nm MNP has 15nm coating, so the hydrodynamic diameter should be roughly 40 nm. And the viscosity constant for the solutions are η (pure epoxy) = 600 m P.s, η (pure chloroform) = 0.53 m P.s, η (1:1 epoxy/chloroform) = 17.8 m P.s. In pure chloroform, the theoretical calculated relaxation time is $\tau_{theoretical-1}$ = 12.9 μs. In 1:1 epoxy/chloroform, the theoretical calculated relaxation time is $\tau_{theoretical-2}$ = 0.43 ms.

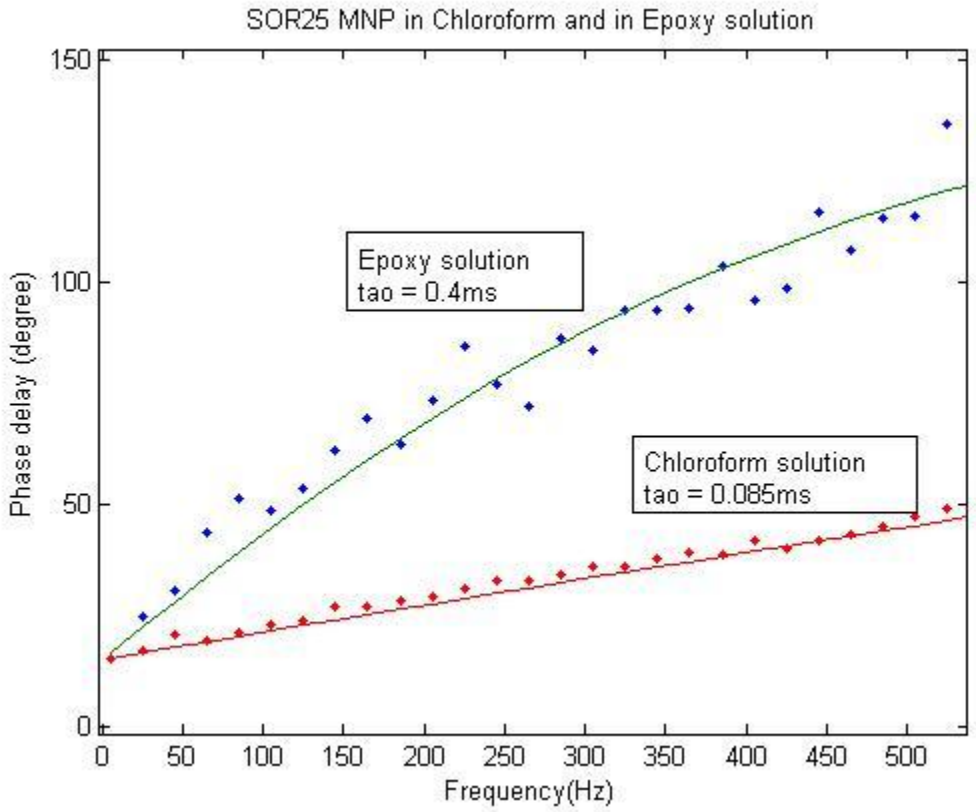

Figure 3-34 Phase delay over frequencies of 25nm MNps in two solutions.

The calculated relaxation times are 0.4ms and 0.085ms respectively.

[31] Liang Tu, et. al. 'Measurement of Brownian and Néel Relaxation of Magnetic Nanoparticles by a Mixing-Frequency Method', IEEE Transactions on Magnetics, Vol 49, No. 1, January 2013

[32] K. Enpuku, T. Tanaka, Y. Tamai, F. Dang, N. Enomoto, J. Hojo, H. Kanzaki, and N. Usuki, Jpn. J. Appl. Phys. **47**, 7859 (2008)

[33]C.M. Oireachtaigh, P.C. Fannin, J. Magn.Magn.Mater.**320**, 871 (2008)

[34] B.K.P. Scaife, J. Phys. D: Appl. Phys. **19**, 195 (1986)

[35] C. Hong, C.C. Wu, Y.C. Chiu, S.Y. Yang, H.E. Horng, and H.C. Yang,Appl. Phys.Lett. **88**,212512 (2006)

[36] J.S. Daniels, E.P. Anderson, N. Pourmand, and T.H. Lee, IEEE, Instrumentation and Measurement Technology Conference, (2010)

Chapter 4 Measurement of GMR

1. 1 GMR Sensor

Giant Magneto Resistance (GMR) sensor is a multi-layer thin film that can be used to detection magnetic field. When MNPs are bonded to the surface of the thin film, GMR can detection the stray fields from the MNPs and output electrically readable signal.

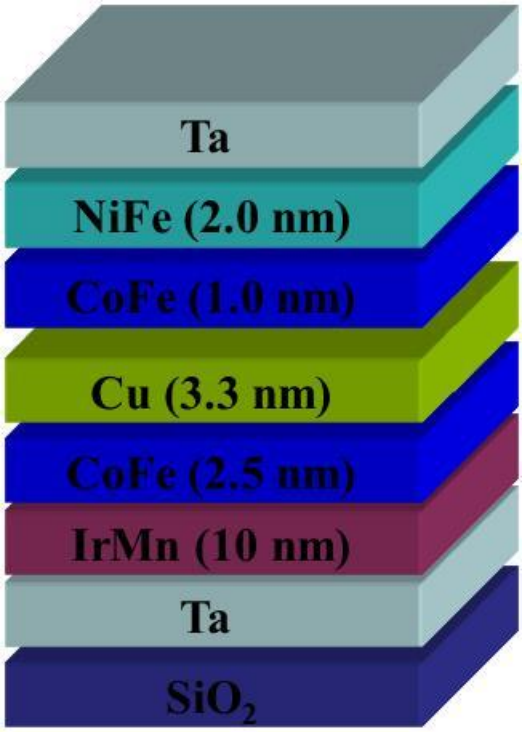

Ta: Covering and protecting layer.

Permalloy (Py): NiFe is a soft material, with small coercivity, as a **free layer**.

CoFe: Py and Cu have similar crystal structure. CoFe can separate to avoid diffusion.

Cu: Nonmagnetic conducting layer.

CoFe: Coupled with the IrMn. It has big coercivity. Function as a **fixed layer**.

IrMn: Antiferromagnetic material. Low Neel temperature. Used to pin the fixed layer.

Ta: Seed layer.

Figure 4-1Thin film structure of GMR grown by Shamrock sputtering

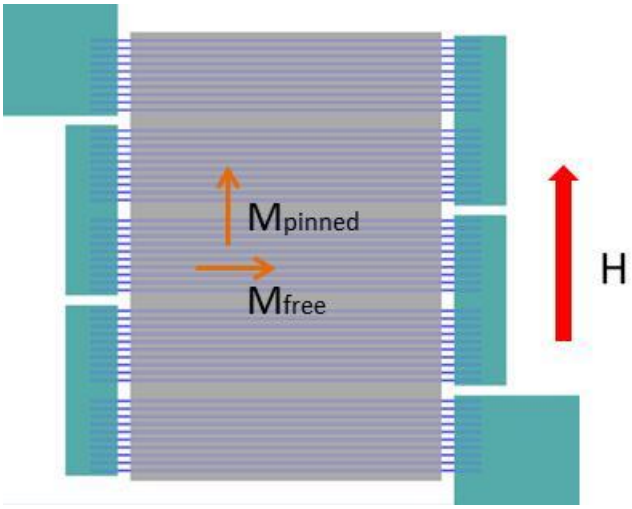

The GMR film is patterned into 50 thin strips for each sensor spot. Each strip has a width of 700 nm, and length of 100 μm. Strips are separated by 1 μm space. 10 adjacent strips are connected at the ends parallel, while 5 of these

Figure 4-2 Patterning of one GMR sensor. Shaded area is active region with thinner SiO_2 protection.

groups are connected serially. The purpose of clustering is to increase the active region of a sensor spot.

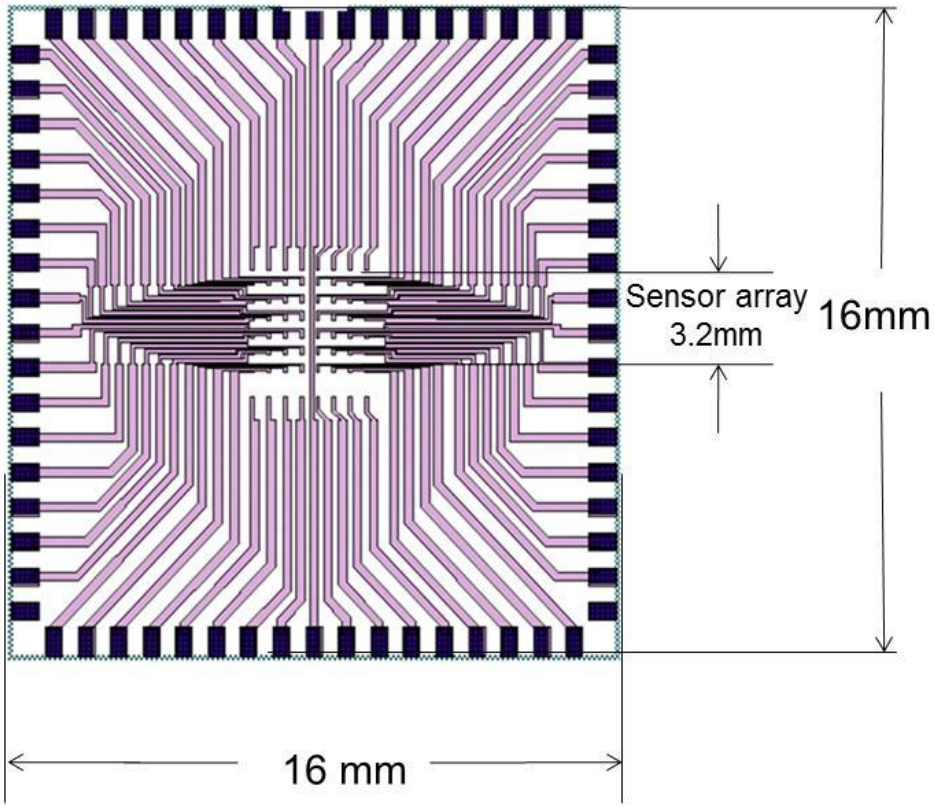

Figure 4-3 GMR sensor array (16X16) with connectors on the 4 sides

1. 2 Measurement Scheme

The resistance of GMR sensor includes static resistance R_0 and magnetic resistance ΔR. The static resistance R_0 comes from the scattering of the conduction electrons by the atom crystal, while the magnetic resistance ΔR comes from the scattering of the electron spins by the magnetization of the ferromagnetic material. Magnetic nano-particles, when in affinity of the ferromagnetic layer, can affect the magnetization of the ferromagnetic layer through its stray field, and thus can change the magnetic resistance ΔR. So instead of R_0, ΔR is an indication of the MNPs. The measurement scheme should effectively cancel the useless signal R_0, and only output the useful signal ΔR. The small signal of ΔR can be amplified many times for the digitizer to read, so the sensitivity of the system can be increased dramatically.

The Wheatstone bridge circuit has a long history of successfully being used to measure electrical resistance and small changes in that resistance.[37] It has been a standard tool for signal conditioning of strain gage and temperature coupler. However, if the variations of lead wire resistance need to be taken into consideration, Anderson loop is better due to its advantage of direct current frequency response and inherent linearity with respect to resistance change. Both circuit schemes will be introduced briefly below.

4.1.1 Anderson Loop

The working principle of Anderson loop in Figure 4-4 is very close to that of four-point probe. A current source is applied to the sensor and a reference resistor, and the detection probe measures the voltage on both the sensor and the reference resistor. The voltage drop on the contact resistance will not affect the voltage measurements on the sensor. The voltage on sensor and resistor will be compared by 3 instrumentation amplifier, and output to the digitizer. However, the lead resistance cannot be avoided convenient, and the large current can easily saturate the instrumentation amplifier, so the Anderson loop is not a good choice now.

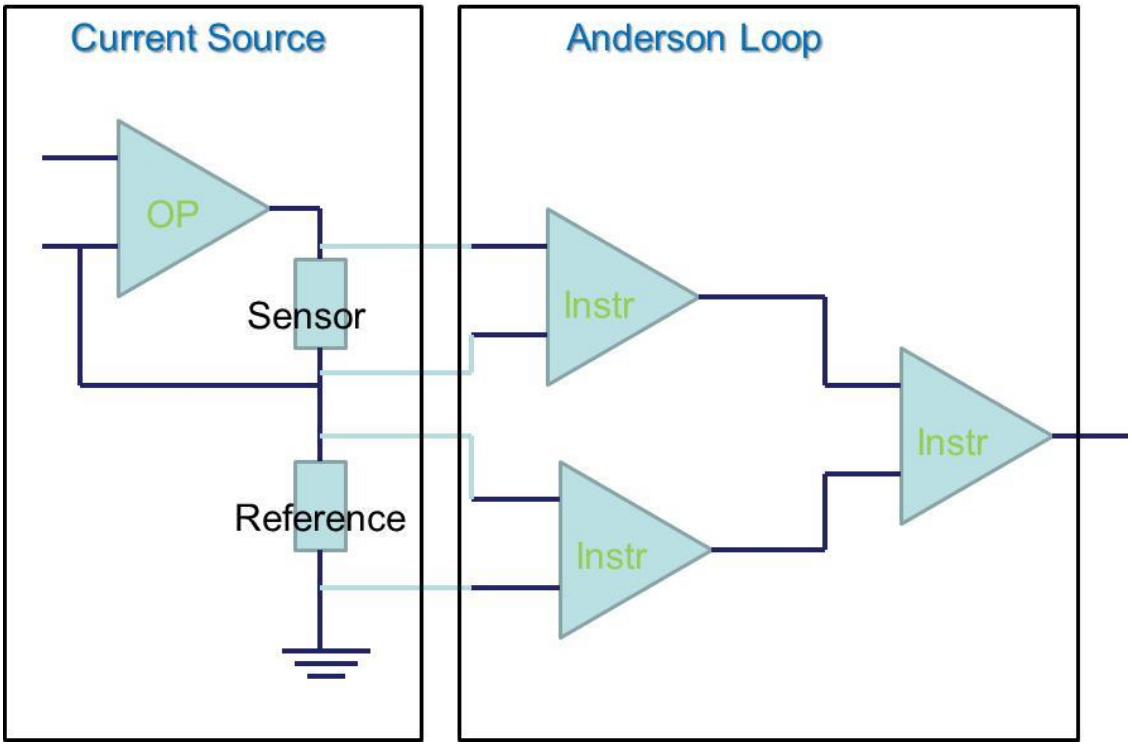

Figure 4-4 Schematic of Anderson Loop

4.1.2 Wheatstone Bridge

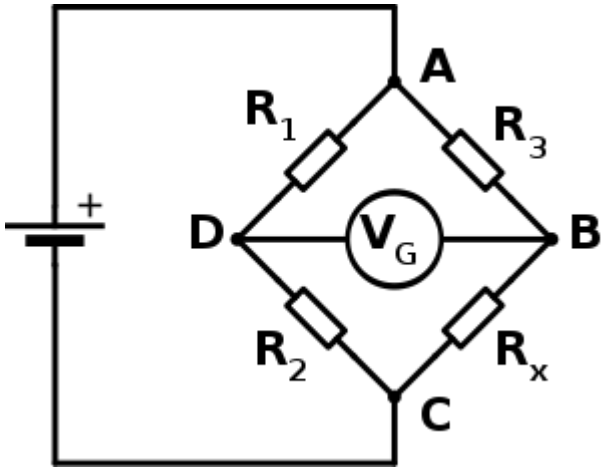

Figure 4-5 Schematic of Wheatstone brige

As shown in Figure 4-5, the balancing resistance R_1 , R_2 and R_3 of Wheatstone Bridge is tuned to be the same as the static resistance R_0 of GMR. The input voltage is V_S. And the output voltage V_G is a function of ΔR,

$V_G \approx V_S/(2R_0 + \Delta R)^* \Delta R$;

When ΔR is small compared to R_0, the output voltage V_G can be considered linearly correlated with ΔR. If the GMR is working in the linear region of the transfer curve, VG is linearly correlated with external magnetic field. Also if the circuit is well balanced, a large current can be applied without saturating the instrumentation amplifier. Generally large current can increase the SNR.

4.2 Mixing frequency measurement

The traditional DC detection is to measure the changing resistance ΔR while applying a DC current. However, the magnetic resistance ΔR has big 1/f like noise as described in the next paragraph, so the detection at DC will suffer from the low frequency

noise. By applying an AC magnetic field with frequency f_m, the detection frequency f_m can be increased to avoid low frequency noise. In order to avoid the electromagnetic interference at f_m, an AC current with frequency f_c is applied to modulate the magnetic resistance ΔR to the high frequency $f_c \pm f_m$. The relationship between the mixing terms and sensing current and excitation field is illustrated in Figure 4-7.

GMR sensor magnetization and resistance drift slowly, and this low frequency fluctuation can be described in frequency as 1/f noise. The origin of GMR 1/f noise is magnetic. Magnetic domain movement or magnetization of a single domain responds more to the lower frequency of the white thermal excitation noise, so the overall magnetic noise floor is shaped as 1/f. A typical 1/f noise floor on a linear sensor is shown in Figure 4-8.

Figure 4-9 illustrates that, in the linear region of transfer curve, even the slow drift of the resistance will not affect the ac response of the GMR. By applying a 200Hz magnetic field, the noise floor Figure 4-10 is not affected at all comparing to Figure 4-8. However, the signal is standing on a cleaner noise floor at 200Hz comparing to the DC.

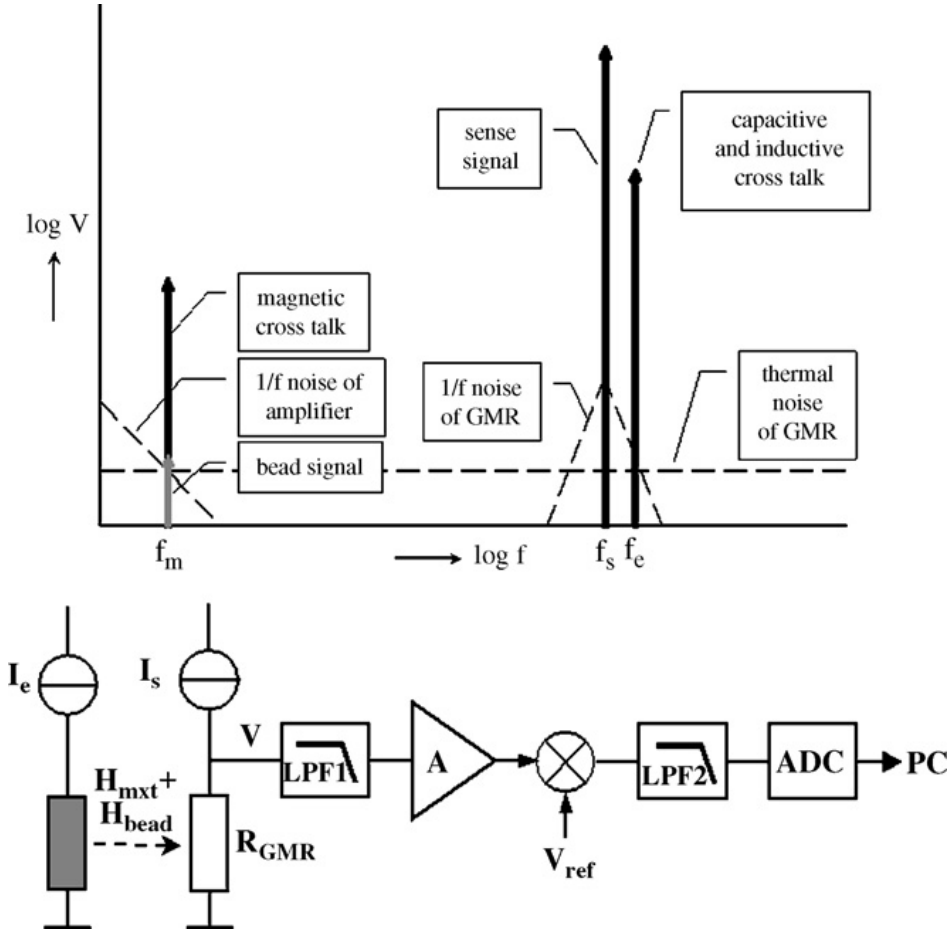

Figure 4-6 Working principle of mixing frequency method[38]

$$V_{GMR}(t) = I_{GMR}(t)(R_0 + \Delta R)$$

$$= B\cos(2\pi f_s t)\{R_0 + A\cos(2\pi f_e t)\}$$

$$= BR_0\cos(2\pi f_s t) + \frac{1}{2}AB\cos(2\pi(f_s - f_e)t) + \frac{1}{2}AB\cos(2\pi(f_e + f_s)t)$$

CT LT HT

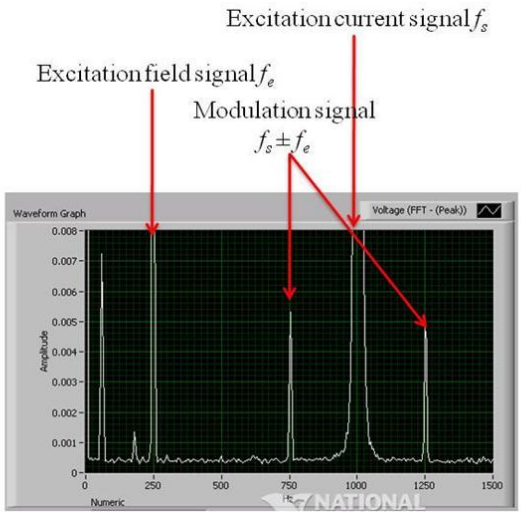

Figure 4-7 Relationship between mixing terms and sensing current and excitation field

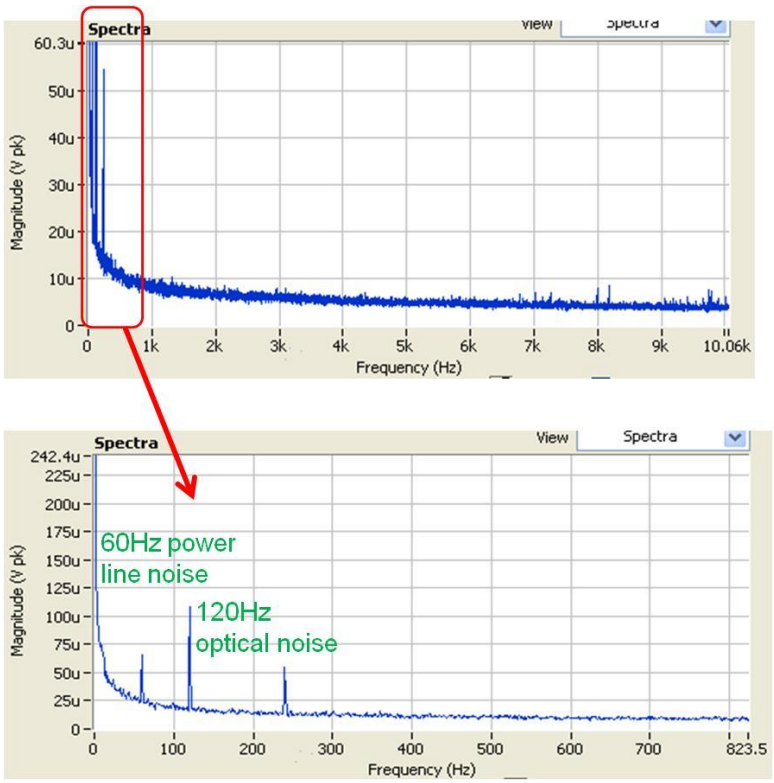

Figure 4-8 Noise floor on a normal linear sensor

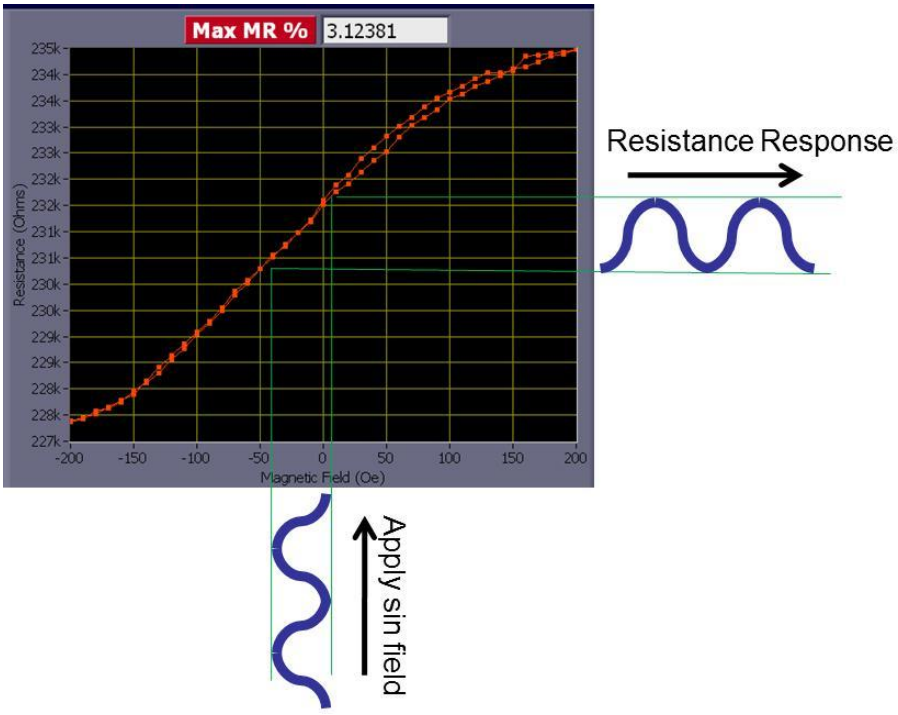

Figure 4-9 An AC resistance response of a GMR sensor in the linear region

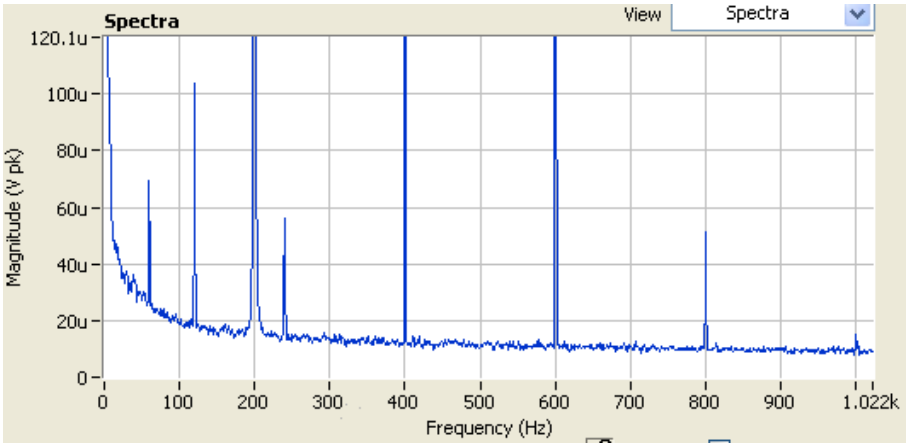

Figure 4-10 Noise floor on a normal linear sensor with a 200Hz field

4.3 Measurement Results

Figure 4-11 and Figure 4-12 shows that real time measurement of 1st side tone and 2nd side tone. Both of the 1st and 2nd side tone can be used to monitor the binding process of MNPs to the surface of the sensor. However, 1st side tone is usually used because of its large amplitude.

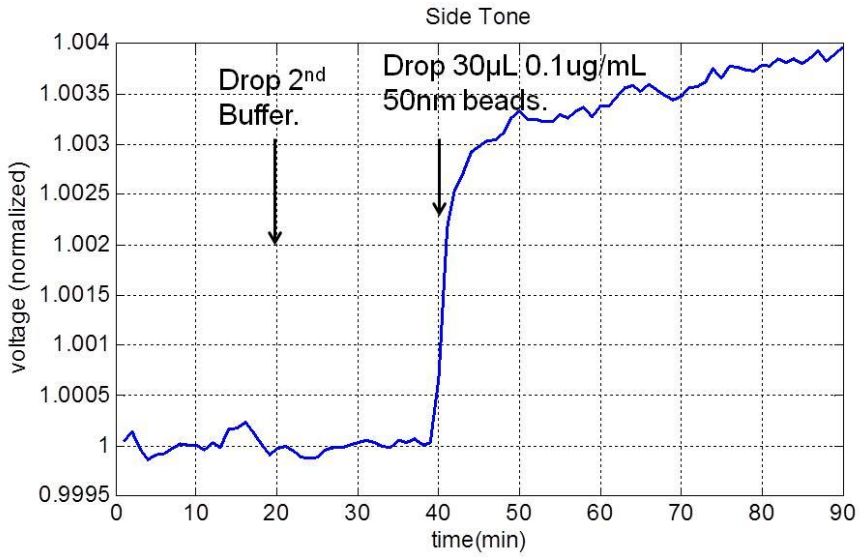

Figure 4-11 1st Side tone of GMR in real time by dropping 50nm MACS with biotin-streptavidin binding

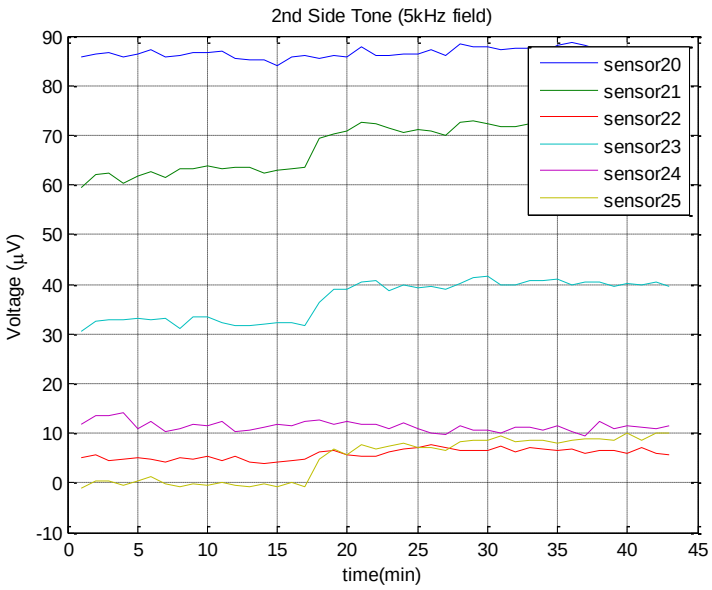

Figure 4-12 2nd Side tone of 6 sensors in real time with MACS50 dropped at 17 min. A bias field is supplied. Sensor 21, 23 and 25 are printed with 10ng IL6. Sensor 20, 22 and 24 are control sensors with BSA blocking.

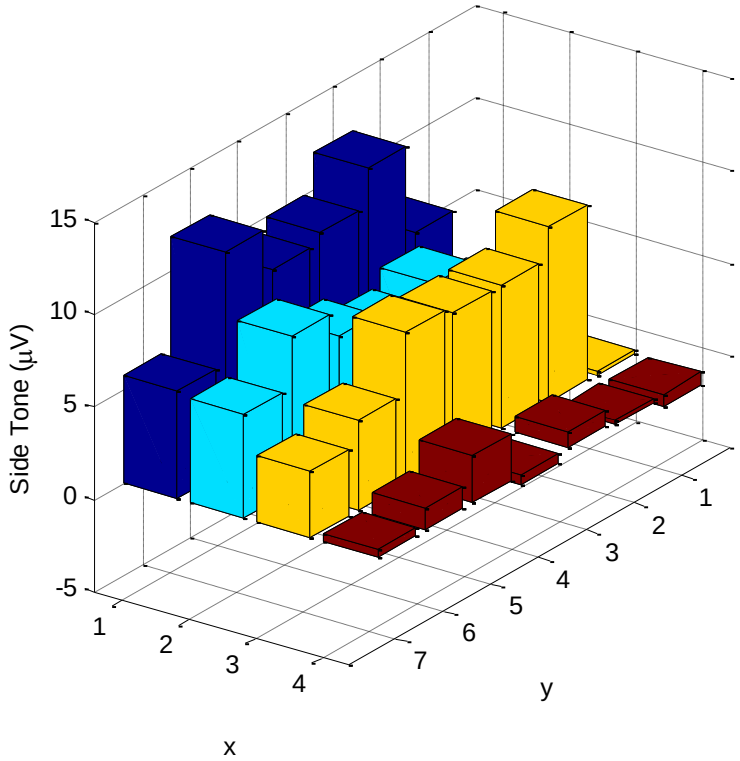

Figure 4-13 The signal of a sensor array. The red bar shows the control sensors and the others are active sensors. The first row indicates the reference sensors under silicon oxide.

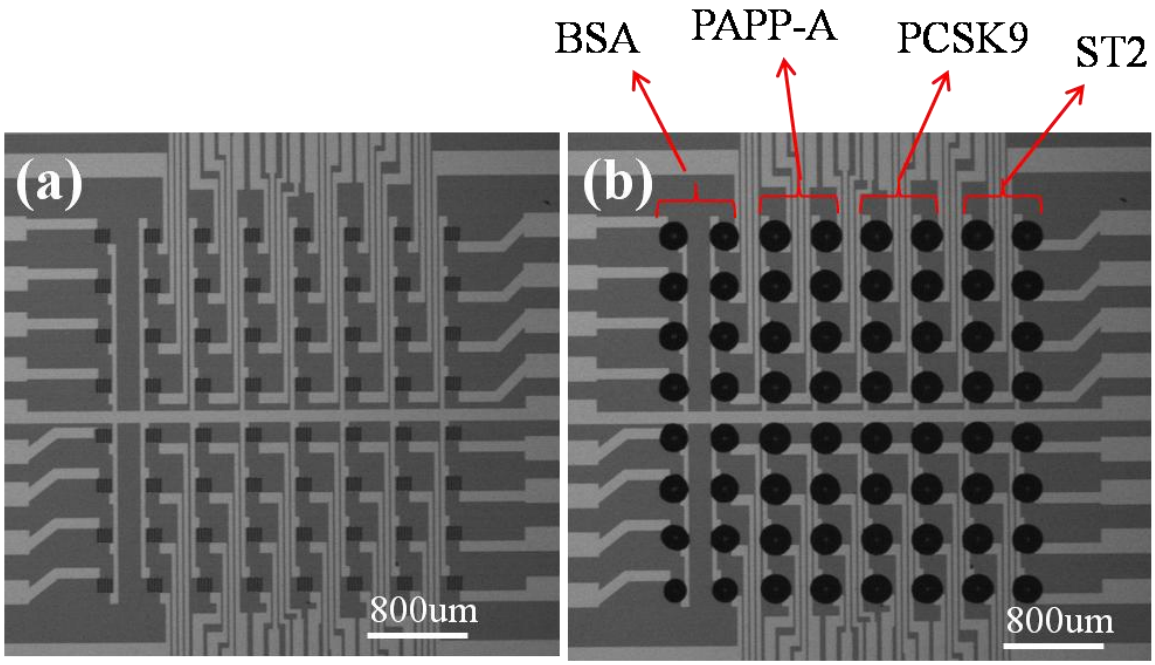

Figure 4-14 Image of 3 printed capture antibody and BSA control on one sensor

The measurement results shown in Figure 4-15 indicate the detection range for PAPP-A is 1 ng/mg to 10 µg/mL. Figure 4-16 shows the detection range for PCSK9 is 433.4 pg/mL to 4.334 µg/mL. Figure 4-17 shows the detection range for ST2 is 40 pg/mL to 400 ng/mL

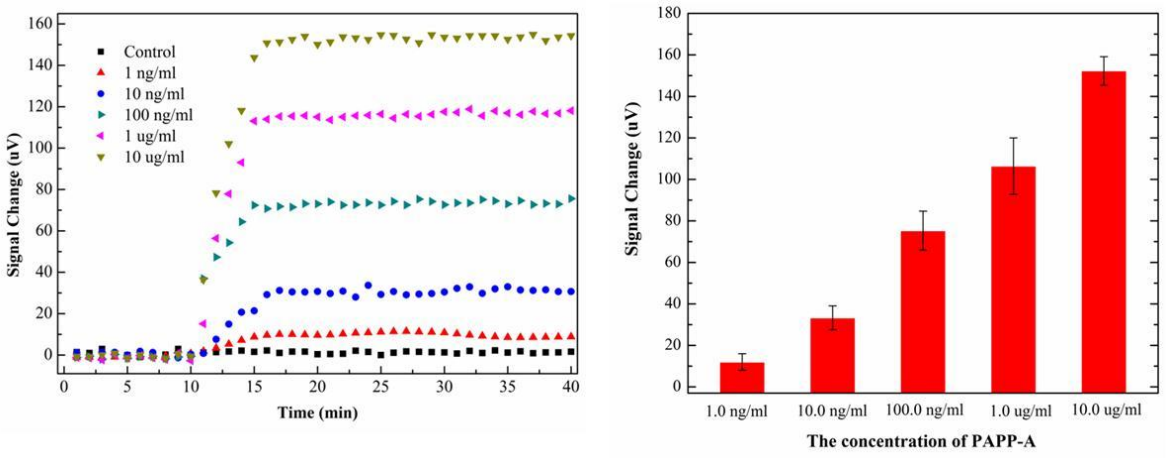

Figure 4-15 Left shows the real time measurement for 5 order concentration of PAPP-A antigen. Right shows the signal distribution of each concentration.

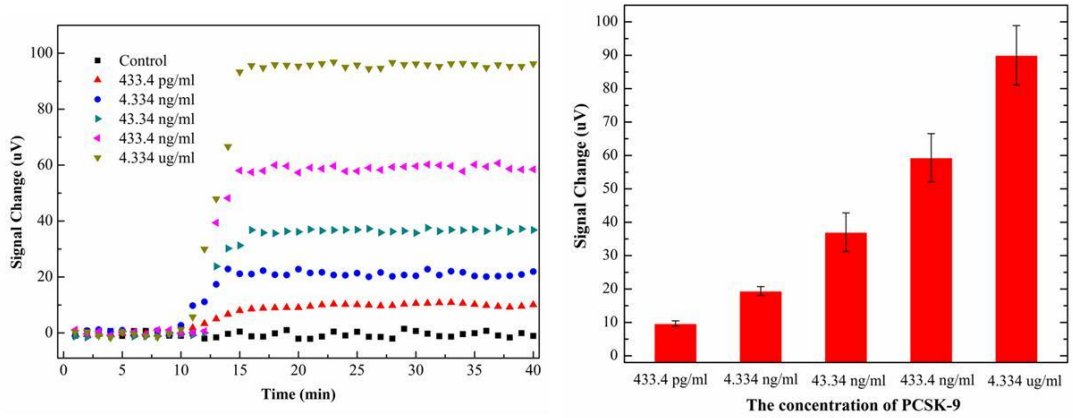

Figure 4-16 Left shows the real time measurement for 5 order concentration of PCSK9 antigen. Right shows the signal distribution of each concentration.

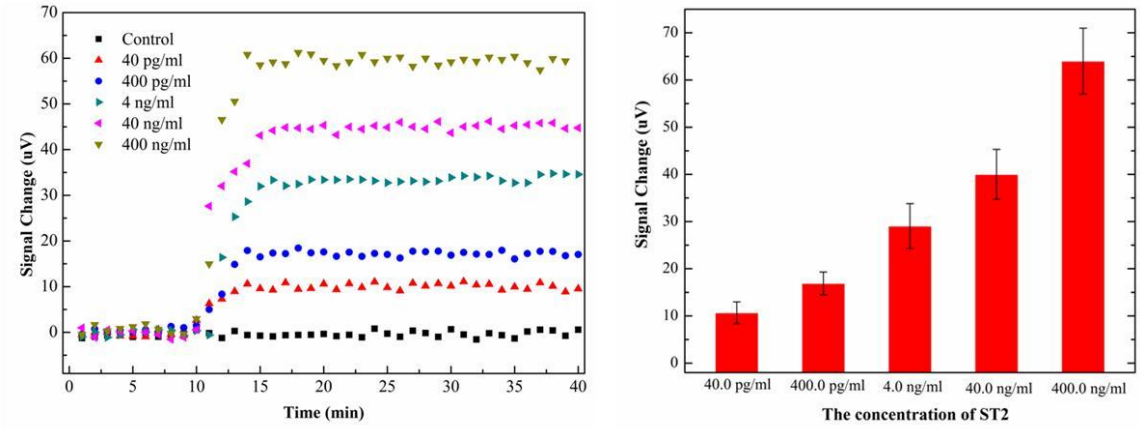

Figure 4-17 Left shows the real time measurement for 5 order concentration of ST2 antigen. Right shows the signal distribution of each concentration.

4.4 GMR Model

To explain the increase of signal caused by the MNP, a GMR model is proposed as in Figure 4-18. The dipole field form the fixed layer magnetizes the MNPs, and the stray field of the MNPs 'frees' the free layer from the fix-free layers coupling. As a result, the effective DC field on the free layer decreases, and the free layer moves into a more linear region. Thus the 1st side tone, interpreted as the slope of the transfer curve, will increase as moving to the sharp region. The 2nd side tone, interpreted as the second derivative or

the asymmetry of the curve, will decrease as moving to the center region. The carrier tone, interpreted as the static resistance R_0, will decrease as the free layer moving towards the direction of the fixed layer.

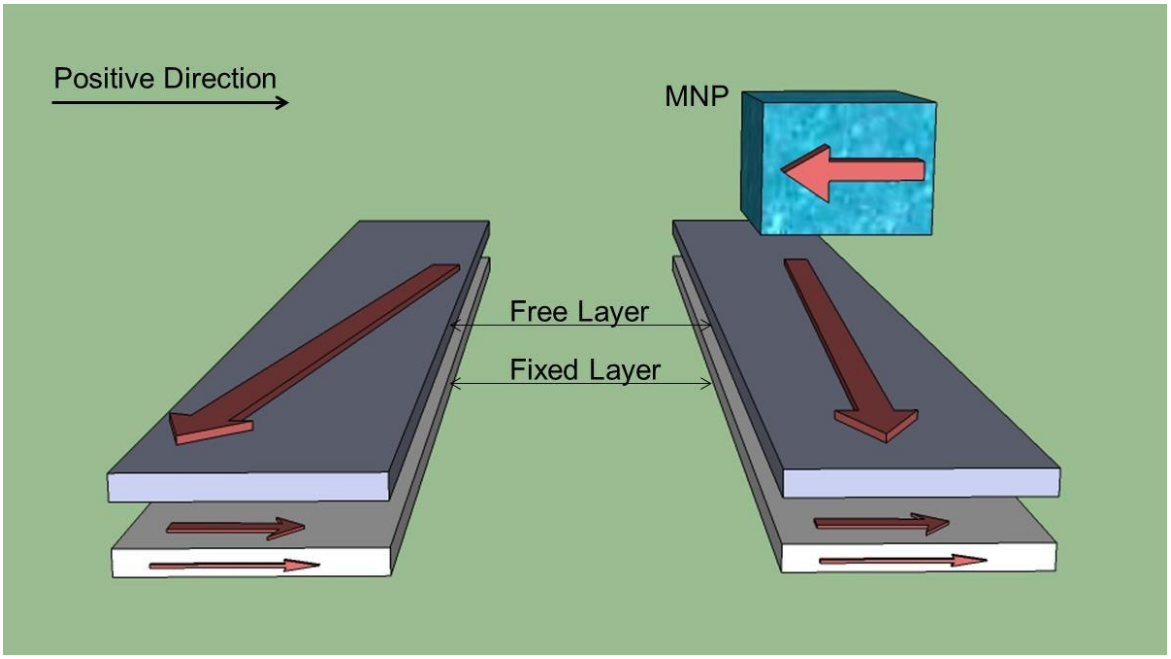

Figure 4-18 GMR detection model

The prediction of the proposed model has been confirmed with the measurement results in Figure 4-19. However, there are still a lot of interactions complicating the model. Such as the ac stray field from the MNPs, and the free layer-MNP interaction. Before it is fully understand, fixed layer-MNP coupling can serve as a good guidance to explain the detection system.

A real time measurement on a 4*7 GMR sensor array is also performed. The results from this measurement are shown in Figure 4-20, Figure 4-21, and Figure 4-22. The left 4 sensors are covered under thick silicon oxide protection layer, thus will not be affected by the MNPs. The other 24 sensors all show strong signals to the MNPs, and the signal levels are pretty uniform. Figure 4-22 shows the static resistance of the sensor, which is independent of the external applied field. Although it suffers from the DC drifting noise due to the temperature and leakage conditions, it truly indicates the possibility of a field free GMR sensor.

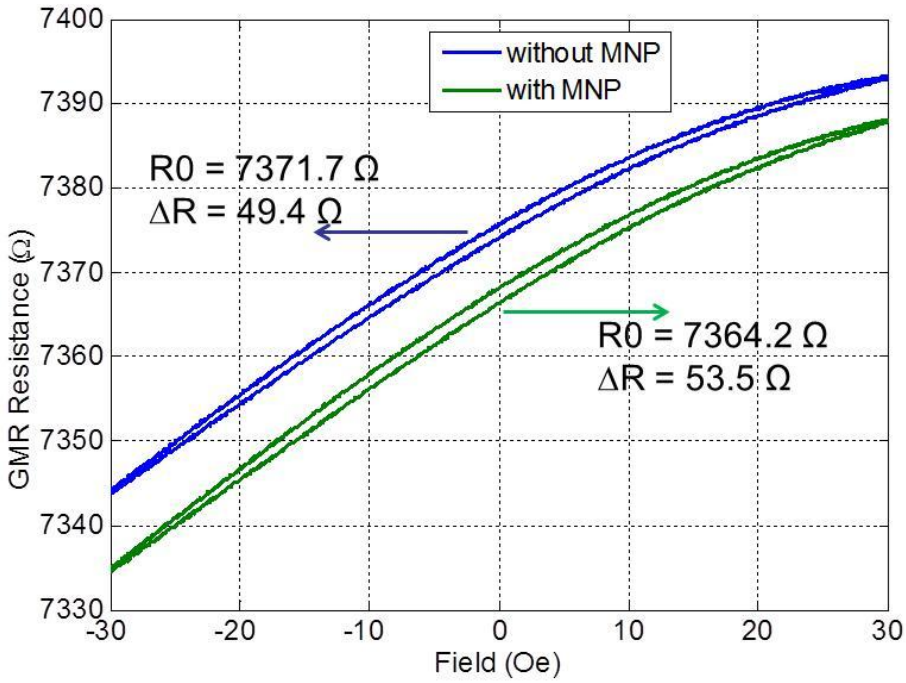

Figure 4-19 GMR transfer curve with and without MNPs on the sensor surface.

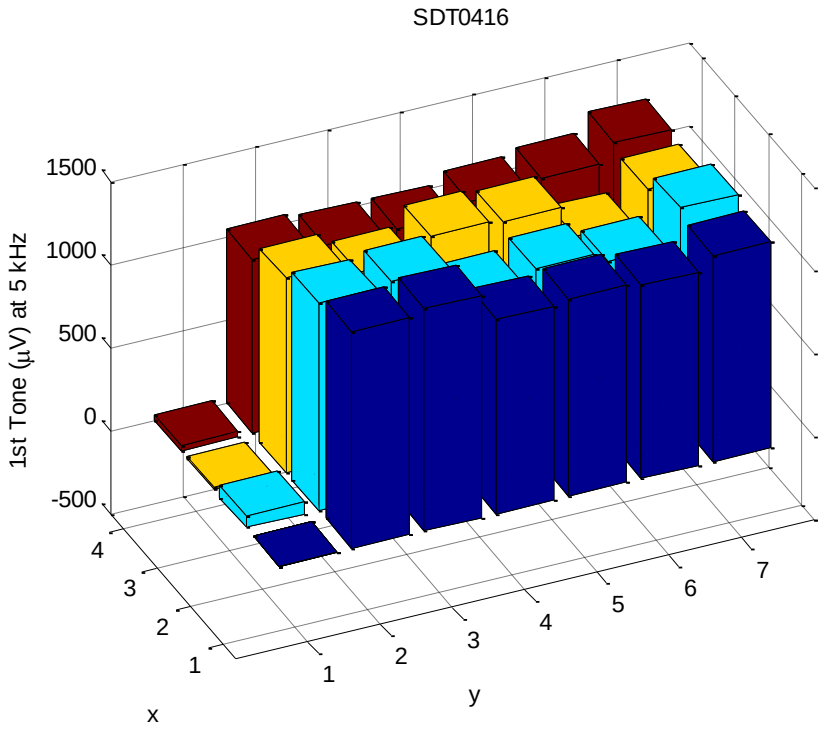

Figure 4-20 The 1st side tone response of GMR to the MNPs.

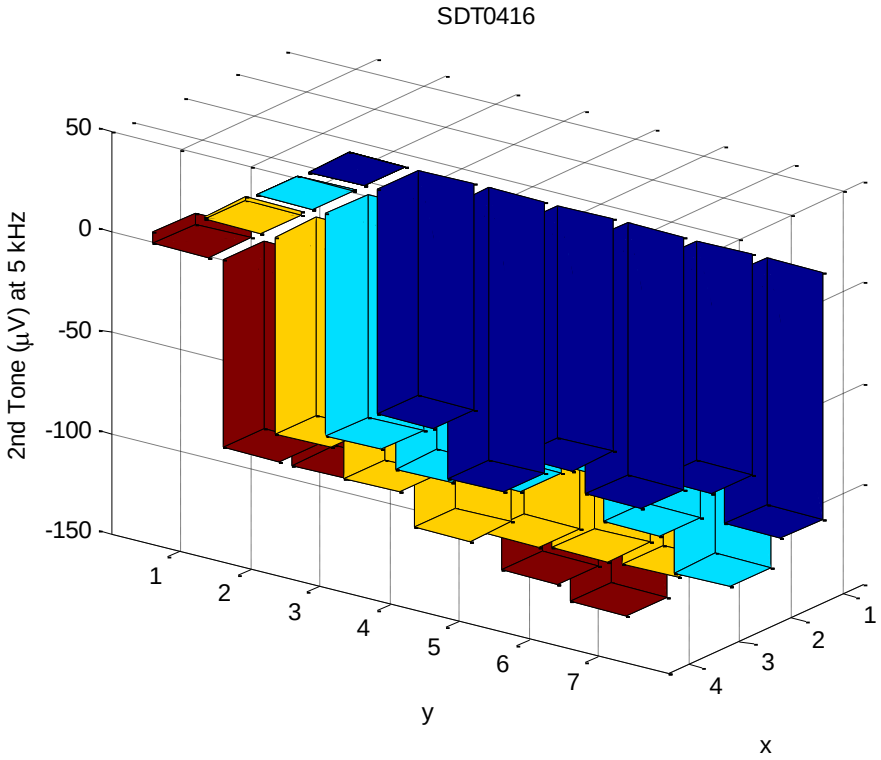

Figure 4-21 The 2nd side tone response of GMR to the MNPs.

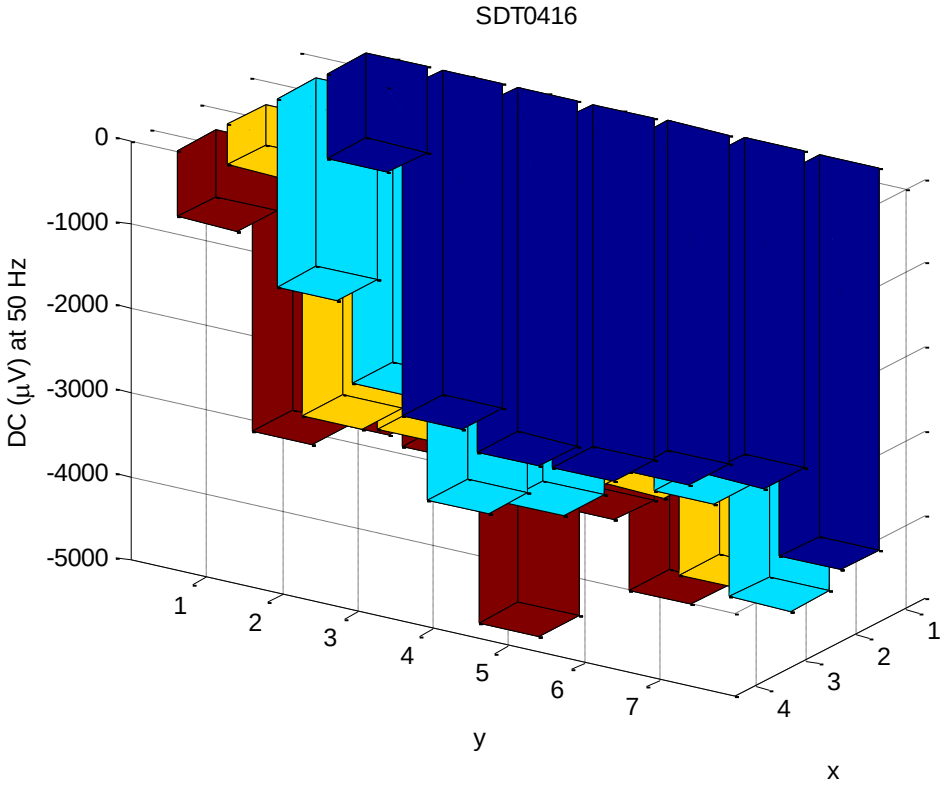

Figure 4-22 The Carrier tone response of GMR to the MNPs

4.5 GMR Sensitivity

10 μA ac current is applied to the sensor. Use a DC bias field to align free layer magnetization to the easy axis. Change the ac field (30Hz) amplitude to simulate the effect from MNPs. The results are shown in the table below.

	AC field (Oe)	97.7	93.5	91	87.8	
DC bias (Oe)	Side Tone (mV)					Sensitivity (μV/Oe)
0		6.07	6.05	6.03	6	7.1
16		5.85	5.83	5.79	5.75	10.1
30		5.2	5.16	5.4	5.03	17.2
45		4.54	4.48	4.42	4.35	19.2
63		3.92	3.86	3.79	3.71	21.2
77		3.38	3.32	3.26	3.19	19.2

Table 4-1 GMR sensitivity at different DC bias

Side Tone Amplitude decreases with the DC bias field. The reason is that the DC field fixes the free layer and decreases the effect of AC field.

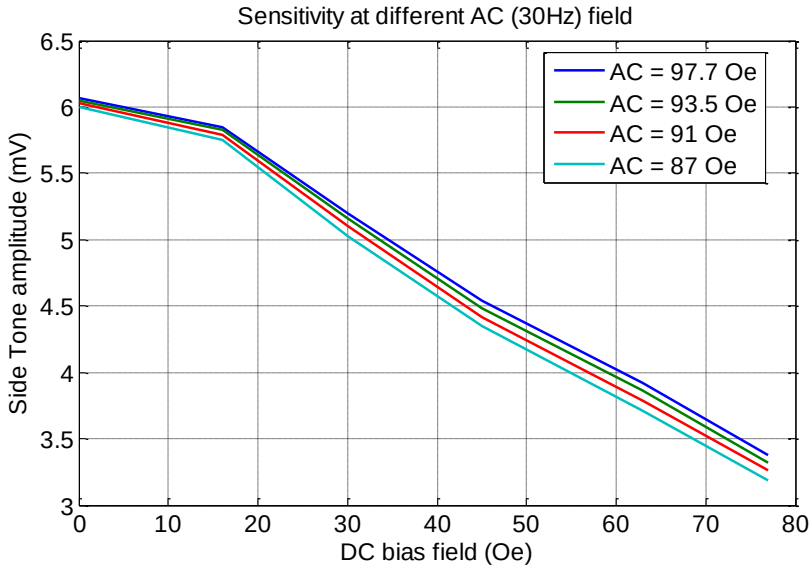

Figure 4-23 Side tone along DC bias field with different AC field

Sensitivity increases with the DC bias field. The reason is that DC bias field drives the sensor into linear region.

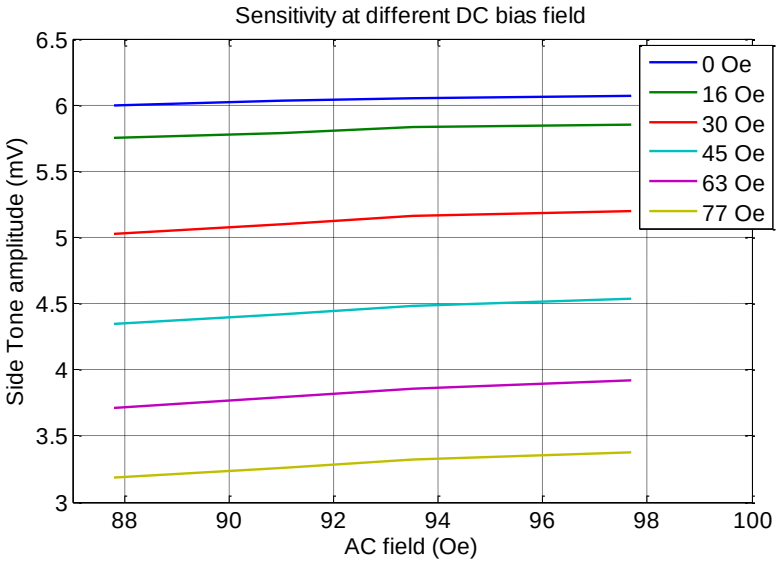

Figure 4-24 Side tone along AC field with different bias DC field.

4.6 GMR Noise

The following figures are used to test Todd's linear sensor (5kΩ) and YL's 40*80 sensor (150Ω) in roughly balanced Wheatstone bridge. The input is 1V DC. The output

depends on MR, not on resistance.

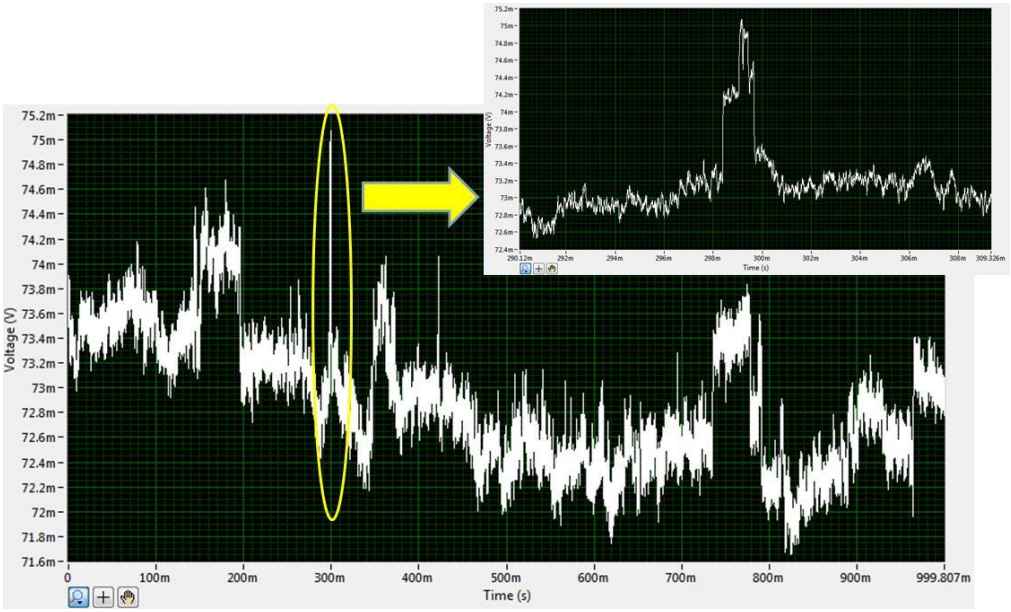

Figure 4-25 Noise of linear sensor in time domain.

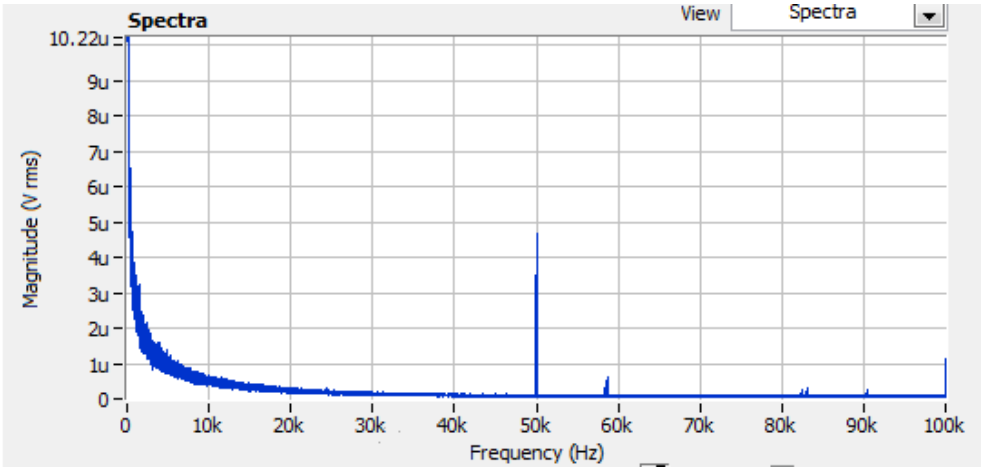

Figure 4-26 Noise of linear sensor in frequency domain.

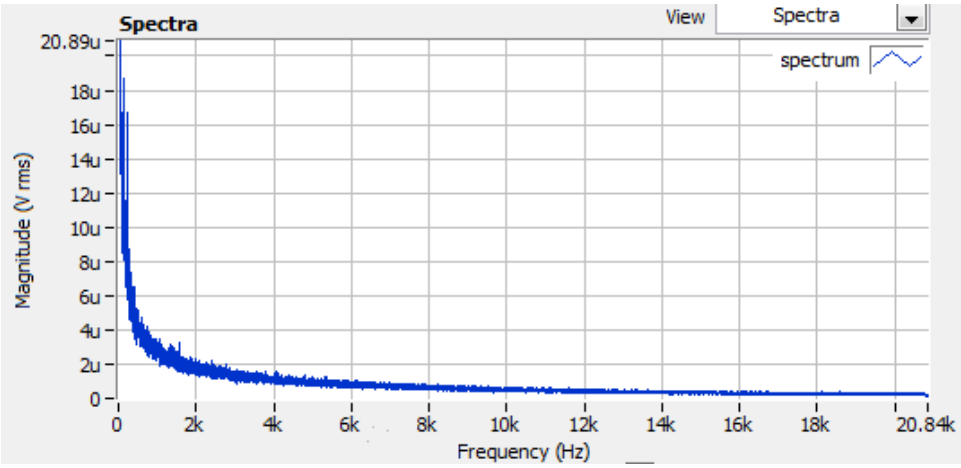

Figure 4-27 Zoomed in plots of Figure 4-26

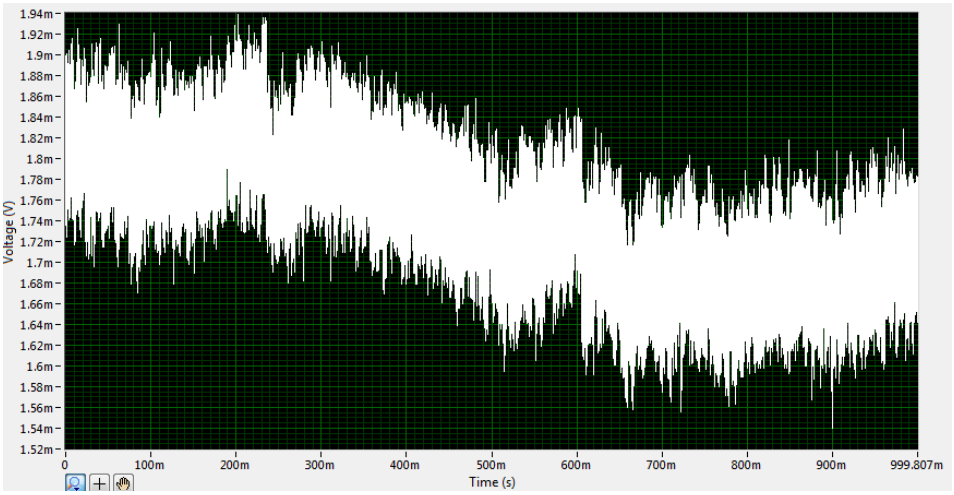

Figure 4-28 Noise of 40*80 sensor in time domain.

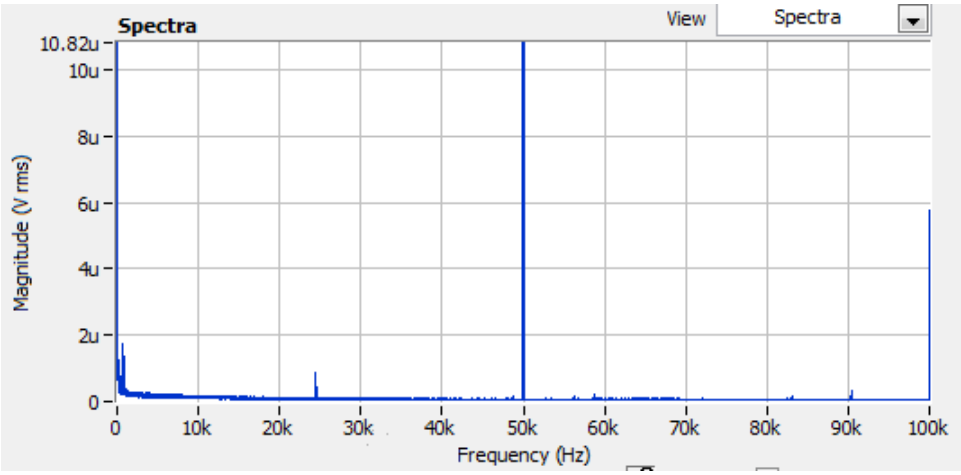

Figure 4-29 Noise of 40*80 sensor in frequency domain.

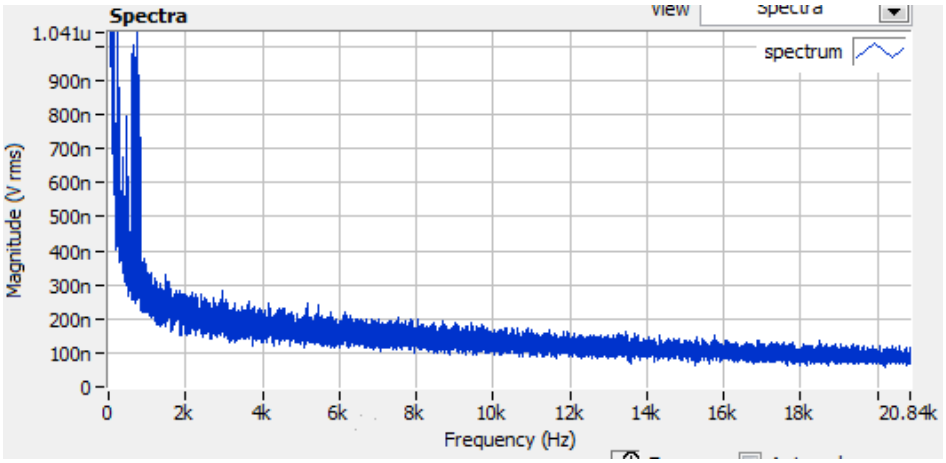

Figure 4-30 Zoomed-in plots of Figure 4-29

4.7 GMR Drift

The following figures show the signal drift by changing the solution, temperature and lights. The tests use linear GMR sensor SDT0314. The results show that temperature can affect carrier tones and 1st side tones dramatically, while lights affect 2nd side tone dramatically.

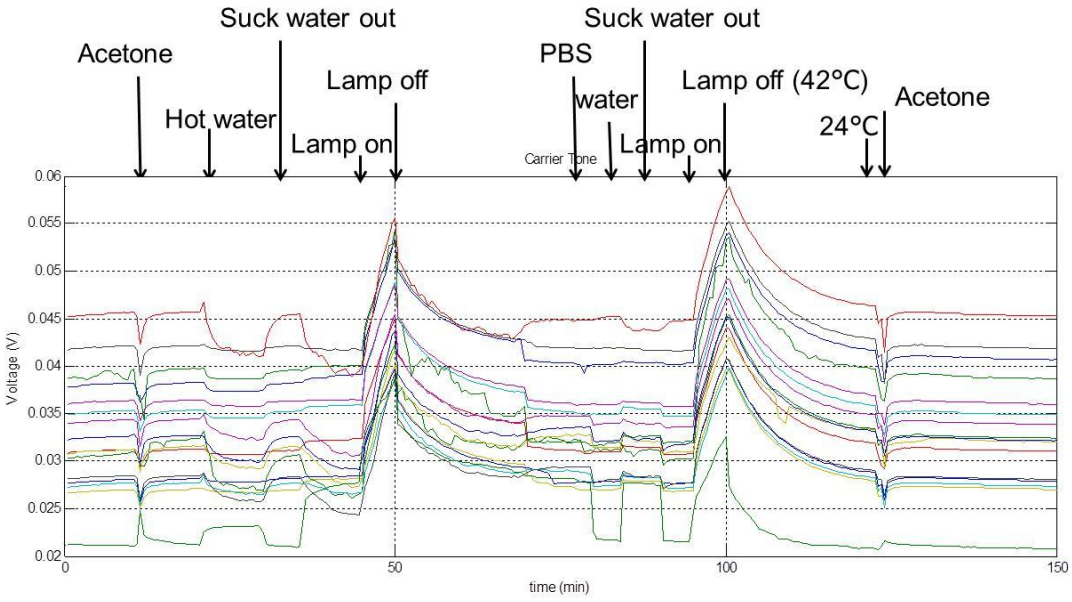

Figure 4-31 Carrier tone drift

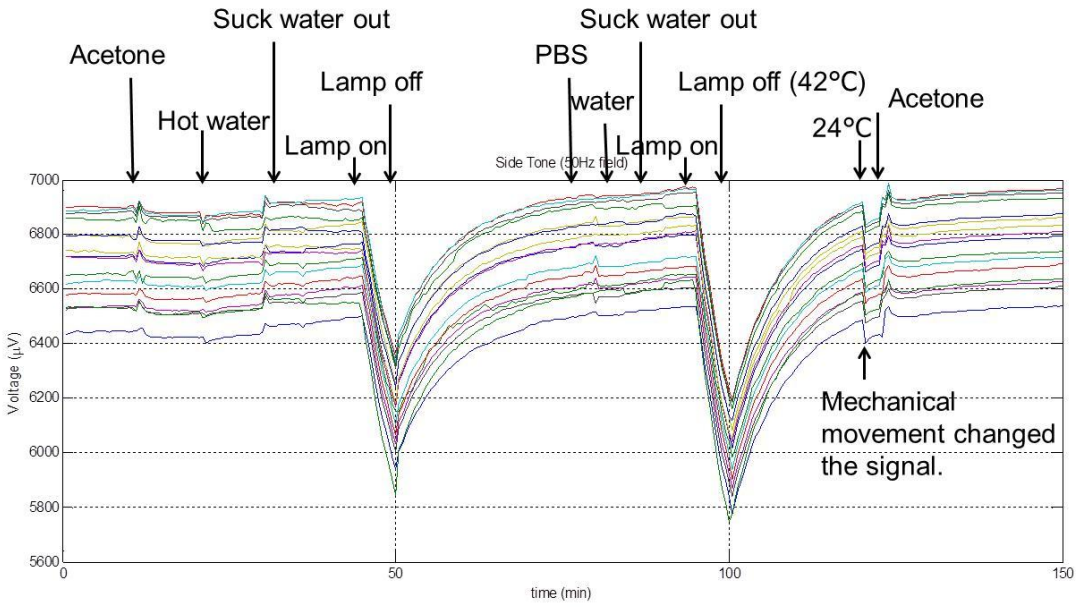

Figure 4-32 1st side tone drift

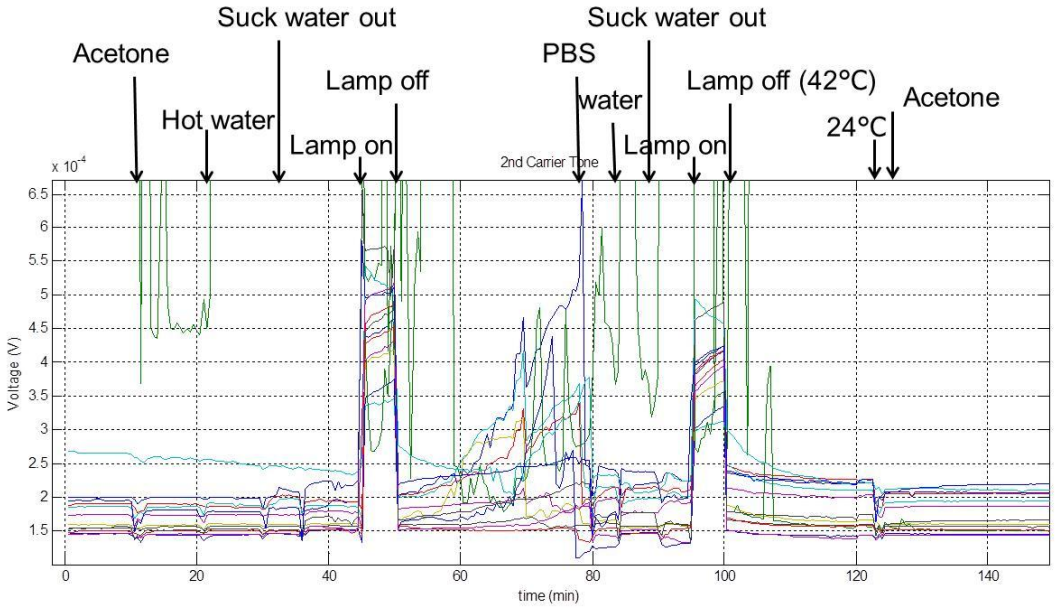

Figure 4-33 2nd side tone drift

4.8 Optical Effects

The following figures show the optical effects on the signal due to the semiconductor effects occurring on the Silicon wafer. The input is a sine signal with amplitude of 2 V. The resistance of sensor is around 2.8 kΩ. So the current amplitude is around 0.36 mA.

As shown in Figure 4-35, in the range of negative input of the 2 Hz sine wave, the output is obviously distorted. When the sensor is exposed to a light source, the output is heavily affected by the light. The 120 Hz spikes in the output signal come from the 120 Hz strobes from the fluorescent light. Figure 4-36 and Figure 4-37 show the transfer curve of input-output in dark and in optical light. In the positive input, the transfer curve is linear functioning like a resistor. In the negative input, the transfer curve shows hysteresis and distortion. And these effects get amplified by optical lights. When the inputs are negative, the silicon substrate has a voltage around -0.3 V. This leakage voltage is probably from the input probe that penetrates through the silicon dioxide protection layer. Silicon, as a semiconductor material, shows nonlinear semiconducting property and also can be affected by the lights. This leakage current through Si is not wanted, and needed to be addressed by either increasing protection layer or avoiding negative voltage. Further increasing the input frequency to 10 Hz and 100 Hz, the transfer loop opens more, especially in the negative part. This shows the capacitive or inductive components. The p-type silicon substrate usually has a negative threshold voltage, and it means a negative voltage on the metal can make the inversion layer charge equal to zero. Further decreasing the voltage will turn the junction on, and the capacitance will suddenly drop at the threshold voltage and slowly increase in the depletion region towards accumulation region.[39] At the depletion region, the optical effects will occur. Also due to the small capacitance, the impedance includes resistance and a big reactance $1/j\omega C$.

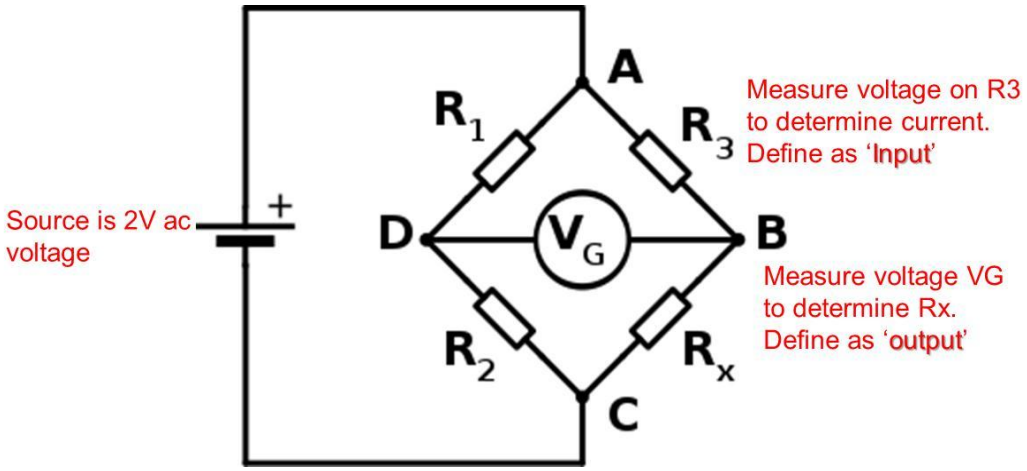

Figure 4-34 Testing condition

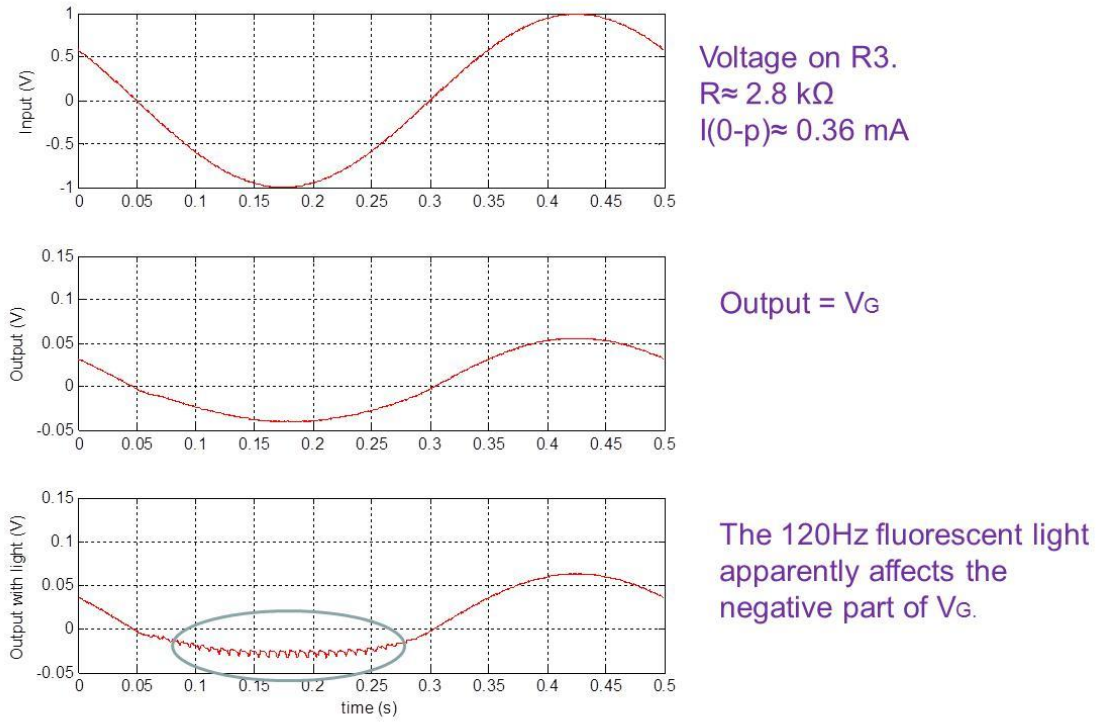

Figure 4-35 Top figure shows an input 2Hz signal. Middle figure shows the output signal from the Wheatstone bridge. Bottom figure shows the output signal modulated by the fluorescent light.

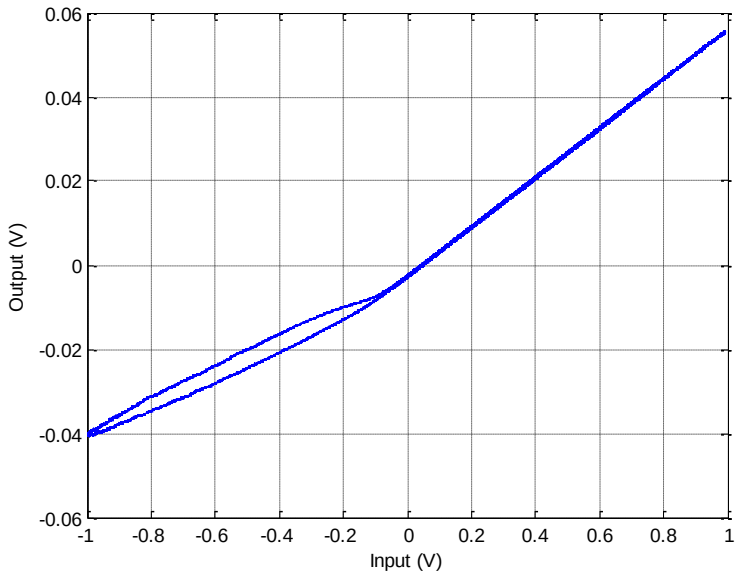

Figure 4-36 Transfer curve of input-output in dark in 2 Hz

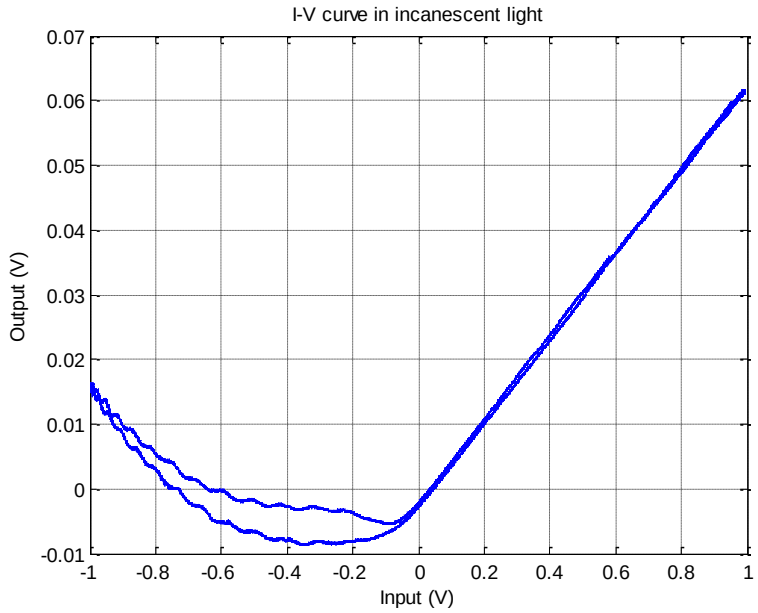

Figure 4-37 Transfer curve of input-output in incandescent light in 2 Hz

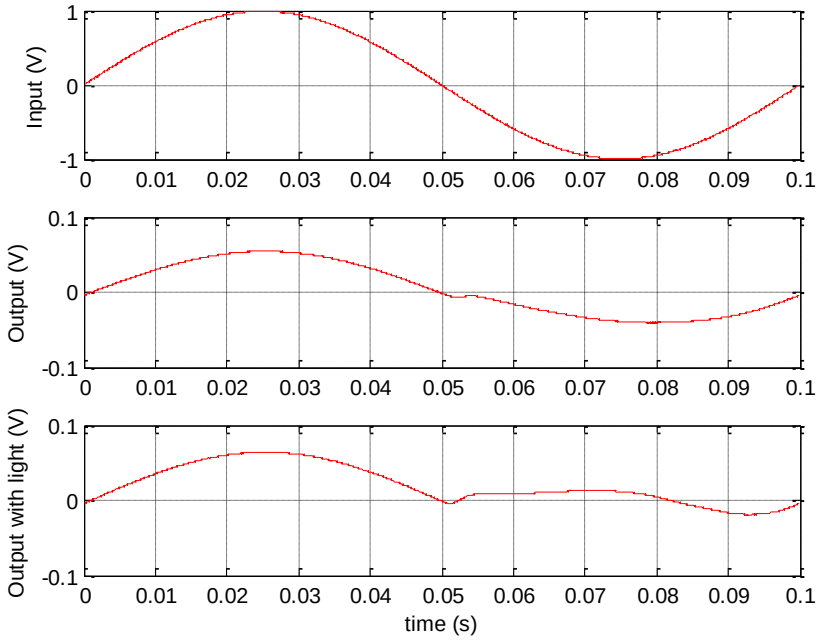

Figure 4-38 Top figure shows an input 10 Hz signal. Middle figure shows the output signal from the Wheatstone bridge. Bottom figure shows the output signal modulated by the incandescent light.

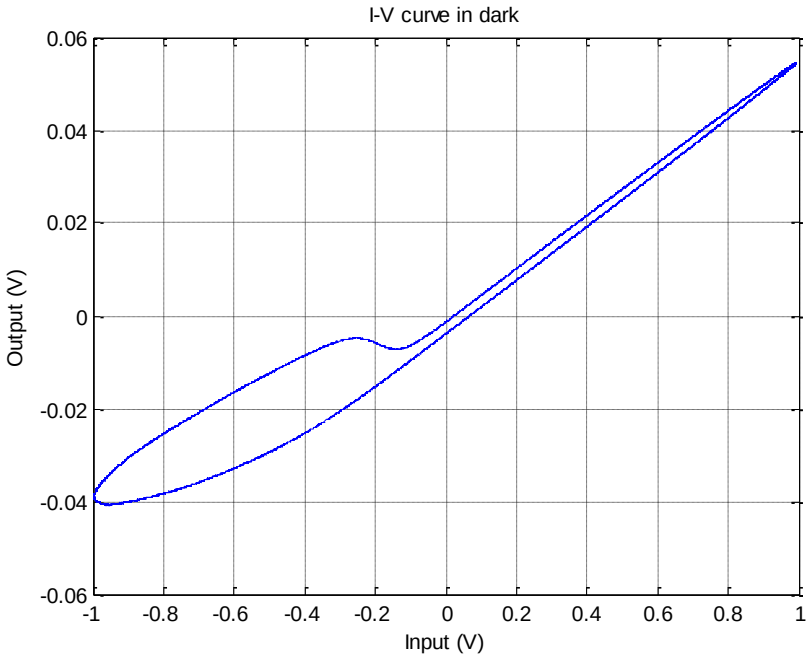

Figure 4-39 Transfer curve of input-output in dark in 10 Hz

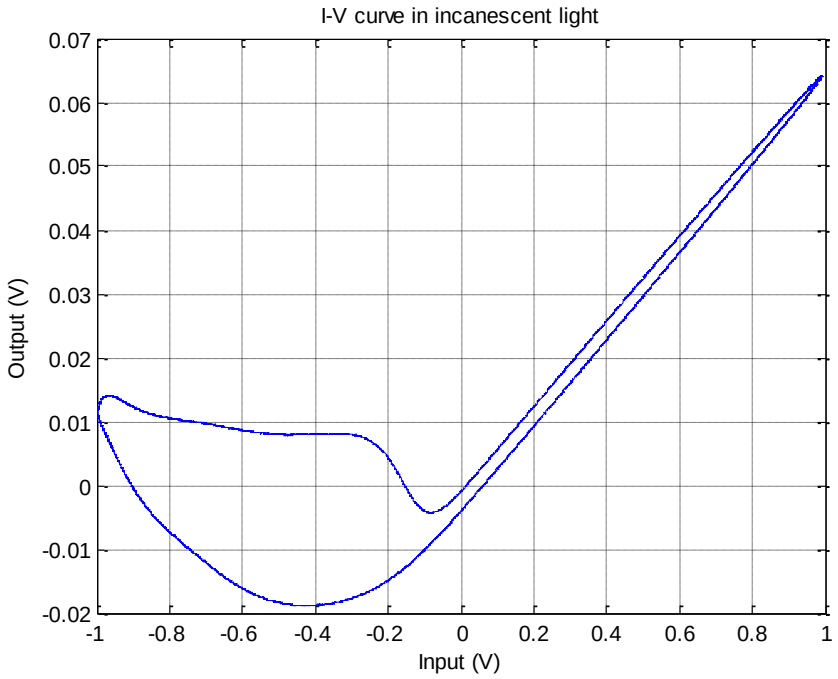

Figure 4-40 Transfer curve of input-output in incandescent light at 10 Hz

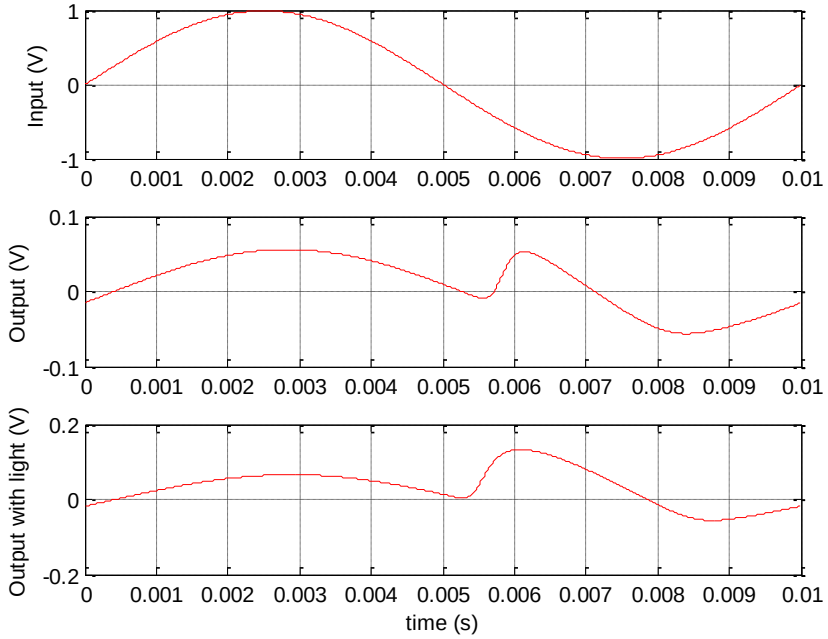

Figure 4-41 Top figure shows an input 100 Hz signal. Middle figure shows the output signal from the Wheatstone bridge. Bottom figure shows the output signal modulated by the incandescent light.

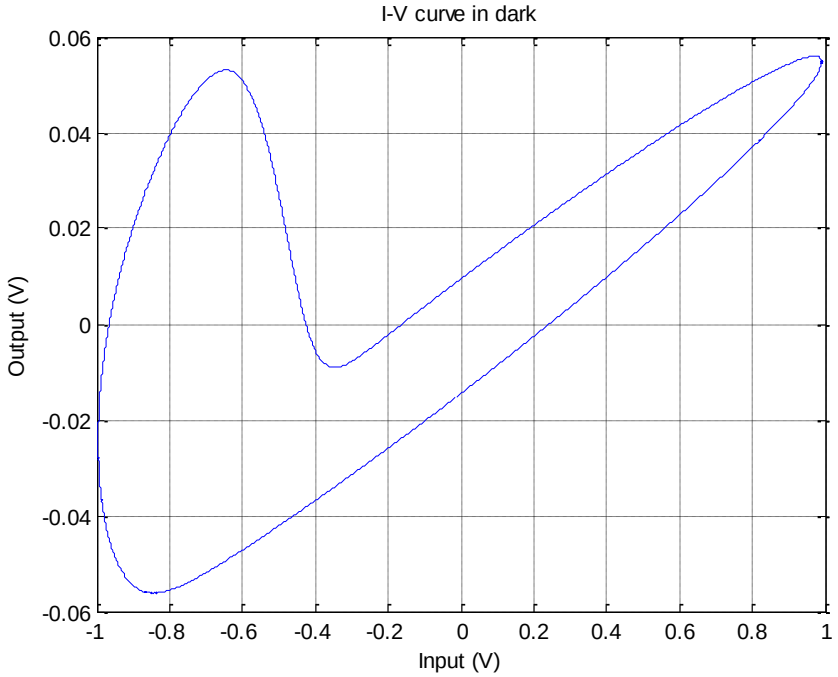

Figure 4-42 Transfer curve of input-output in dark at 100 Hz

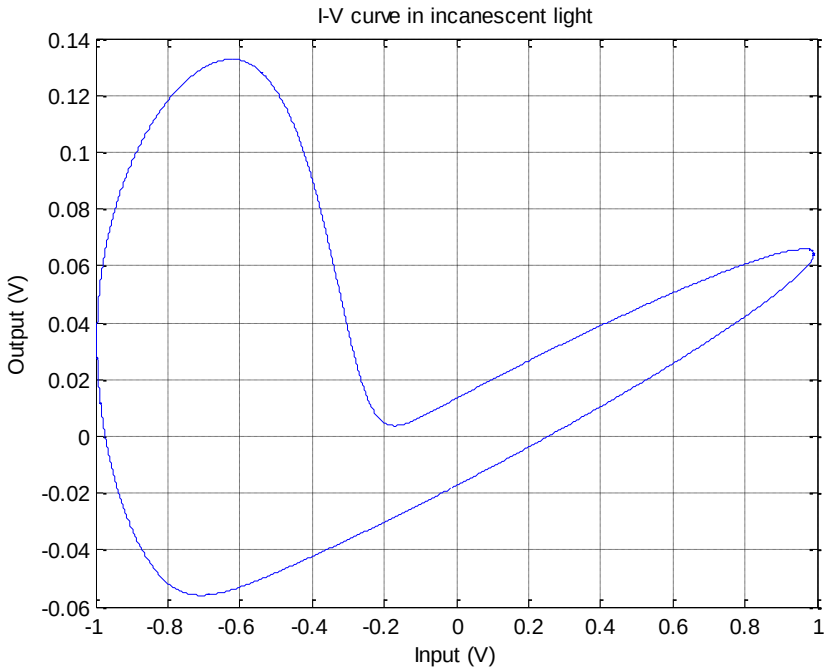

Figure 4-43 Transfer curve of input-output in incandescent light at 100 Hz

4.9 Detection Circuit

System overview is shown in Figure 4-44. A microcontroller generates a pilot tone as the voltage input to the Wheatstone bridge, and another signal for coil driver. The sensor array will be measured in sequence by multiplexes. The output signal will be amplified and fed to the microcontroller.

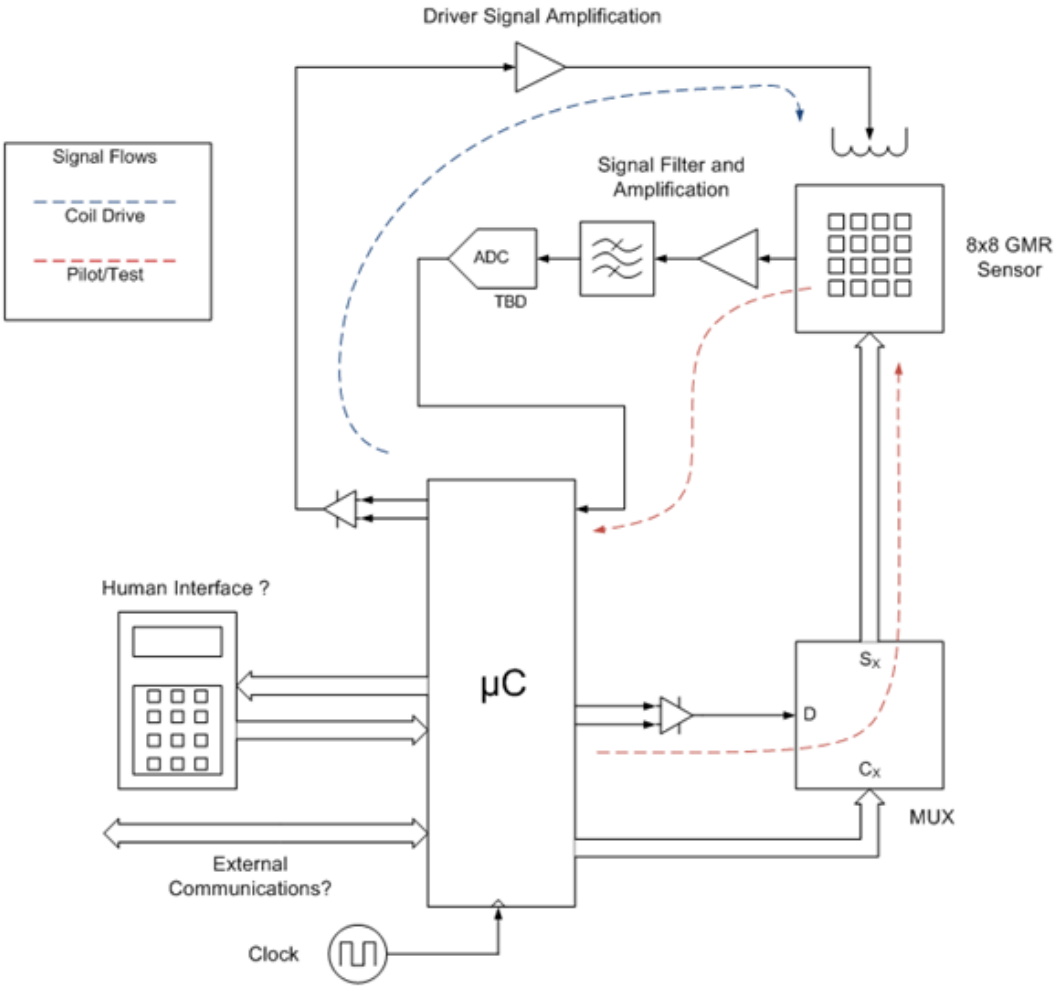

Figure 4-44 Schematic of detection system

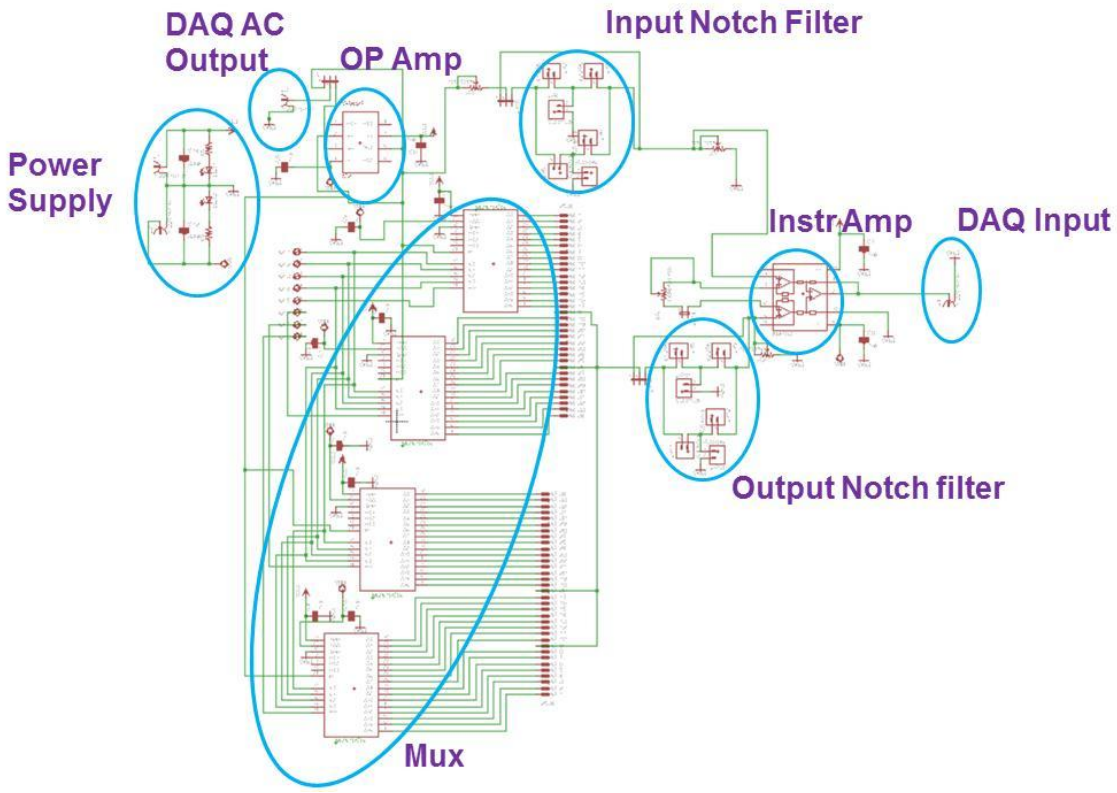

Figure 4-45 Schematic of the detection circuit

The overall detection circuit shown in Figure 4-45 based on Wheatstone bridge is comprised of the following parts.

4.9.1 DAQ： NI USB-6289[40]

Data Acquisition Card has 4 analog outputs channel, and the maximum resolution and sampling rate are 16 bit and 2.8 MS/s. DAQ has 32 analog input channel, and the maximum resolution and sampling rate are 18 bit and 625 kS/s. When operating in the minimum voltage range ±100 mA, digitization has the highest accuracy of 28 μV and highest sensitivity of 0.8 μV. It has a built-in input low pass filter, with -3 dB bandwidth of 40 kHz with filter on and 700 kHz with filter off.

4.9.2 Low Pass Filter

It is observed that the output of DAQ has big 1/f -like noise. So when operating in

low frequency range, the noise is big and will be cascaded to the following circuits. So a low pass filter is needed right after the DAQ output. The low pass filter we use is a passive LC low pass filter.

4.9.3 Input Voltage Follower

The signal provided to the Wheatstone-Bridge is provided by DAQ. DAQ has output impedance of 0.2 Ω, and outdrive current of 20 mA. Although it is capable of driving the Wheatstone-Bridge, we still use an operational amplifier 'TI OPA827'[41] to function as a voltage follower. OPA827 has a Gain-Bandwidth Product (GBW = gain * bandwidth) of 22 MHz, which is more than enough for our application. As shown in Figure 4-46, for unit gain voltage follower, the gain is very flat below 1 MHz, so frequency dispersion by the amplifier can be ignored. Figure 4-47 shows the measured input voltage noise where the load resistance is 10 kΩ. There is strong low frequency noise below 10Hz, and its time domain representation is shown Figure 4-48. At 1 kHz, the input noise voltage e_n spectrum density is about 4nV/√Hz, and the input noise current spectrum $i_n$density is about 2.2 fA/√Hz. For the unity gain buffer configuration shown in Figure 4-49, the total noise power E_o^2 is

$$E_o^2 = e_n^2 + (i_n R_s)^2 + 4k_B T R_s$$

Where R_s is source impedance and $4k_BTR_s$ is thermal noise power. The calculation shows the voltage noise will dominate, and the total noise is about 4nV/√Hz at 1kHz.Both time-domain and frequency-domain shows the noise from OPA827 is much smaller than from DAQ. So for a DAQ based generation and detection system, noise from OPA827 can be ignored.

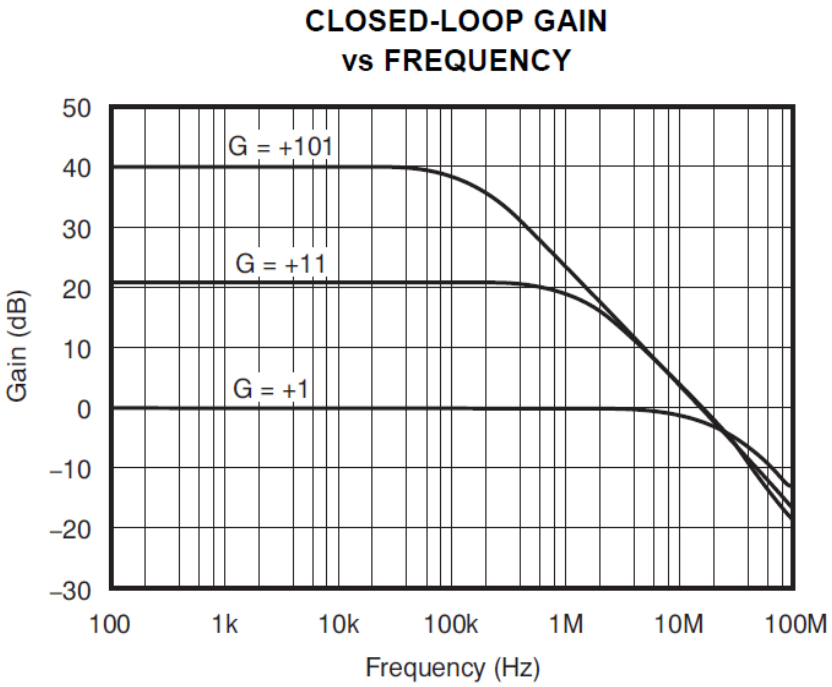

Figure 4-46 Closed-loop gain along frequency of OPA827

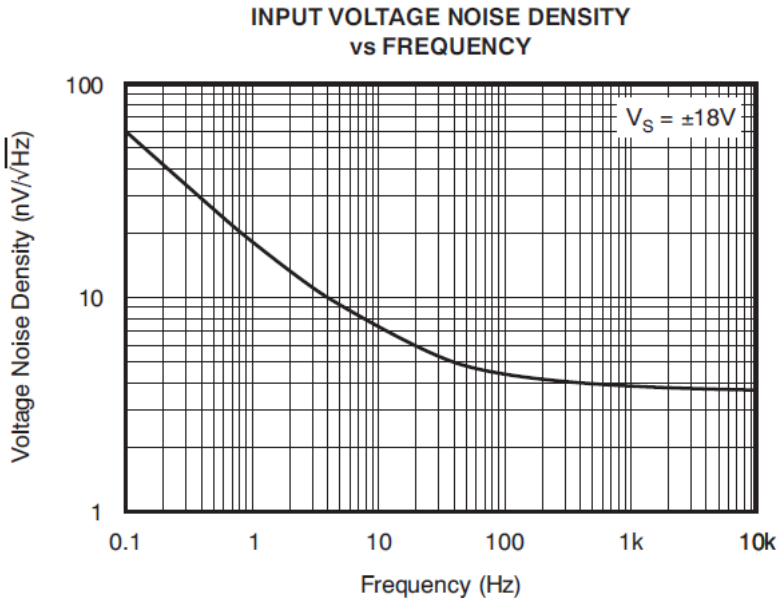

Figure 4-47 Input voltage noise density along frequency of OPA827

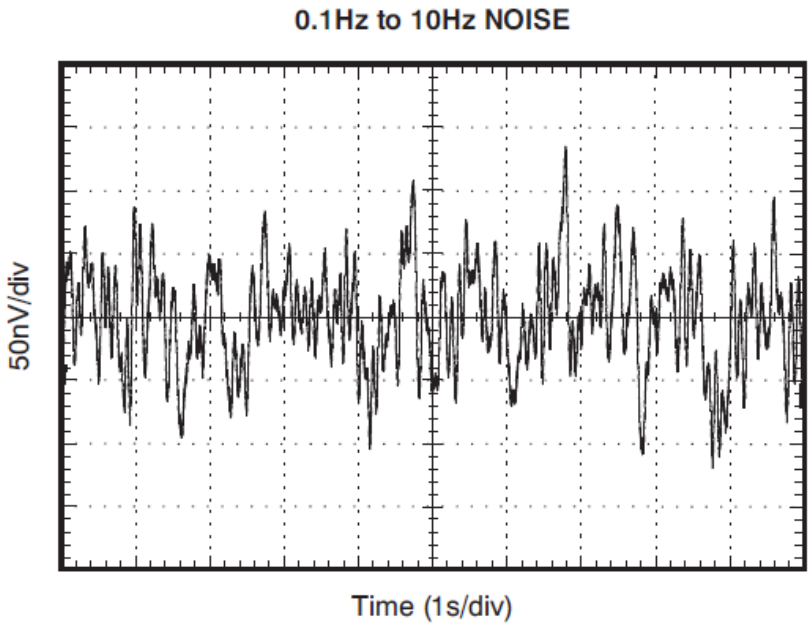

Figure 4-48 Low frequency output noise in time domain of OPA827

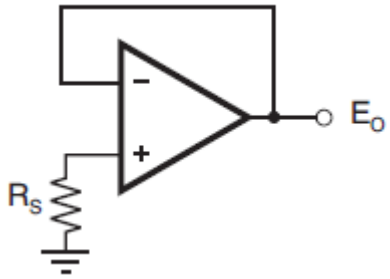

Figure 4-49 Unity-Gain Buffer Configuration

4.9.4 Multiplexer

The GMR sensor array will be addressed by Multiplexers ADG1606[42] and will be measured in time sequence. Each chip has 16 bi-directional single channels (S1 – S16), and the switch of each channel is determined by the 4-bit binary address lines (A0 – A3). All the channels are enabled by an EN pin.

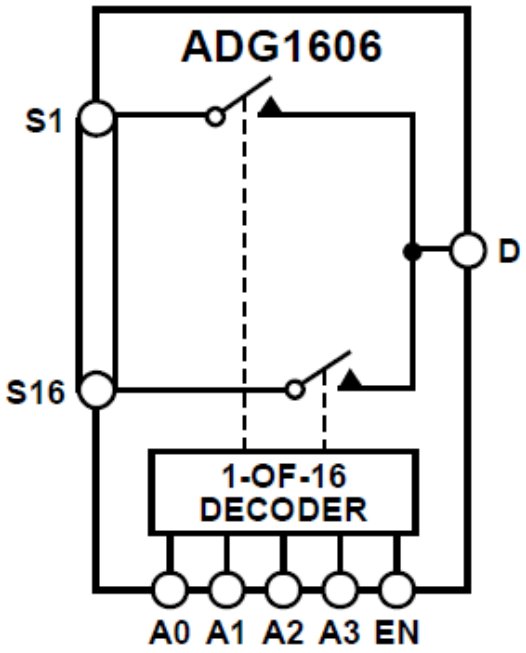

Figure 4-50 ADG1606 Functional Block Diagram

Each channel has an on-resistance of 3.5 Ω in our application. This is small compared to the sensor resistance (several kHz), so can be ignored.

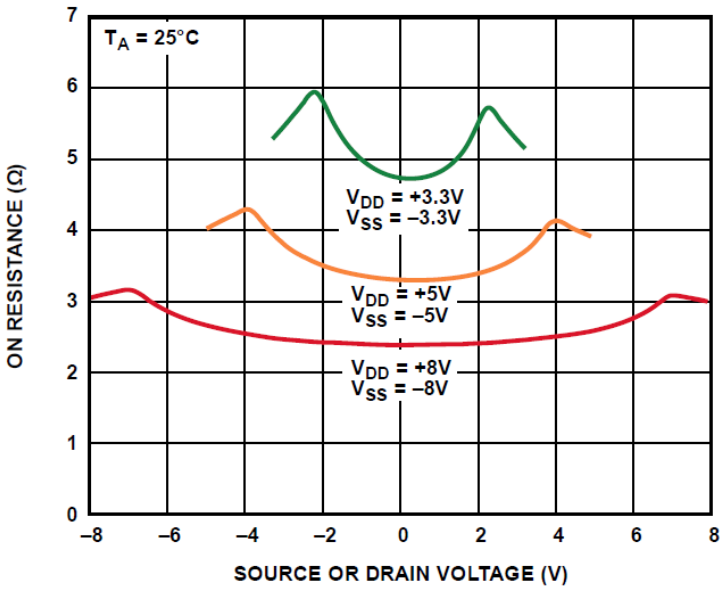

Figure 4-51 ADG1606 on Resistance as a Function of V_D/V_S for Dual Supply

Our circuit has the dual power supply of ±5V. The Source Off Leakage current $I_S$is typically ±0.02 nA. The Drain Off Leakage current I_D is typically ±0.05 nA.Since the leakage current increases dramatically with temperature, the PCB cannot be exposed to high temperature.

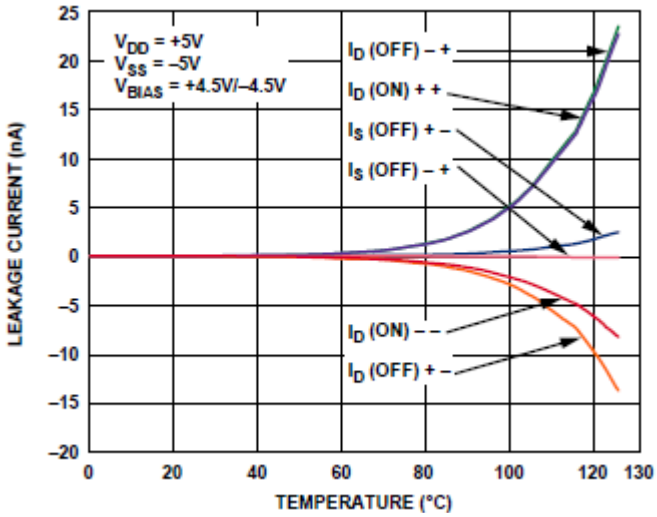

Figure 4-52 ADG1606 Leakage Current as a Function of Temperature for Dual Supply

The maximum continuous current allowed on S (source) or D (drain) channel at room temperature is 259 mA. The current through sensor is usually much smaller than the maximum limit. The transition time of each channel is around 180 ns at room temperature. This transition time will not affect our measurement in kHz range. The crosstalk (off channel affected by on channel) and off isolation (between S and D in an off channel) is from -90 dB to -80 dB in the frequency range from 30 kHz to 100 kHz. The crosstalk and leakage are small and can be ignored. The frequency response of an on channel is very flat below 1 MHz, so frequency dispersion can be ignored and signal will not be distorted through a channel. The total harmonic distortion plus noise for an on-channel is 0.04%.

Overall, the Multiplexer can be treated as an ideal switch in our application. However, the noise level of the Multiplexer is not indicated in the datasheet. Out test results show that a dis-enabled chip will contribute to the overall noise level. So a physical Reed relay (Coto Tech 9011-05-11) is used to isolate each multiplexer.

4.9.5 Output Voltage Amplifier

The final stage of signal will be amplified 10 to 100 times by an instrumentation amplifier INA163[43]. The instrumentation amplifier is designed in such way that the gain G can be controlled by an external resistance R_G,

$$G = 1 + \frac{6000}{R_G}$$

.

Since DAQ input channel has an input impedance of 10 kΩ which is close to the resistance of the GMR, a buffer is necessary between Wheatstone bridge and DAQ.

The gain of INA163 is flat below 100 kHz shown in Figure 4-53, so it will not create distortion to the signal. The input voltage noise is around 1nV/√Hz and current noise is around 1pA/√Hz. The noise from INA163 will be much lower than DAQ noise floor, so the noise contribution from INA163 can be ignored.

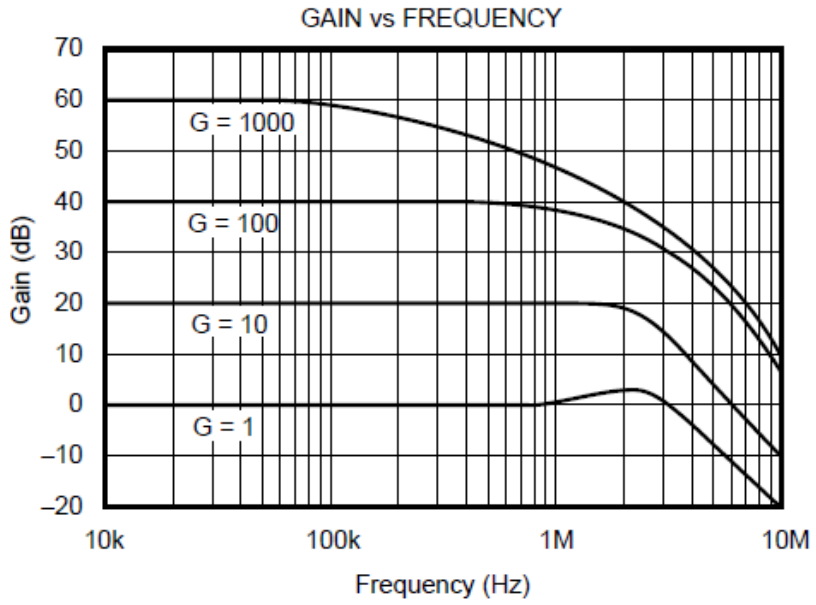

Figure 4-53 Gain of INA163 along frequency

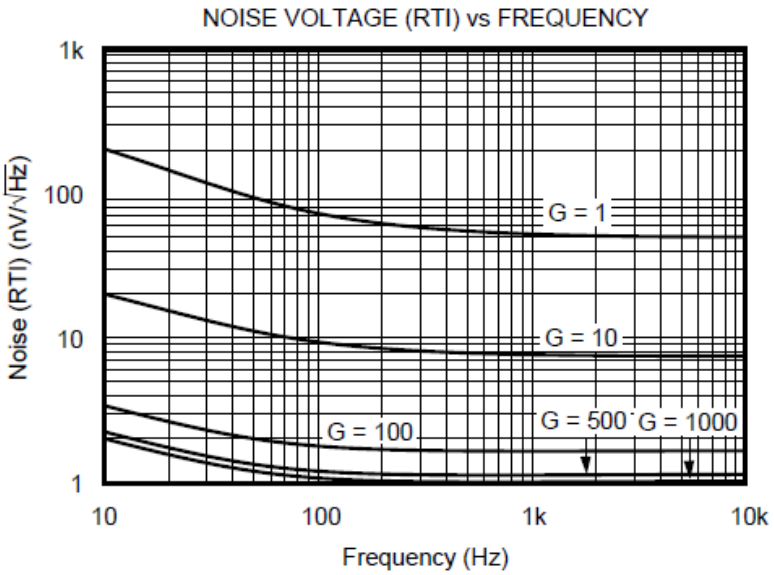

Figure 4-54 Noise voltage of INA163 along frequency

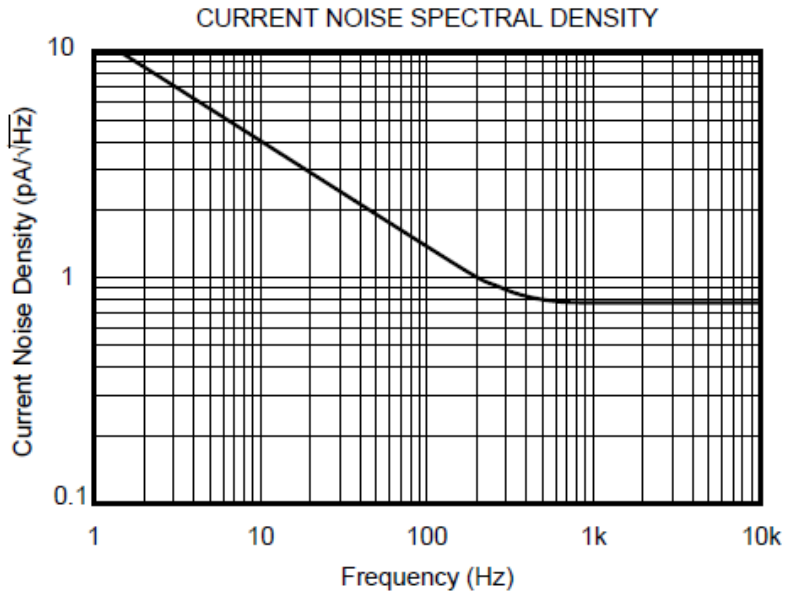

Figure 4-55 Noise current of INA163 along frequency

4.10 System Noise Analyze

To test the noise floors in different stages of the whole system, a 100mV DC voltage from a DAQ output channel is used as an input. The signal is passed through the GMR sensors and amplified. A probe will measure the signal at each stage and feed to a DAQ input channel.

Figure 4-56 shows the noise floor of the DAQ output channel measured directly by a BNC connector. By using a probe will introduce high frequency noise, but will not affect the profile of the noise floor. The PCB will not introduce obvious noise, so the main noise contribution is the output channel of DAQ. By replacing the DAQ output with a battery to generate DC signal will greatly decrease the noise floor as shown in Figure 4-64. By replacing the DAC output with a function generator will not help decrease the noise floor. The frequency jitter between two systems will affect measurement accuracy badly as shown in Figure 4-65. Although the instrumentation amplifier has a gain of 13, the noise floor after amplification as shown in Figure 4-62 doesn't increase 13 times because two differential inputs from resistor-resistor and resistor-sensor shares the same noise source, and thus most noise will be cancelled.

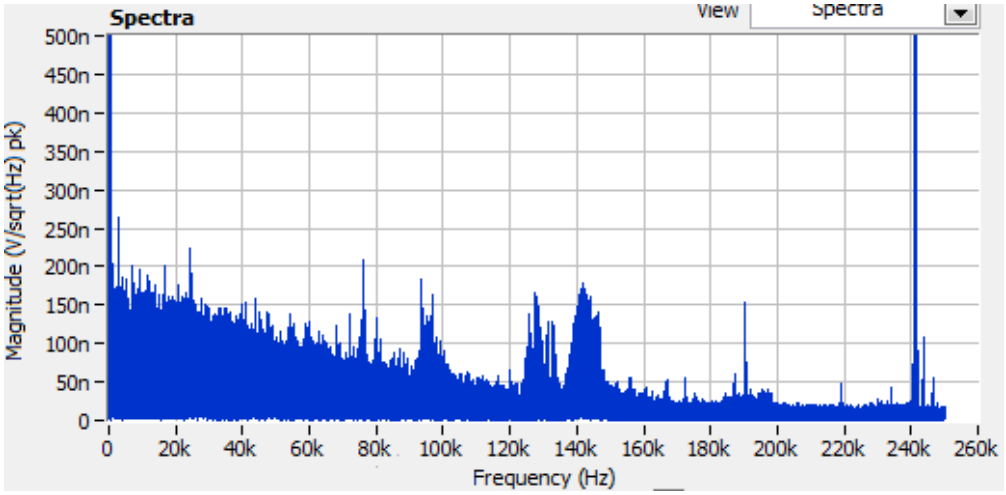

Figure 4-56 Noise floor at DAQ output directly through BNC connector

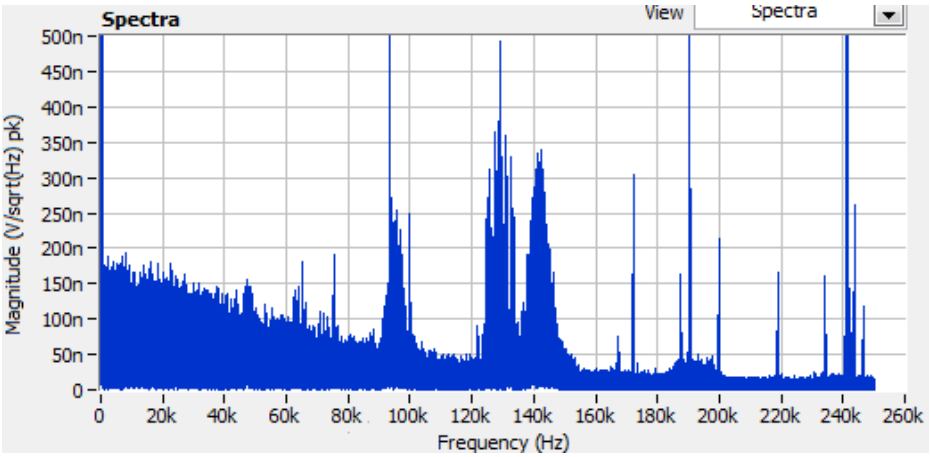

Figure 4-57 Noise floor of input signal to PCB measured by a probe

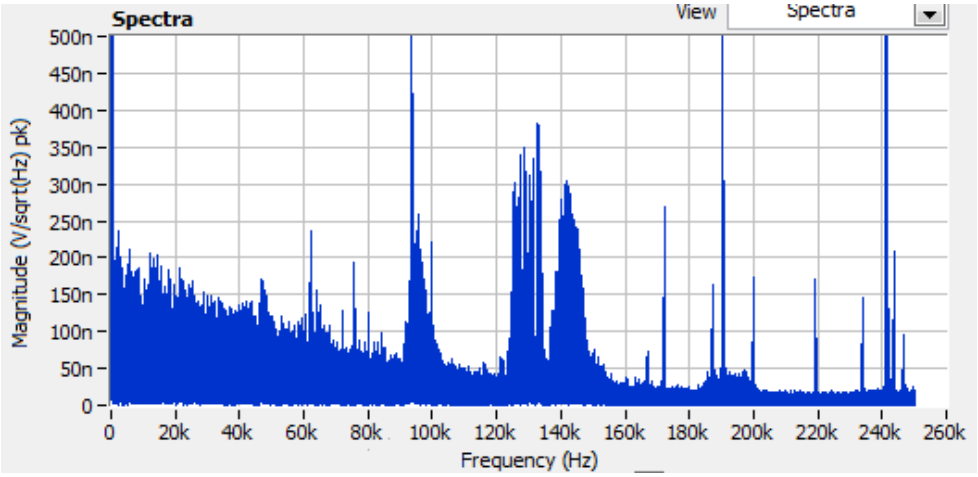

Figure 4-58 Noise floor of signal after the voltage follower measured by a probe

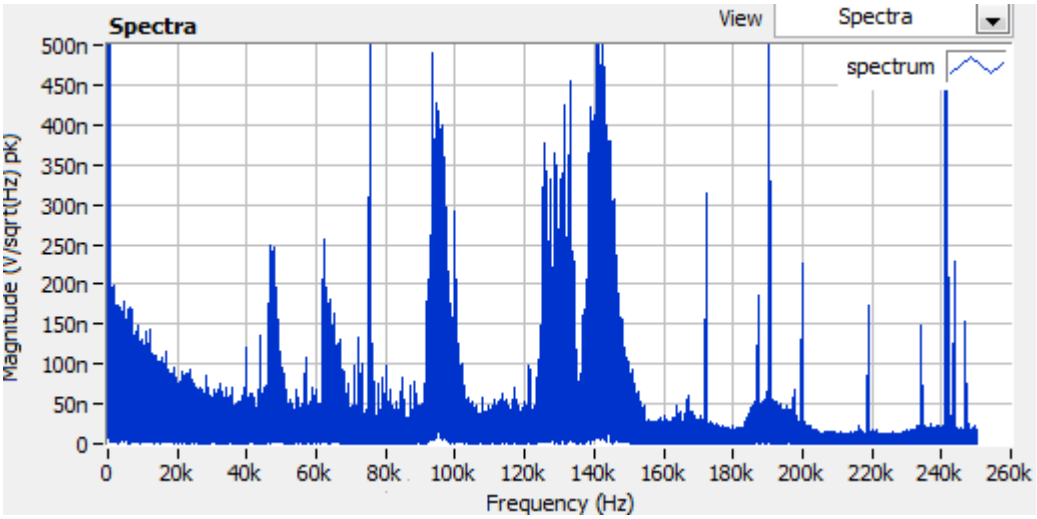

Figure 4-59 Noise floor of signal after the voltage follower measured by a probe. A low pass filter is enabled before the voltage follower.

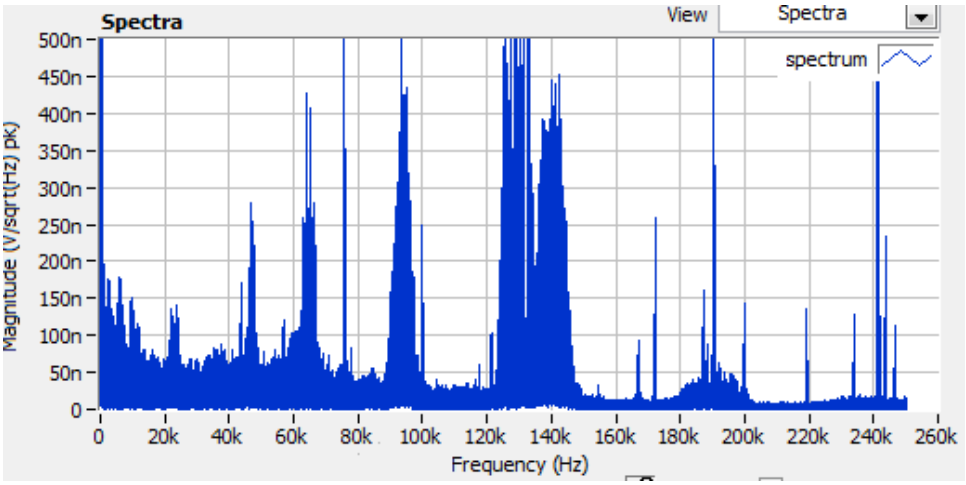

Figure 4-60 Noise floor of signal at the resistor-resistor node in the Wheatstone bridge

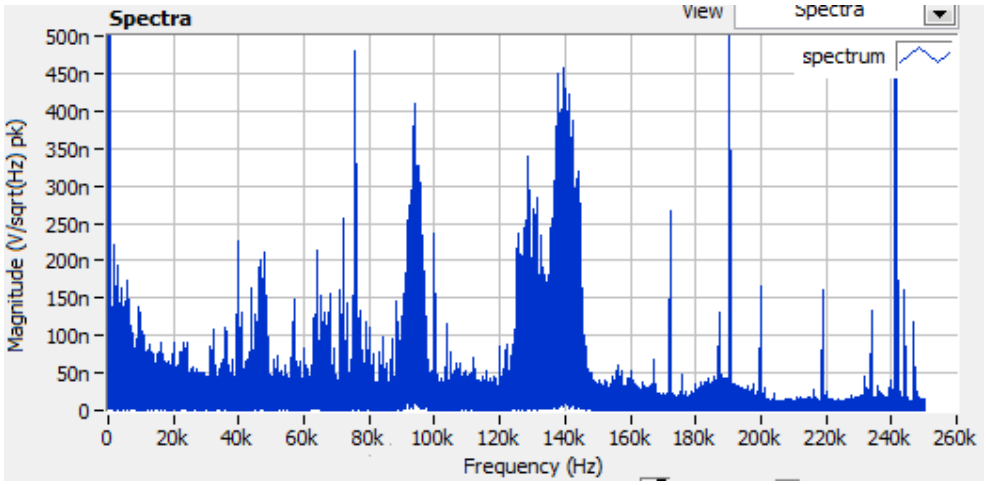

Figure 4-61 Noise floor of signal at the resistor-sensor node in the Wheatstone bridge

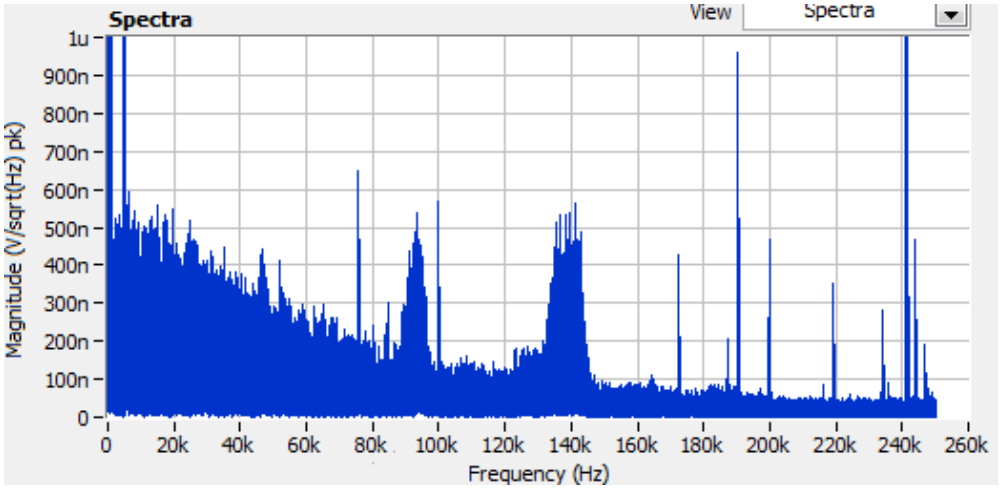

Figure 4-62 Noise floor of signal after an instrumentation amplifier of 13.5 gain

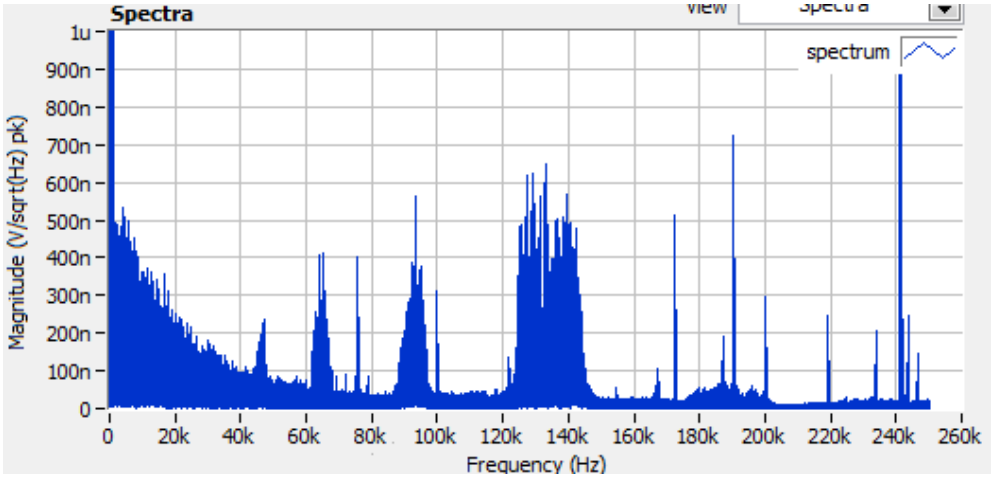

Figure 4-63 Noise floor of signal after an instrumentation amplifier after a low pass filter

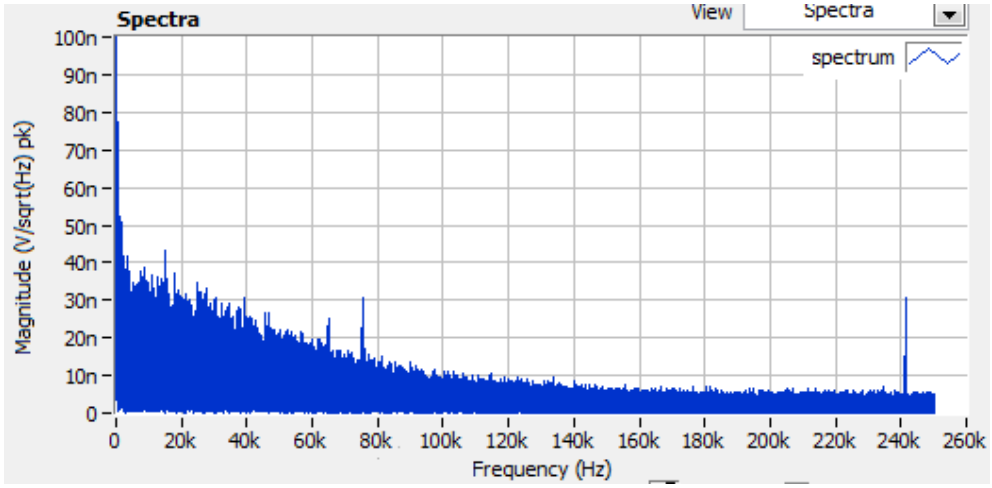

Figure 4-64 Noise floor of 85 mV DC signal provided by a 7.5 V battery and 10 kΩ potentiometer

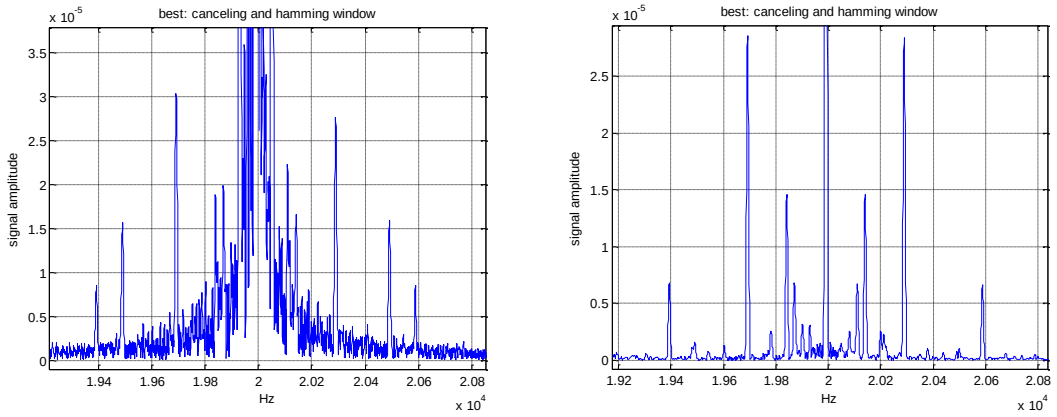

Figure 4-65 Left shows the spectrum of a 20 kHz sine signal generated by a function generator. Right shows the spectrum of a 20 kHz sine signal generated by DAQ itself.

4.11 Other development

4.11.1 Microcontroller Developments

Microcontroller **dsPIC33FJ128MC802** has the capability of performing ADC at **1M Sample/second**, with **resolution 10 bit**. A Sin wave and square wave are generated by function generator and digitized by the microcontroller as shown in Figure 4-66 and Figure 4-67. The DSP core can do **FFT** of input time signal as shown in Figure 4-68, and find the peak frequency and peak amplitude. It also can communicate with computer through USB at the baud rate of 115200 to receive the command from computer and send out the data to computer.

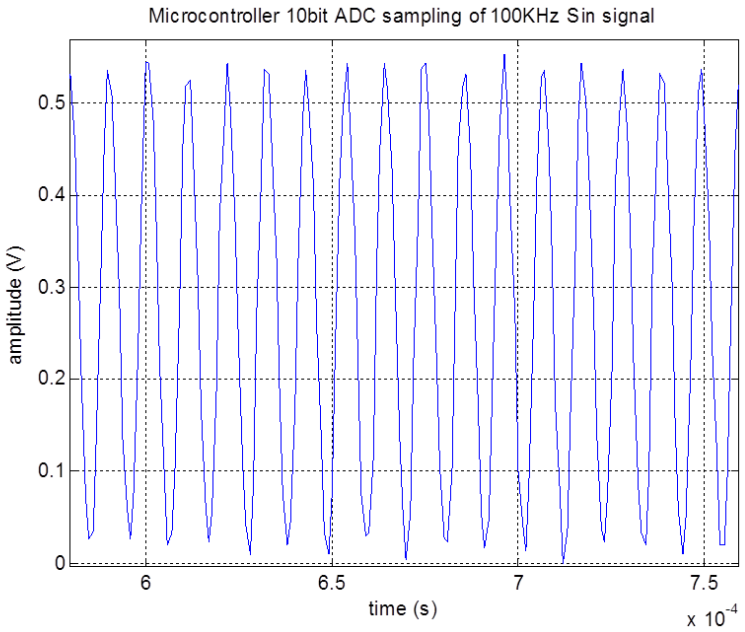

Figure 4-66 A 100 kHz Sin signal sampled by a microcontroller.

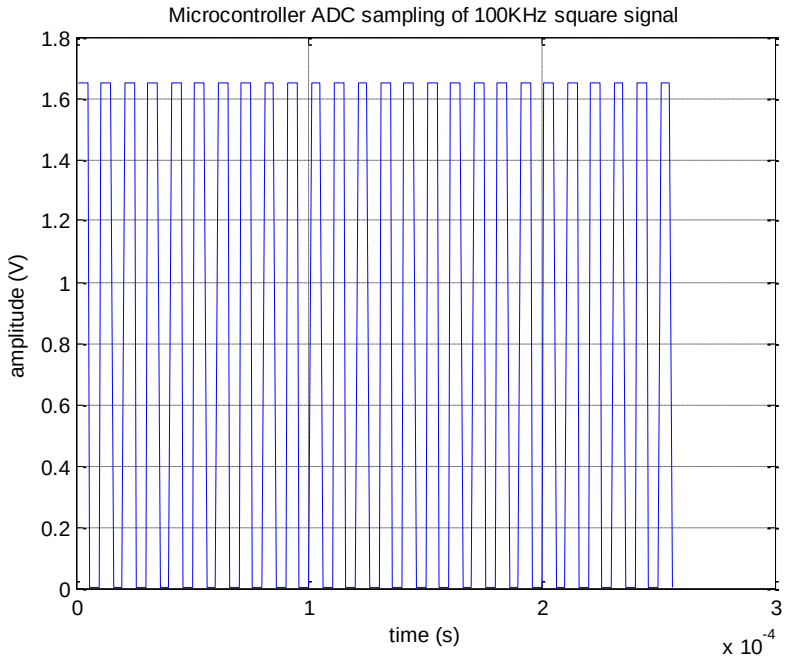

Figure 4-67 A 100 kHz square wave sampled by a microcontroller.

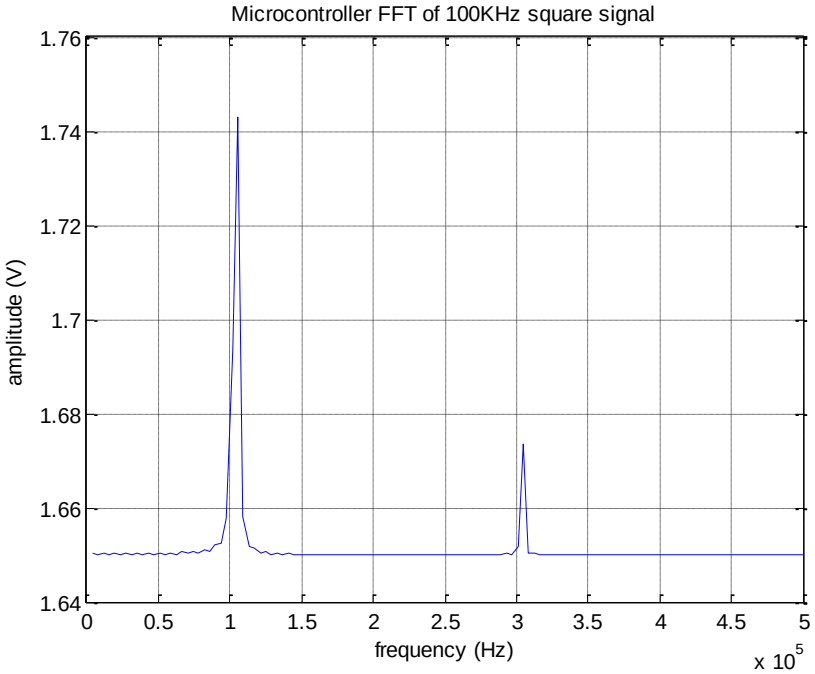

Figure 4-68 Voltage spectrum of Figure 4-67 calculated by FFT module in DSP core in μC. The peak frequency is 0x00018CB4 = 101556 Hz shows the clock mismatch between function generator and μC.

4.11.2 Demodulation circuits

Since DAQ is not perfect in term of noise, an analog circuit can help to increase the SNR. The idea is to use the exact input signal to the GMR to demodulate the output signal to low frequency region. The working principle is similar to that of lock-in amplifier. In the Figure 4-69, A 2 kHz current and 200 Hz field generated by function generator are applied to the sensor. 1.8 kHz and 2.2 kHz mixing frequencies are generated. A multiplier AD743 is used to demodulate the high frequency signal to low frequency region by modulating 2 kHz input signal. The demodulated signal has the spectrum shown in Figure 4-70. Also the DC offset can be trimmed, thus the signal can be amplified effectively.

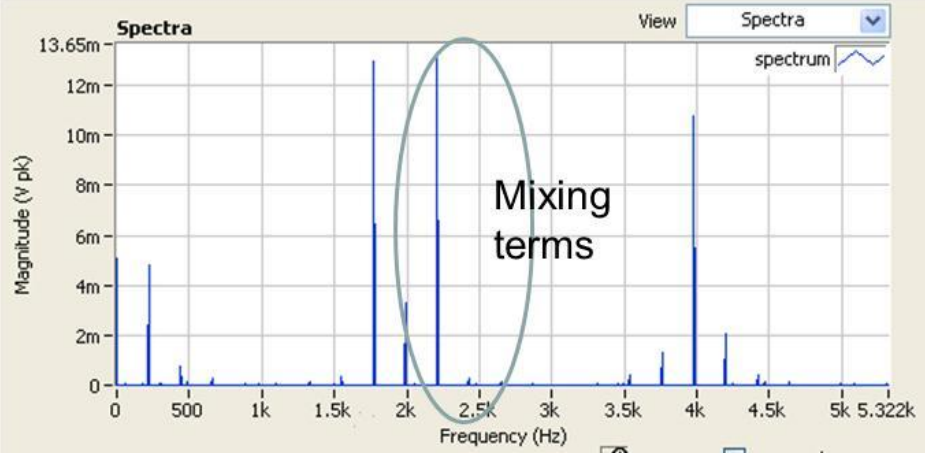

Figure 4-69 A 2 kHz and a 200 Hz signal are applied to the sensor. The output shows the mixing frequencies 1.8 kHz and 2.2 kHz.

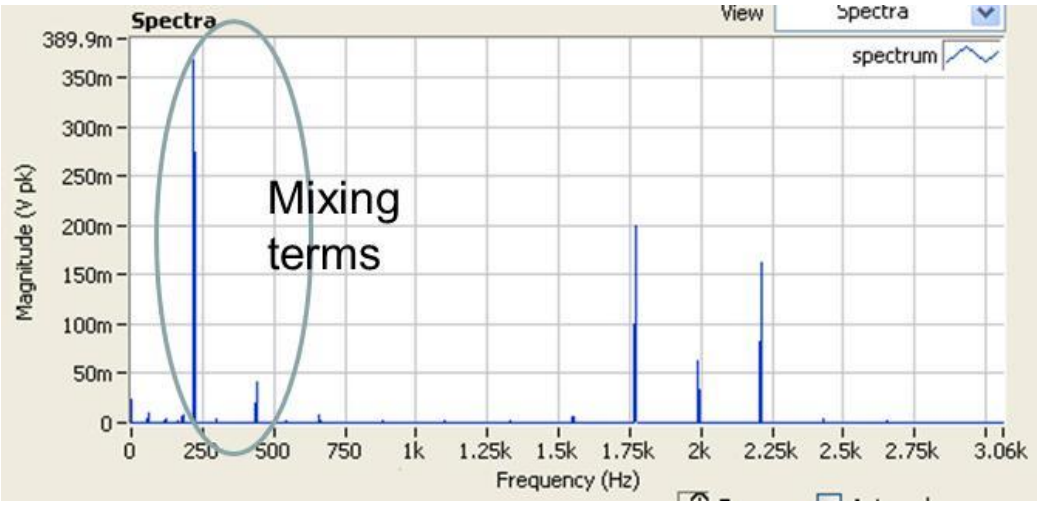

Figure 4-70 By modulating 2 kHz input with the output signal in Figure 4-69, the mixing terms are demodulated in 200 Hz.

4.11.3 Function Generating Circuit

To develop a hand-held system, a XR2206 can be used to generate the sine wave with frequency from 0.01 Hz to 1 MHz. A 3.5 kHz sine wave generated by XR2206 is shown below.

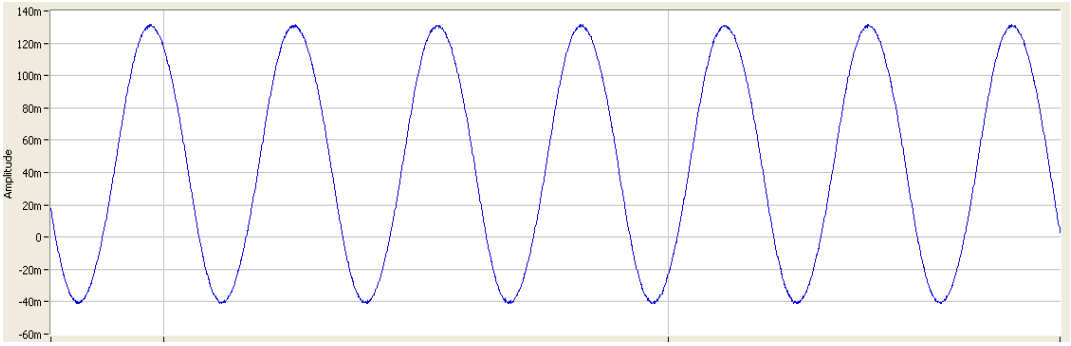

Figure 4-71 a 3.5 kHz sine wave generated by XR2206

[37] Karl F. Anderson, 'Current Loop Signal Conditioning: Practical Applications', NASA Technical Memorandum 4636, Jan. 1995.
[38]Biosensors and Bioelectronics 22 (2007) 2366–2370
[39] Figure 6.37, Chapter 6, Fundamentals of the Metal-Oxide-Semiconductor Field-Effect Transistor', Donald A. Neamen, 'an introduction to Semiconductor devices.'
[40] Data Sheet of 'NI USB-6289', National Instruments
[41] Data sheet of 'OPA827', TI, Nov. 2006
[42] Data sheet of 'ADG 1606', Analog Devices
[43] Data sheet of 'INA163', TI, 16 May 2005

Chapter 5 Conclusion and Outlook

5.1 Conclusion

Superparamagnetic Nanoparticles (MNPs) have been successfully detected by using a search coil based scheme for volume detection and by using a Giant Magneto-Resistance (GMR) sensor for surface detection.

In search coil detection scheme, magnetic and hydrodynamic dynamic response of MNP to the external magnetic field has been analyzed. Proper model for MNP relaxation has been proposed, and the results of MNPs in different coating and solution have been compared with the experiments. The approach to colorize different MNPs by mixing frequency method is also simulated and experimentally verified. Besides MNPs, magnetic thin film and bulk material has also been studied using mixing frequency method.

In GMR detection scheme, various proteins have been detected using MNPs as probes in the sandwich structure. The detection sensitivity is higher than the current ELISA method, and the range covers 5 to 6 orders. Multiple capture antibodies can be printed on the same chip to analyze the one patient sample. Although the exact detection model of GMR is not very accurate, the experiments still show very reliable and repeatable results. GMR noise, protection defects, and bad connections may also affect the sensitivity to a certain level. These issues will be addressed in the future improvement in the fabrication process.

5.2 Outlook

In search coil detection scheme, the current frequency range only covers the audio frequency. By increasing the frequency and increasing the field amplitude, the sensitivity of the detection will increase proportionally. By improving the sampling rate and

resolution in the digital circuit, the SNR will also increase. More advanced analog circuit can be used to reduce the burden of DAQ and reduce the noise from DAQ. The coil design can be further improved to fit the applications of small scale detection or high frequency detection. Coil, in the form of transmission line, can study the FMR of magnetic material. One rough approach to study the RF response of MNPs is presented in the section FMR in the appendix.

In GMR detection scheme, GMR detection model needs to be fully understood in order to design an optimal sensor. The protection layer needs to be more reliable so that the nonmagnetic factors will not cause the drift of the sensor signal. The issue of current leakage to the semiconductor needs to be addressed, because the unnecessary conductance and susceptance of the semiconductor will decrease the signal and introduce noise. Also the noise spectrum of the GMR needs further study to design a better circuit for optimal SNR. Furthermore, the GMR technology can be incorporated with other detection method, such as ultrasound, magnetic semiconductor, and etc.

Magnetic bio-sensors, compared to currently popular optical bio-sensors, have shown very promising market. The natural background noise is much less than optical method, which can push the detection limit further down. Also the magnetic sensors are more easily compatible with CMOS technology, which makes them good candidates for point-of-care devices. As the technology has been used for hard disk drive for several decades, magnetic bio-sensor benefits from very mature industry and researches. Plus with the properties of cheap cost and light weight, magnetic bio-sensor will have a bright future.

Bibliography

[1]Robert C. O'Handley, Modern Magnetic Materials: Principles and Applications.
Publication Date: Nov. 26, 1999| ISBN-10: 0471155667| ISBN-13:978-0471155669| Edition: 1

[2] Superparamagnetism, (Oct. 22nd, 2012), from
http://en.wikipedia.org/wiki/Superparamagnetism

[3] Superparamagnetism, (Oct. 22nd, 2012), from
http://lmis1.epfl.ch/webdav/site/lmis1/shared/Files/Lectures/Nanotechnology%20for%20engineers/Archives/2004_05/Superparamagnetism.pdf

[4] Y. Jing, S. He, T. Kline, Y. Xu and J.P. Wang, 'High-Magnetic-Moment Nanoparticles for Biomedicine', 31st Annual International Conference of the IEEE EMBS, Minneapolis, Minnesota, USA, September 2-6, 2009.

[5] K. M. Krishnan, A. B. Pakhomov, Y. Bao, et al.,'Nanomagnetism and spin electronics: materials, microstructure and novel properties.' J Mater Sci 41 (2006) 793-815.

[6] Landau-Lifshitz-Gilbert equation, (Oct. 23rd, 2012), from
http://en.wikipedia.org/wiki/Landau%E2%80%93Lifshitz%E2%80%93Gilbert_equation

[7] W. T. Coffey, P. J. Gregg, and Y. P. Kalmykov, 'On the Theory of Debye and Néel Relaxation of Single Domain Ferromagnetic Particles', in Advances in Chemical Physics, edited by I. Prigogine and S. A. Rice (Wiley, New York, 1993), Vol. 83, p. 263

[8] B K P Scaife, 'On the low-field, low-frequency susceptibility of magnetic fluids', J. Phys. D: Appl. Phys. **19** (1986) L195-L197

[9] Vibrating sample magnetometer, (Oct. 31st, 2012), from
http://en.wikipedia.org/wiki/Vibrating_Sample_Magnetometer

[10] Scanning electron microscope, (Oct. 31st, 2012), from
http://en.wikipedia.org/wiki/Scanning_electron_microscope

[11] Transmission electron microscope, (Oct. 31st, 2012), from
http://en.wikipedia.org/wiki/Transmission_electron_microscopy

[12] Dynamic light scattering, (Oct. 31st, 2012), from
http://en.wikipedia.org/wiki/Dynamic_light_scattering

[13] J. Lenz, IEEE Proceedings, **78**, 973, (1990)

[14] Caruso, Michael J; Tamara Bratland; Carl H Smith, PhD; and Robert Schneider, "A New Perspective on Magnetic Field Sensing," Honeywell Inc, May 1998, www.ssec.honeywell.com/magnetic/datasheets/new_pers.pdf

[15] http://www.boulder.nist.govdiv81881803MagneticDevicesandNanoStructuresindex.html

[16] Quantum Design, San Diego, CA, 'http://www.qdusa.com/products/ppms.html'

[17] Imego Institute, Göteborg, SWEDEN, 'http://www.imego.com/Products/dynomag/index.aspx'

[18] P.C. Fannin, B.K.P. Scaife, J. Magn.Magn.Mater.**72**, 95 (1988)

[19] Magnetic dipole, 11/9/2012, from 'http://en.wikipedia.org/wiki/Magnetic_dipole'

[20] http://www.oceannanotech.com/upload/090604131348592520yef2g1.pdf

[21] T.L. Paoli and J.F. Svacek, Rev. Sci. instrum., **47**, 9 (1976)

[22] Petr I. Nikitin, Petr M. Vetoshko, and Tatiana I. Ksenevich, J. Magn. Magn.Mater.**311**, 445 (2007)

[23] Hans-Joachim Krause, Norbert Wolters, Yi Zhang, Andreas Offenhausser, Peter Miethe, Martin H.F. Meyer, Markus Hartmann, and Michael Keusgen, J. Magn. Magn.Mater.**311**, 436 (2007)

[24] R.E. Rosensweig, J. Magn. Magn.Mater.**252**, 370 (2002)

[25] M.I. Shliomis, Yu.L. Raikher, IEEE Trans. Magn. **MAG-16**, 237 (1980)

[26] J Dieckhoff, M. Schilling, and F. Ludwig, "Fluxgate based detection of magnetic nanoparticle dynamics in a rotating magnetic field."*Appl. Phys. Lett.*, vol. 99, p. 112501, 2011

[27] T. Yoshida, K. Enpuku, J. Dieckhoff, M. Schilling, and F. Ludwig, "Magnetic fluid dynamics in a rotating magnetic field" J. Appl. Phys., vol. 111, pp. 053901, 2012

[28] T. L. Paoli and J. F. Svacek, "Derivative measurement by frequency mixing," Rev. Sci. Instrum., vol. 47, p. 1016, 1976

[29] W. T. Coffey, P. J. Cregg, and Y. P. Kalmykov, "On the theory of Debye and Néel relaxation of single domain ferromagnetic particles," *Advances in Chemical Physics*, vol. 83, p. 263, 1993

[30] http://crca.ucsd.edu/~msp/techniques/v0.11/book-html/node86.html

[31] Liang Tu, et. al. 'Measurement of Brownian and Néel Relaxation of Magnetic Nanoparticles by a Mixing-Frequency Method', IEEE Transactions on Magnetics, Vol 49, No. 1, January 2013

[32] K. Enpuku, T. Tanaka, Y. Tamai, F. Dang, N. Enomoto, J. Hojo, H. Kanzaki, and N. Usuki, Jpn. J. Appl. Phys. **47**, 7859 (2008)

[33] C.M. Oireachtaigh, P.C. Fannin, J. Magn.Magn.Mater.**320**, 871 (2008)

[34] B.K.P. Scaife, J. Phys. D: Appl. Phys. **19**, 195 (1986)

[35] C. Hong, C.C. Wu, Y.C. Chiu, S.Y. Yang, H.E. Horng, and H.C. Yang,Appl. Phys.Lett. **88**,212512 (2006)

[36] J.S. Daniels, E.P. Anderson, N. Pourmand, and T.H. Lee, IEEE, Instrumentation and Measurement Technology Conference, (2010)

[37] Karl F. Anderson, 'Current Loop Signal Conditioning: Practical Applications', NASA Technical Memorandum 4636, Jan. 1995.

[38] Biosensors and Bioelectronics 22 (2007) 2366–2370

[39] Figure 6.37, Chapter 6, Fundamentals of the Metal-Oxide-Semiconductor Field-Effect Transistor', Donald A. Neamen, 'an introduction to Semiconductor devices.'

[40] Data Sheet of 'NI USB-6289', National Instruments

[41] Data sheet of 'OPA827', TI, Nov. 2006

[42] Data sheet of 'ADG 1606', Analog Devices

[43] Data sheet of 'INA163', TI, 16 May 2005

Appendix

1. 1 FMR

Ferromagnetic resonance (FMR) is a spectroscopic technique to probe the magnetization of ferromagnetic materials. [44] The resonance comes from the unpaired electrons. The resonance frequency depends on the gyromagnetic ratio γ, and effective magnetic field including external field and anisotropy field. For sphere sample, there is no direction preference, and the resonance frequency is $\omega_0 = \gamma B_0$.[45] As an illustration shown in Figure 5-1, the resonance frequency has a linear dependence on the applied field H. However, when pH=6, the MNPs have chemical binding affinity, and the stray field of MNPs will affect each other. The resonance frequency is spread due to the various interactions of MNPs, and the line width ΔH will be bigger.

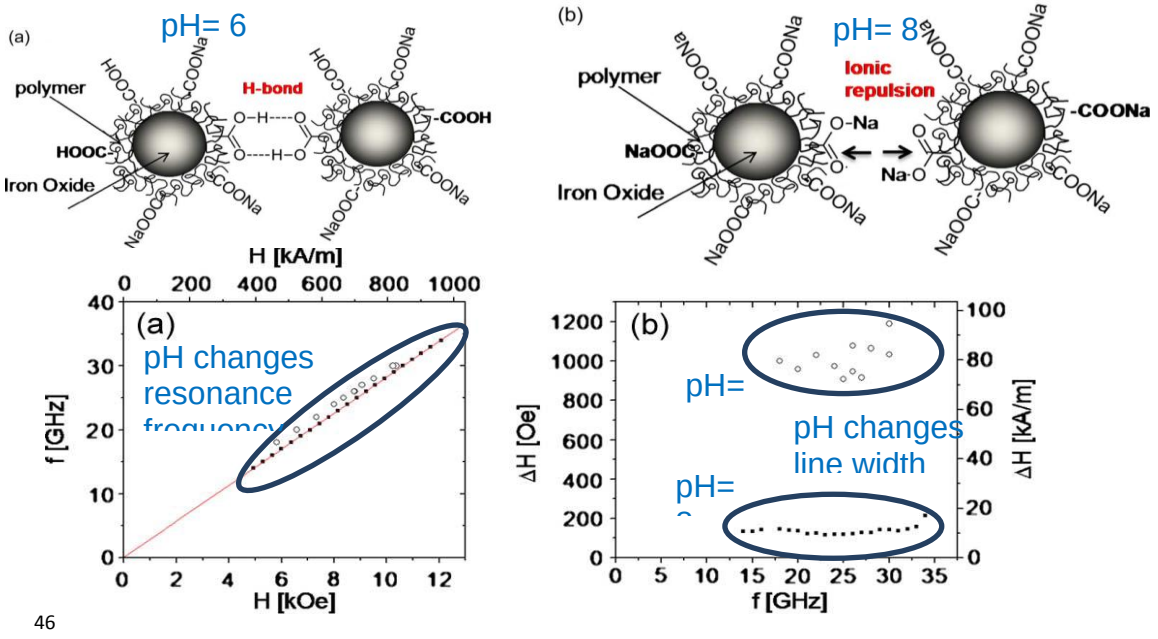

46

Figure 5-1 Resonance frequency (left figure) and line width (right figure) of MNP are dependence on pH of solution (dot represents pH=8; circle represents pH=6).[46]

In order to detect the FMR of MNPs, a transmission line (Tline) is needed to deliver and transmit the microwave. The microwave absorption of the MNPs will be detected through the transmission and reflection coefficients measured by a network analyzer. The transmission line is designed and fabricated based on a 4-layer PCB as shown in Figure 5-2. A simple in-planar spiral is simulated in Sonnet and HFSS. The HFSS full-wave simulation tool can generate the EM wave distribution along the line Figure 5-4. The Sonnet simulator can calculate the S-parameters Figure 5-5 and input impedance Figure 5-7 along frequency. There is no simple way to simulate the effects from the MNPs, so I simply increase the permeability μ_r=2 to see how the results will be affected. Figure 5-6 and Figure 5-7Figure 5-8 show that the peaks of S-parameters and input impedance will be shifted and changed. Increasing the turns of the coil shown in Figure 5-9, more complicated pattern of S-parameters is generated in Figure 5-10. By carefully design the shape of the transmission line, we will find an optimal detection method for the MNPs. However, here as a first try, co-planar Tline with and without gap, planar coil with different turns and sizes are designed in Figure 5-11. All the connection lines are designed in 50Ω configuration to decrease the signal loss to/from the sensor spot. The MNPs samples are iron oxide particles, and a permanent magnet is used to generate non-uniform field. From left to right, the measurement of Tline1 to Tline6 are plotted from Figure 5-12 to Figure 5-17. The blue lines show the difference of S-parameters by adding MNPs. The green lines show the differences of S-parameters by adding MNPs with a permanent magnet. There is clear evidence that the MNPs affect the microwave transmission on the Tline. However, the FMR effects need further studies.

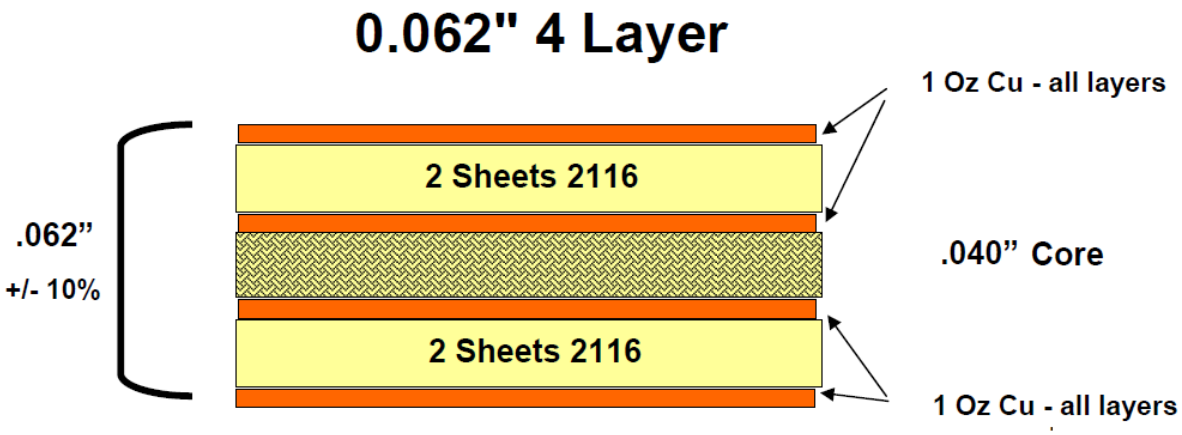

Figure 5-2 Structure of a 4-layer PCB[47]

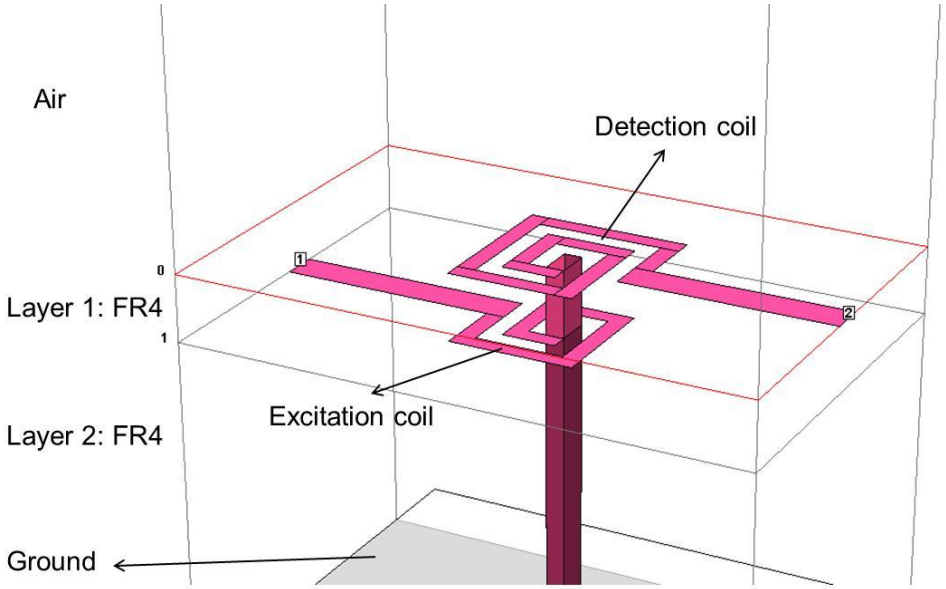

Figure 5-3 Coil Design in Sonnet simulation

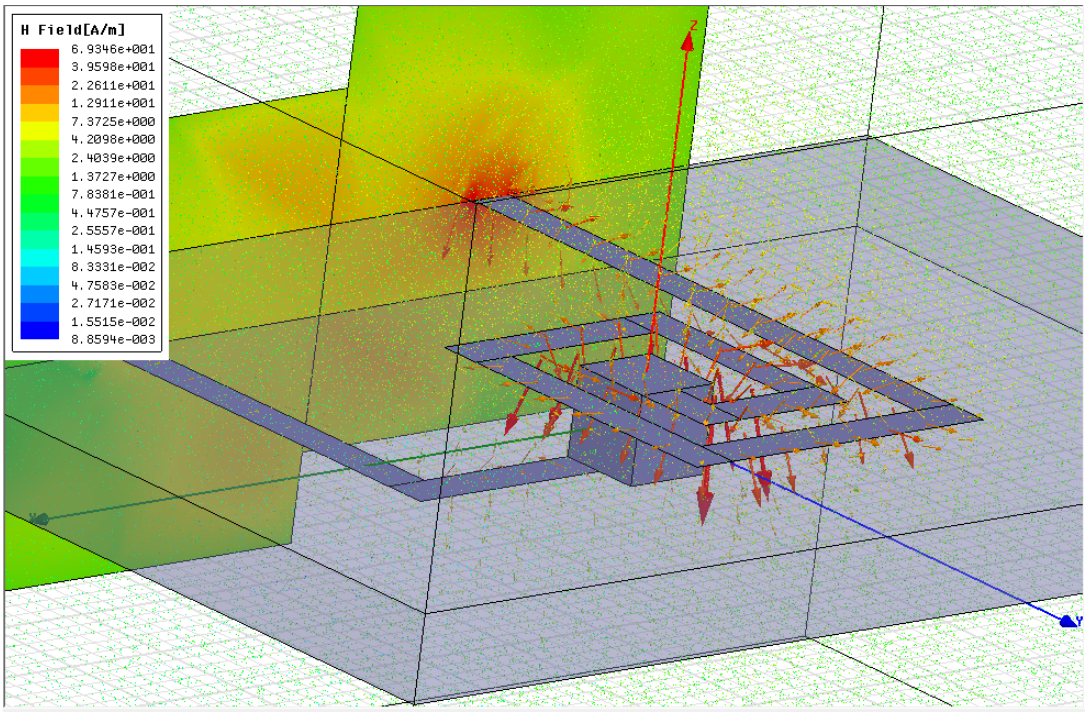

Figure 5-4 Magnetic field distribution by HFSS

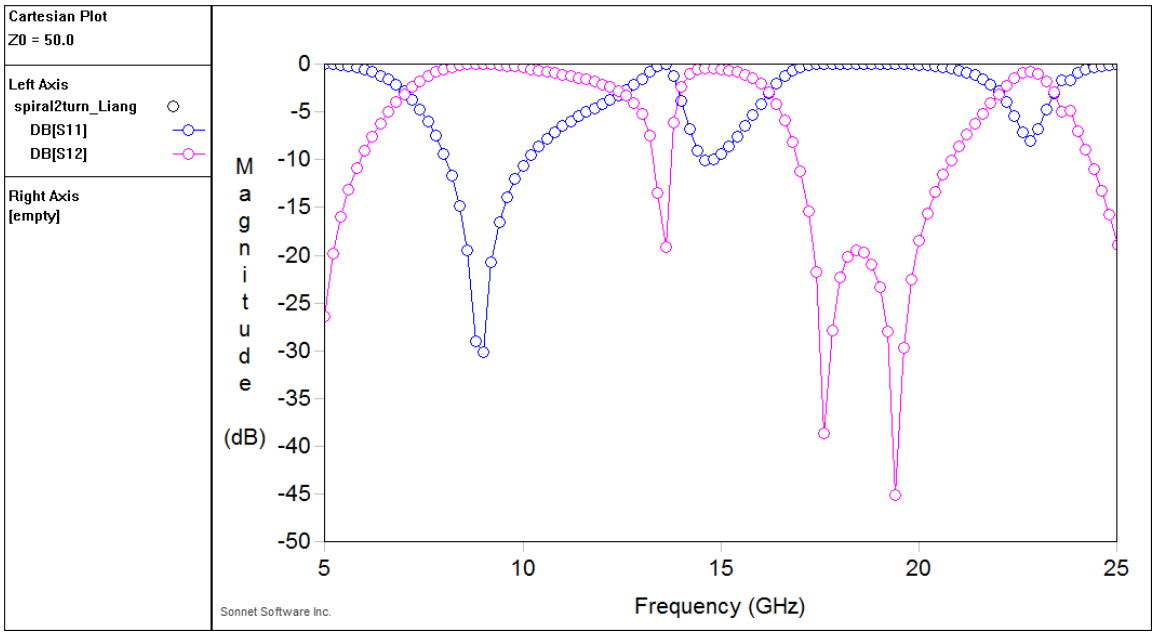

Figure 5-5 S-parameter measurement in Sonnet simulation

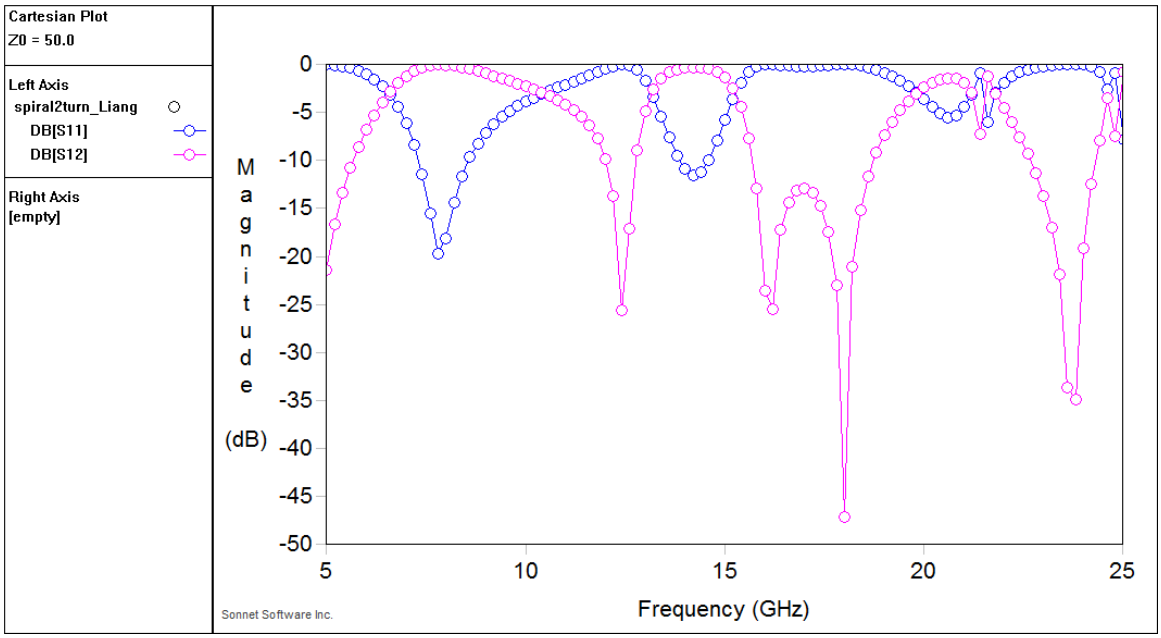

Figure 5-6 S-parameter measurement in Sonnet simulation.μ_r is changed to 2 to represent MNPs.

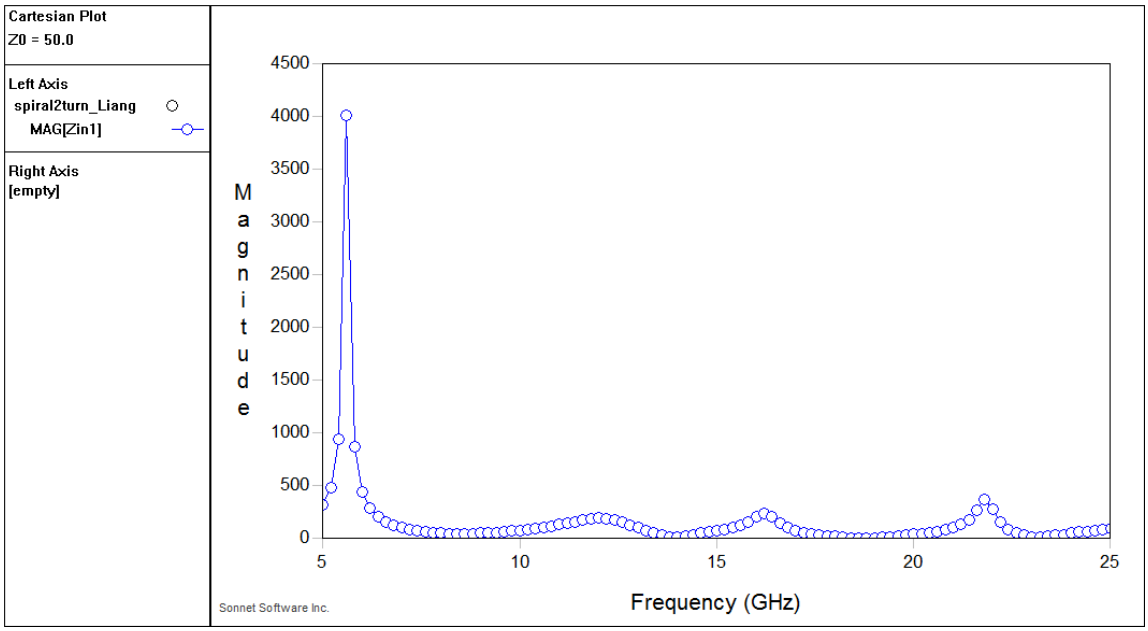

Figure 5-7 Input impedance measurement in Sonnet simulation.

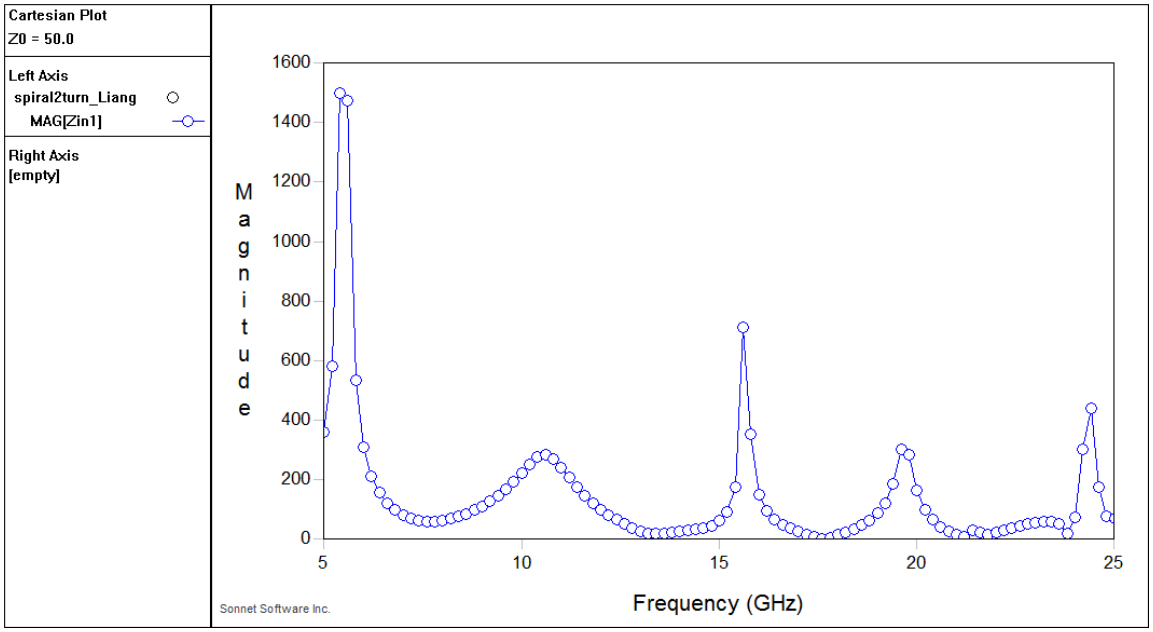

Figure 5-8 Input impedance measurement in Sonnet simulation. μ_r is changed to 2 to represent MNPs.

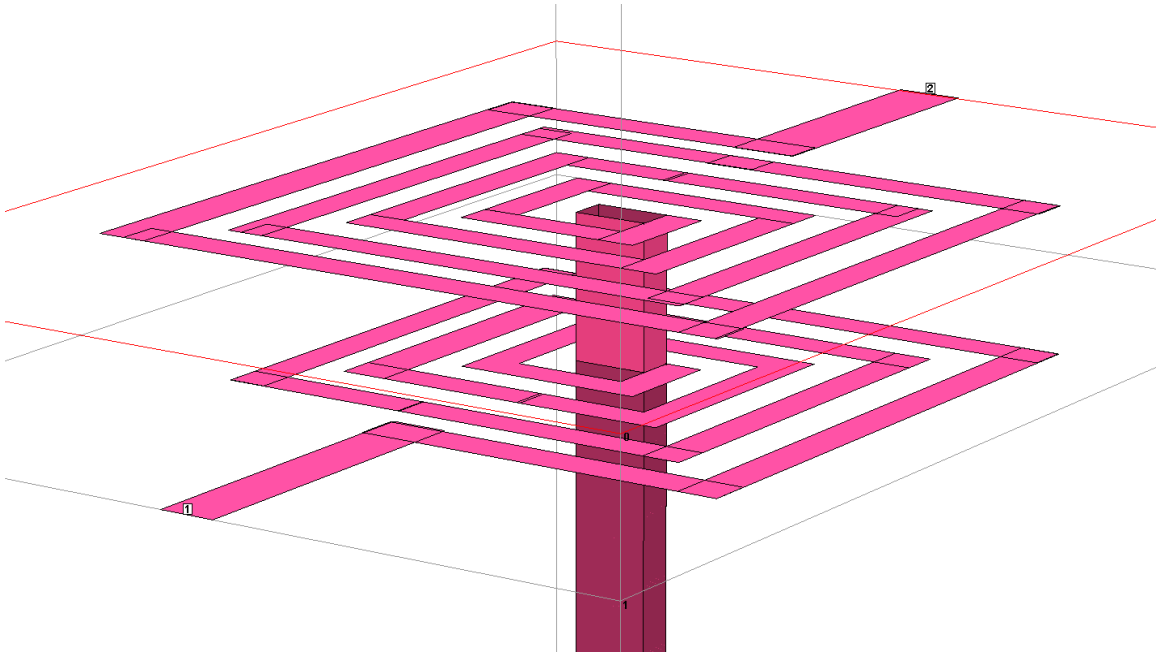

Figure 5-9 Coil Design with more turns in Sonnet simulation

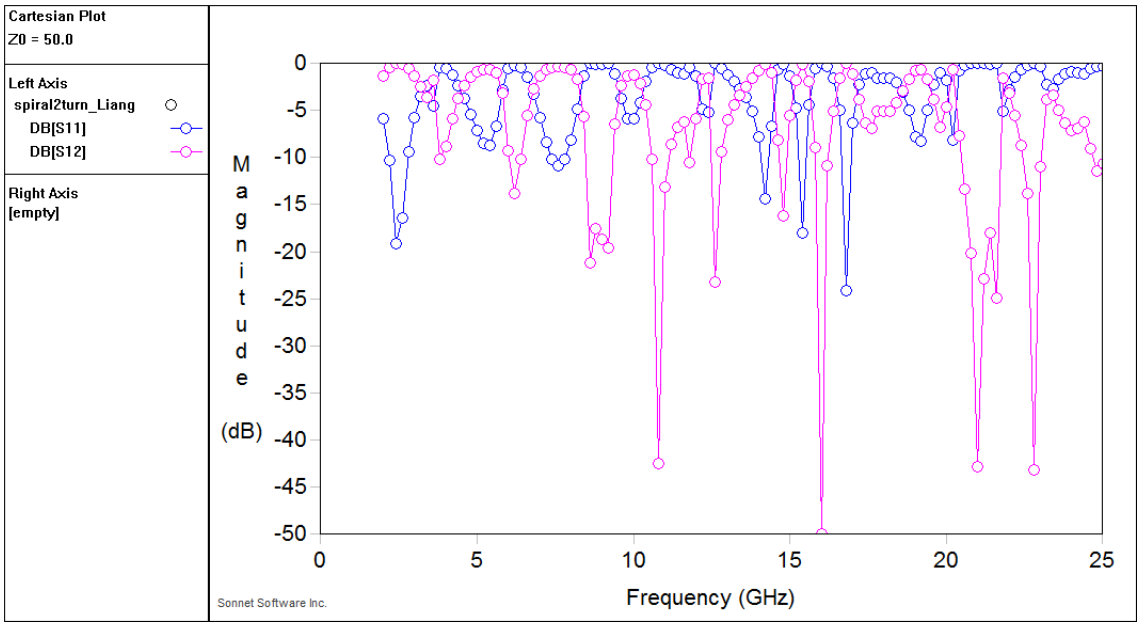

Figure 5-10 S-parameter measurement in Sonnet simulation

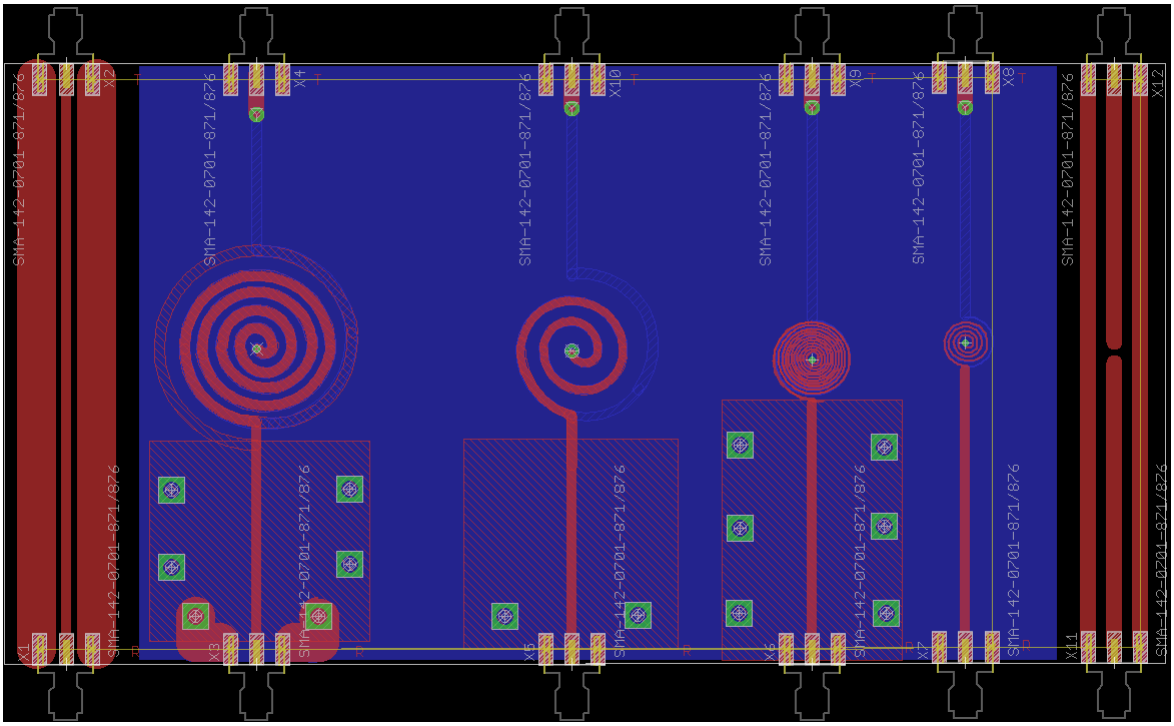

Figure 5-11 PCB design of various transmission lines

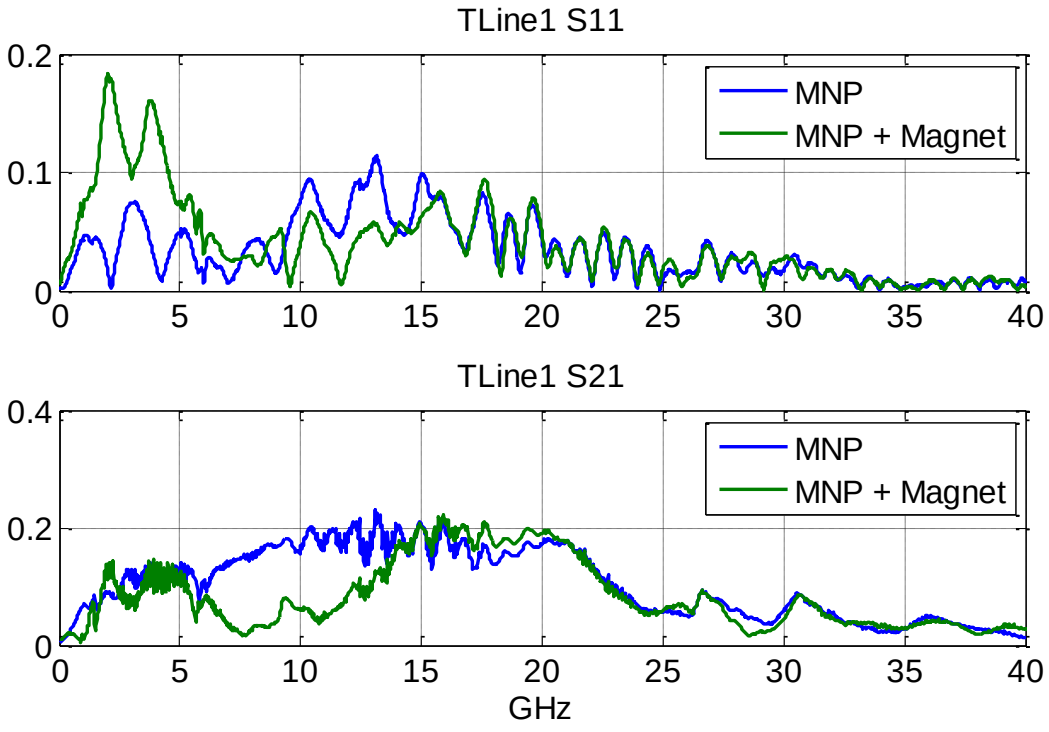

Figure 5-12 S-parameter of TLine1

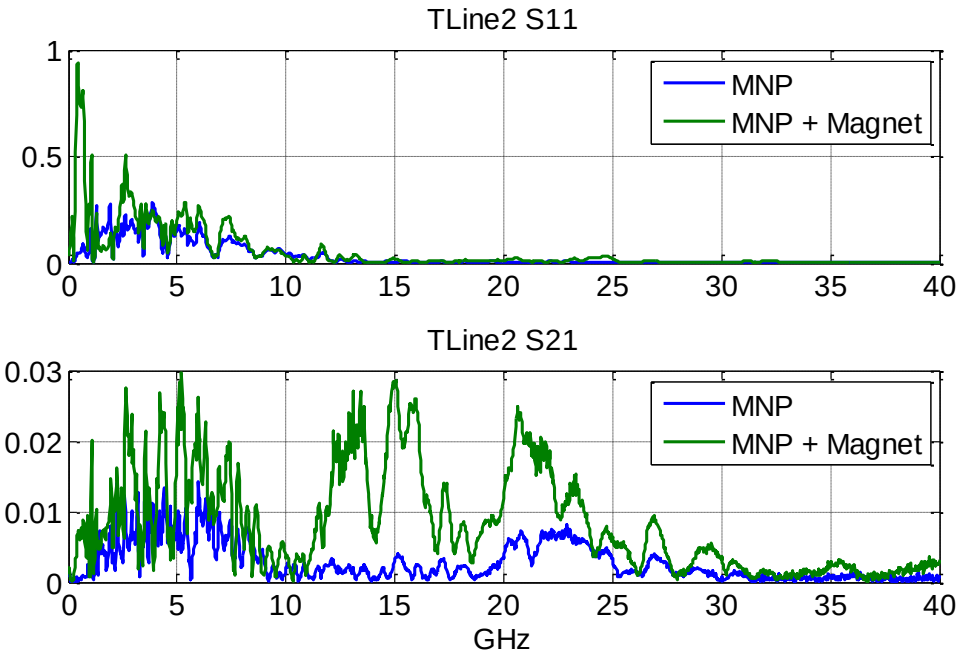

Figure 5-13 S-parameter of TLine2

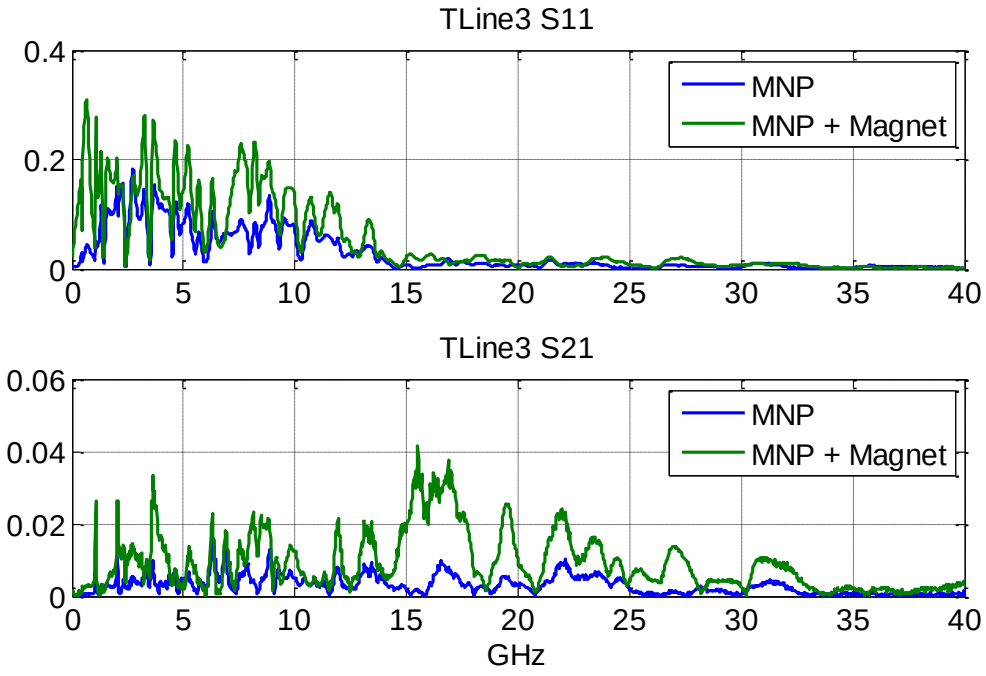

Figure 5-14 S-parameter of TLine3

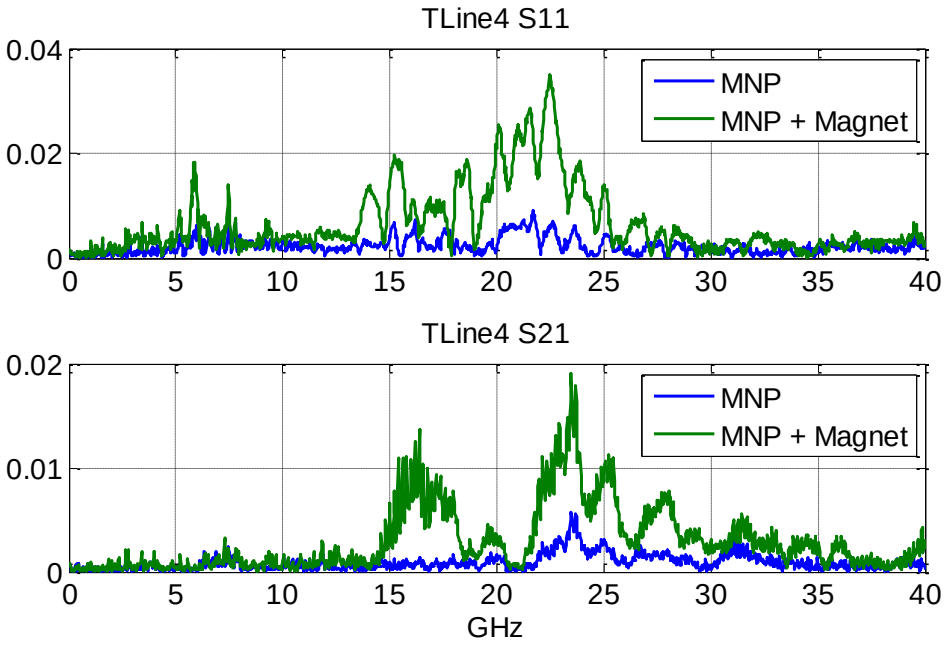

Figure 5-15 S-parameter of TLine4

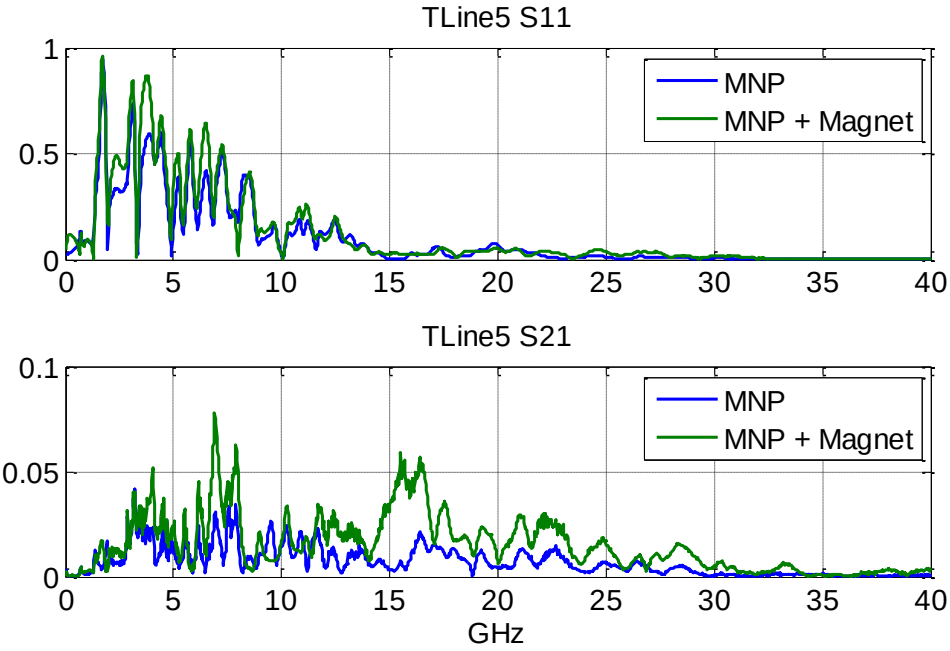

Figure 5-16 S-parameter of TLine5

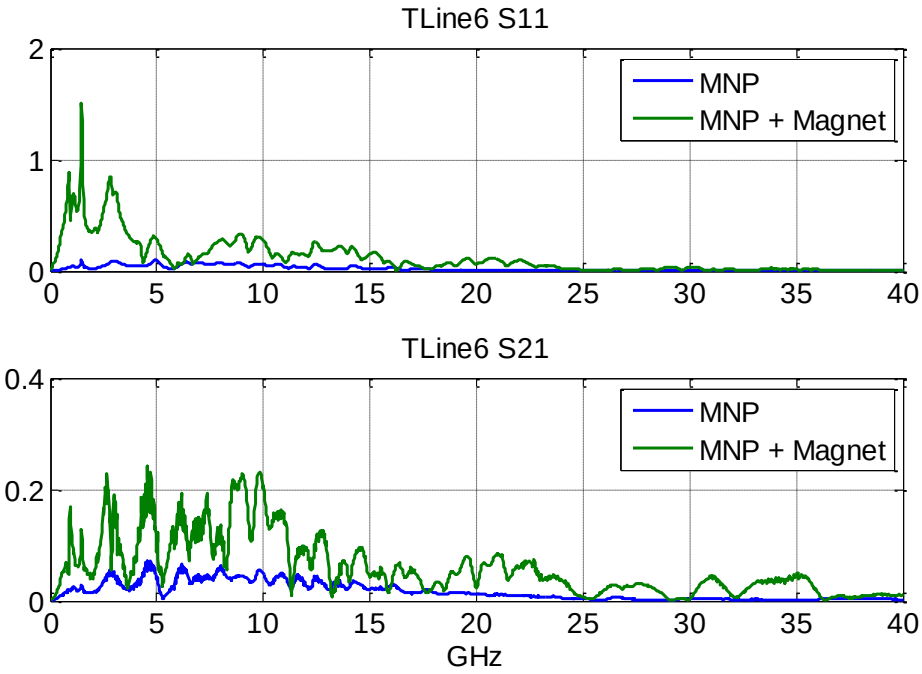

Figure 5-17 S-parameter of TLine6

[44] http://en.wikipedia.org/wiki/Ferromagnetic_resonance

[45] Charles Kittel, 'Introduction to Solid State Physics'. 8th edition.

[46]'Relaxation of Polymer Coated …', University of Alabama, IEEE,Vol 46, No. 6, June 2010

[47]http://www.4pcb.com/index.php?load=content&page_id=242